**Title**
Imaging Spectroscopy Applications for Mapping and Monitoring Environmental Change in Louisiana's Coastal Wetlands



**Author**
Jensen, Daniel John

**Publication Date**
2019

Peer reviewed|Thesis/dissertation

UNIVERSITY OF CALIFORNIA

Los Angeles

# Imaging Spectroscopy Applications for Mapping and Monitoring Environmental Change in Louisiana's Coastal Wetlands

A dissertation submitted in partial satisfaction of the

requirements for the degree Doctor of Philosophy

in Geography

by

Daniel John Jensen

2019

ABSTRACT OF THE DISSERTATION

Imaging Spectroscopy Applications for

Mapping and Monitoring Environmental Change in Louisiana's Coastal Wetlands

by

Daniel John Jensen

Doctor of Philosophy in Geography

University of California, Los Angeles, 2019

Professor Kyle Cavanaugh, Chair

Louisiana's coastal wetlands are continually threatened by anthropogenic disturbances and relative sea level rise (RSLR), factors which have caused widespread degradation and loss. This region has historically been a productive ecosystem with high carbon sequestration capacity that offers important ecological benefits to neighboring communities. The region's "blue carbon" stocks and ecosystem services are now severely degrading with the coastal wetlands' ongoing submergence resulting from RSLR. Accretion is the trapping of sediments and deposition of organic matter resulting in the buildup of the soil surface, and wetlands will submerge if the factors governing accretion do not sufficiently account for RSLR. Remote sensing offers data that can be applied to wetland ecology to assess ecological processes relating to RSLR and accretion at a regional scale. Imaging spectroscopy, specifically, enables sophisticated modeling techniques that may improve

remote sensing applications in wetland regions. This project applies imaging spectroscopy to Louisiana's coastal wetlands, developing applications for Airborne Visible/Infrared Imaging Spectrometer-Next Generation (AVIRIS-NG) data that include image processing algorithms, environmental parameter retrievals, and assessment of vegetation growth patterns and changes. The study's first chapter addresses image processing methods for correcting bidirectional reflectance distribution function (BRDF) effects that inhibit image mosaicking. We developed a new empirical algorithm—the adaptive reflectance geometric correction—and applied it to imagery collected around the Atchafalaya and Wax Lake deltas to produce optimized surface reflectance mosaics. The second chapter sees the estimation and mapping of hydrologic suspended solids in from those AVIRIS-NG mosaics with an independently validated and transferable algorithm. The third chapter integrates the AVIRIS-NG data with simultaneously collected data from the Uninhabited Airborne Vehicle Synthetic Aperture Radar (UAVSAR) to estimate aboveground biomass (AGB) in Louisiana's Wax Lake Delta (WLD). The fourth chapter uses the AVIRIS-NG data to map the WLD's vegetation species distribution, then compares the results to published data from five years prior to assess extent changes for key vegetation types. It further employs the AGB dataset to examine key species' growth patterns across elevational gradients and zones. The methods and results developed herein will enable future efforts to model accretion and predict wetland loss at regional scales.

The dissertation of Daniel John Jensen is approved

Robert Twilley

Yongwei Sheng

Gregory Okin

Marc Simard

Kyle Cavanaugh, Committee Chair

University of California, Los Angeles

2019

LIST OF FIGURES

LIST OF TABLES

Table

# ACKNOWLEDGMENTS

Funding for this research was primarily provided by the NASA Earth and Space Science Fellowship (grant number NNX16AO43H) and the UCLA Graduate Research Mentorship Award. Additional funding for field work and publications was provided by NASA Jet Propulsion Laboratory (JPL) internal funding (grant number 01STCR – R.16.023.011), JPL's Strategic Research and Technology Development funding (grant number 01STCR – R.17.231.069), and the NASA Carbon Monitoring System program (grant number 105357-613570.02.03.02.09).

Chapter 1 was published as follows: Jensen, Daniel J., Marc Simard, Kyle C. Cavanaugh, and David R. Thompson. 2017. "Imaging Spectroscopy BRDF Correction for Mapping Louisiana's Coastal Ecosystems." *IEEE Transactions on Geoscience and Remote Sensing* 56 (3): 1739–48. doi: 10.1109/TGRS.2017.2767607.

Chapter 2 was published as follows: Jensen, Daniel, Marc Simard, Kyle Cavanaugh, Yongwei Sheng, Cédric G. Fichot, Tamlin Pavelsky, and Robert Twilley. 2019. "Improving the Transferability of Suspended Solid Estimation in Wetland and Deltaic Waters with an Empirical Hyperspectral Approach." *Remote Sensing* 11 (1629). doi: 10.3390/rs11131629. I would like to acknowledge Alexandra Christensen, Christine Lion, and Robert Lane for their roles in collecting and processing the water sample data for this study.

Chapter 3 was published as follows: Jensen, Daniel, Kyle C. Cavanaugh, Marc Simard, Gregory S. Okin, Edward Castañeda-Moya, Annabeth McCall, and Robert R. Twilley. 2019. "Integrating Imaging Spectrometer and Synthetic Aperture Radar Data for Estimating Wetland Vegetation Aboveground Biomass in Coastal Louisiana." *Remote Sensing* 11 (21):2533. doi: 10.3390/rs11212533. Field work for this study benefited from projects supported by the National

Science Foundation via the National Center for Earth-Surface Dynamics (EAR-0120914), Frontiers of Earth Surface Dynamics (FESD, OCE-1135427), and the Coastal SEES program at LSU (EAR-1427389). This study further benefited from the Coastwide Reference Monitoring System (CRMS) Program's long-term monitoring network, funded by the Coastal Wetland Planning, Protection, and Restoration Act Program and the State of Louisiana. Lastly, I would like to thank Alexandra Christensen for her logistical support for the field work.

Chapter 4 is in preparation for journal submission, as the following citation notes: Jensen, Daniel, Kyle C. Cavanaugh, Marc Simard, Alexandra. Christensen, Andre Rovai, and Robert R. Twilley. In Progress. "Accretion-driven variation in vegetation composition and biomass in Louisiana's Wax Lake Delta." To be submitted to *Estuarine, Coastal and Shelf Science*.

I would like to thank each of my committee members for sharing their knowledge, and for their investment in this work and myself. To Gregory Okin for his great guidance and advice, and for lending his spectroscopic expertise to these studies. To Yongwei Sheng for his input, teaching skill, and direction in developing these projects. To Robert Twilley for lending his significant ecological knowledge that was invaluable in formulating and interpreting these studies, for hosting me in his lab at Louisiana State University, and for providing me with understanding and relationships that drove much of this research. To Marc Simard—whose brainchild much of this work springs from—for involving me in his brilliant work, creating a place on his research team for me, and investing much personal energy toward mentoring me. And finally to Kyle Cavanaugh for guiding me through this process, for creating an environment to succeed in, for imparting invaluable knowledge, lessons, and skills to me, and for too many other things to count. Nightmare stories are commonplace in the pursuit of a PhD, but with this committee I have had an ideal experience—far beyond what I initially hoped for.

VITA

## EDUCATION

**PhD, Geography, University of California, Los Angeles**
Expected 2019
Committee: Kyle Cavanaugh (Chair), Yongwei Sheng, Gregory Okin, Marc Simard (External, NASA Jet Propulsion Laboratory, California Institute of Technology), Robert Twilley (External, Louisiana State University)

**MA, Geography, California State University, Long Beach** 2014
Post-Baccalaureate Certificate in Geographic Information Science
Thesis title: *Spatial Analysis and Visualization in the NBA Using GIS Applications*
Supervisor: Dr. Hyowon Ban

**BA, University of California, Berkeley** 2011
Major: Geography (Focus: Earth System Science)
Minor: Earth and Planetary Science

## AWARDS AND FELLOWSHIPS

2019 NASA Postdoctoral Program Fellowship
2016-2019 NASA Earth and Space Sciences Fellowship
2016-2017 UCLA Graduate Research Mentorship Award
2014 CSULB Geography Department Distinguished Graduate Student

## REFEREED JOURNAL PUBLICATIONS

**Jensen, D.**, Cavanaugh, K.C., Simard, M., Christensen, A., Rovai, A., & Twilley, R.R. (*In Progress*). Accretion-Driven Variation in Vegetation Composition and Biomass in Louisiana's Wax Lake Delta. To be submitted to *Estuarine and Coastal Shelf Science*.

**Jensen, D.**, Cavanaugh, K.C., Simard, M., Okin, G.S., Castañeda-Moya, E., McCall, A., & Twilley, R.R. (2019). Integrating Imaging Spectrometer and Synthetic Aperture Radar Data for Estimating Wetland Vegetation Aboveground Biomass in Coastal Louisiana. *Remote Sensing*, 11(21), 2533.

**Jensen, D.**, Simard, M., Cavanaugh, K., Sheng, Y., Fichot, C.G., Pavelsky, T., & Twilley, R. (2019). Improving the Transferability of Suspended Solid Estimation in Wetland and Deltaic Waters with an Empirical Hyperspectral Approach. *Remote Sensing*, 11(13), 1629.

**Jensen, D.**, Reager, J.T., Zajic, B., Rousseau, N., Rodell, M., & Hinkley, E. (2018). The sensitivity of US wildfire occurrence to pre-season soil moisture conditions across ecosystems. *Environmental Research Letters*, 13(1).

**Jensen, D.J.**, Simard, M., Cavanaugh, K.C., & Thompson, D.R. (2017). Imaging Spectroscopy BRDF Correction for Mapping Louisiana's Coastal Ecosystems. *IEEE Transactions on Geoscience and Remote Sensing*, 56(3), 1739–1748.

Topp, S., Pavelsky, T., **Jensen, D.**, Simard, M., & Ross, M. (*In Review*). Remote sensing of inland water quality: A 50-year review of methods and applications. *Water*.

Thompson, D.R., Cawse-Nicholson, K., Erickson, Z. Fichot, C.G., Frankenberg, C., Gao, B., Gierach M.M., Green, R.O., **Jensen, D.**, Natraj, V., & Thompson, A. (2019). A unified approach to estimate land and water reflectances with uncertainties for coastal imaging spectroscopy. *Remote Sensing of Environment*, 231, 111198.

# Introduction

Coastal wetlands provide their surrounding regions with improved water quality, wildlife habitat, storm surge protection, and numerous other benefits that serve regional infrastructure and economies while promoting ecological sustainability (Twilley et al. 2016). In addition to these direct services, coastal wetlands absorb and store large quantities of atmospheric carbon dioxide, making them valuable "blue carbon" stocks. A wetland's net uptake of atmospheric carbon dioxide—i.e. carbon sequestration—can occur at rates over ten times greater than a tropical forest's typical sequestration rate as plant material and sediment-borne carbon are accreted in wetland soils (Chmura et al. 2003). This carbon sink's richness is driven by coastal wetlands' high net primary productivity and the carbon storage capacity of their soils (McLeod et al. 2011). Despite their provision of vital ecosystem services to neighboring coastal basins, many coastal wetlands face severe threats from anthropogenic disturbances and relative sea level rise (RSLR). Hydrocarbon and water extraction, pollution, drainage and land reclamation, and the engineering of river networks all threaten coastal wetland equilibrium relative to RSLR, whereby a vegetated marsh surface can sustain its own elevation (Morton et al. 2006; Day et al. 2003). These anthropogenic forcings increase the rate of subsurface material compaction, combining with natural soil subsidence to accelerate wetlands' subsidence rates. Subsidence combines with eustatic sea level rise (SLR) to make up RSLR, altering the water depth to which wetlands have adapted (Song et al. 2011; Krauss et al. 2009). By altering ecological variables such as salinity and hydroperiod, RSLR can destabilize wetlands and cause widespread submergence.

There are many environmental feedbacks that impact a wetland ecosystem's net primary productivity and carbon storage capacity, and thereby its ability to keep pace with RSLR. Primary among these are the influences of sea level, subsidence, vegetation type, primary productivity, and

sedimentation on a wetland's accretion potential and stability (Morris et al. 2002; FitzGerald et al. 2008). These factors see ongoing changes in coastal wetlands impacted by coastal engineering, climate change, and RSLR. A wetland's ability to vertically accrete—meaning the capture of sediment and biological matter for soil accumulation—material and maintain their elevation can thus be broken down into the organic and inorganic components that comprise net primary productivity and sedimentation rates (FitzGerald et al. 2008). Mineral sedimentation, for one, is controlled by waterborne mineral sediment deposited as water inundates and flows through wetlands, contributing to its vertical accretion rate. Tidal sedimentation rates are driven by tidal currents and suspended sediment loads, typically delivered by the ecosystem's fluvial systems, over short (i.e. tidal cycle or seasonal) timescales, and are further impacted by rainfall-induced resuspension of sediment, wave action, and episodic storm activity (FitzGerald et al. 2008). These processes are further altered in deltaic wetlands, where river stage is the primary control of the wetland surface elevation (Twilley et al. 2019). Over decadal timescales with a shifting climate, rising sea levels augment accretion rates as wetlands alter bioproductivity to maintain their elevational equilibrium (Morris et al. 2002). Wetland plant bioproductivity, then, contributes to organic peat production, forming the primary biological accretionary component. Organic sedimentation in wetlands occurs as organic plant matter is produced and buried in soil, then partially decomposed within the sediment layers. The deposited biomass stored within soils forms wetlands' most significant blue carbon sink, while the wetland vegetation's biomass modulates wetland response to RSLR and its potential for inundation and loss (Chmura et al. 2003). This is due to the critical role of vegetation biomass in the exchange of mineral sediments and carbon between inland regions and the coast, as vegetation structure affects sediment attenuation and accretion rates—creating a feedback with mineral sedimentation (Morris et al. 2002; Krauss et al.

2014). These factors determine a wetland's ability to counteract subsidence and keep pace with SLR, and thus influence a region's capacity for carbon sequestration and storage.

Ecological changes driven by RSLR are causing devastating impacts to Louisiana's coastal wetlands. Coastal Louisiana has seen almost 4000 $km^2$ converted to open water since 1956, with an ongoing rate of 44 $km^2$ of wetland area being lost each year (Barras et al. 2003; Twilley et al. 2016). While this historical record of wetland submergence indicate 44 $km^2$ being lost annually (Barras et al. 2003; Barras et al. 2008), analysis of the 30 years from 1988-2018 shows an estimated 1914.80 $km^2$ of total loss at an average rate of 61.77 $km^2$/year (Figure 1)—a clear increase from the historical rates. Sea level, land elevation, primary productivity, and sediment accretion are all changing in different parts of Louisiana's coastline, destabilizing much of Louisiana's coastal wetland ecosystems. While the Mississippi River Deltaic Plain (MRDP) has seen significant wetland loss due to the development of petroleum fields and land reclamation for agriculture (Morton et al. 2006), its wetlands' widespread isolation from its river network has caused the most significant ongoing degradation (Day et al. 2007). Prior to its extensive engineering, a natural network of distributaries meandered through the MRDP and delivered sediments to adjacent wetlands during flood periods (Kim et al. 2009). As the Mississippi River system is now highly channelized with reinforced levees and 15,000 km of canals cutting across the deltaic plain, much of the region's wetlands are disassociated from their natural sediment supply (Day et al. 2007). If wetland vegetation is unable to replace the lack of inorganic sediment input with sufficient organic matter deposition, surface soil elevation will not keep pace with RSLR and will eventually submerge (Morris et al. 2002). However, the Atchafalaya and Wax Lake deltas—distributaries of the Mississippi River—are themselves growing due to their concentrated sediment loads (Roberts et al. 2003), resulting in regimes of both land degradation and aggradation along the Louisiana

coast (Figure I-1). These dynamics, whereby RSLR has caused widespread wetland loss across the sediment-starved MRDP while new active deltas expand, provide an opportunity to examine accretionary processes and wetland changes in the face of different environmental conditions.

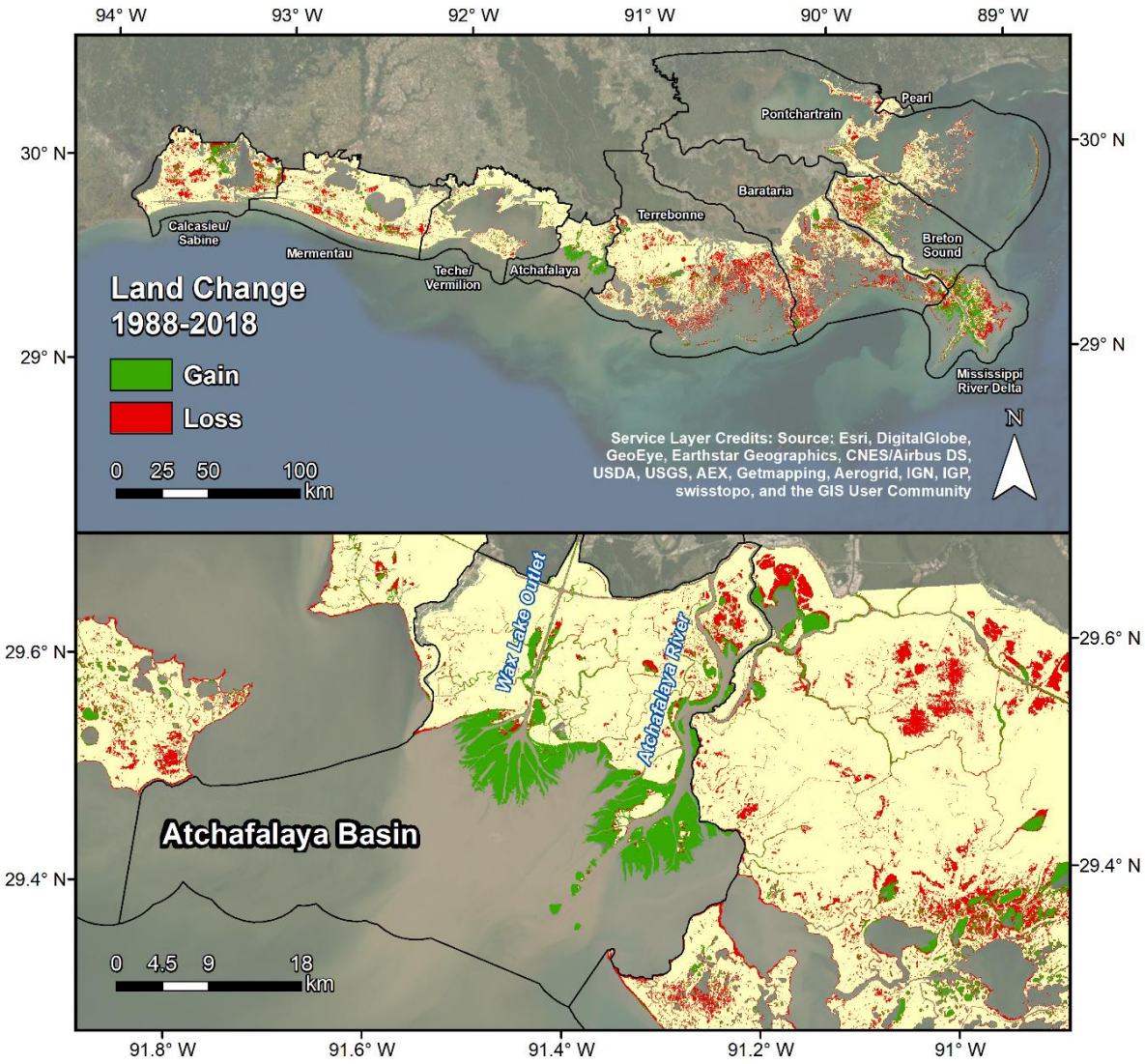


**Figure I-1.** Land change in Louisiana's coastal wetlands. This map was generated using the Landsat data catalog from 1988 and 2018. The average Normalized Difference Vegetation Index was calculated for each growing season (May-October), and a k-means cluster was applied to classify each averaged pixel value as either water or land. The output classifications were masked using National Wetlands Inventory boundaries and the shown drainage basins.

Satellite and airborne instruments offer the ability to attain regional-scale data that can be used to map wetland land-cover, hydrologic characteristics, and biophysical traits to assess environmental health. While these parameters can be measured in situ, it is often infeasible to conduct measurements on large spatial scales over which change is occurring. Spaceborne or airborne remote sensing offer more efficient tools for attaining regional-scale data that can be used to map wetland land-cover and assess environmental processes that contribute to wetland stability (Adam et al. 2010; Byrd et al. 2014). Many standard multispectral vegetation mapping methodologies are applied in wetland ecology, but the nature of wetlands often complicates the procedures and diminishes results in comparison with typical terrestrial vegetation. This is in part due to the prevalence of wet soil and water underlying vegetation in wetlands, which attenuate spectral information useful for distinguishing vegetation types (Zomer et al. 2008). Wetland vegetation types are more difficult to distinguish due to the complicating effects of local hydrology, underlying soil, more pronounced atmospheric vapor interference, and steep environmental gradients on observed spectral signatures (Lin and Liquan 2006; Adam et al. 2009; Adam et al. 2010). Each of these factors complicates the methodological complexity and the efficacy of wetland vegetation mapping with multispectral datasets. High-resolution imaging spectrometer data, however, has the potential to improve and broaden those capabilities, thereby enhancing the array of remote sensing applications for wetland ecology research.

Confounding these imaging spectroscopy data applications are various physical effects that must be corrected. Without accurate surface reflectance retrieval, mosaicking and analysis of different scenes is inhibited due to varying radiance retrievals between scenes. This is especially important in coastal wetlands as they frequently contain more variable atmospheric moisture content conditions (Lin and Liquan 2006; Adam et al. 2010). Additionally, the bidirectional

reflectance distribution function (BRDF) causes variations in spectral intensity across scenes. BRDF effects in imagery follow variations in surface anisotropy as a function of solar and instrument viewing geometry, including specular reflectance over a mirror-like surface, sunglint reflectance over water, volume scattering over leafy vegetation, and shadow-driven reflectance over forests (Lucht et al. 2000; Abuelgasim and Strahler 1994). As each surface type present in an image scene has different anisotropic scattering properties, each surface's BRDF has a different impact on the observed albedo (Lucht et al. 2000). While the BRDF contains biophysical information about the measured surface (Gao et al. 2003), accurately modeling and correcting the BRDF in a remotely sensed image enables the retrieval of actual surface albedo, so that surface properties can be analyzed independently of observation geometry (Lucht et al. 2000). Without adequate correction, BRDF effects create artefacts in mosaics of multiple images by degrading spatial uniformity of reflectance retrievals (Kennedy et al. 1997; Collings et al. 2010).

Numerous biological and hydrological parameters may be modeled and mapped with imaging spectrometer data collected over wetlands. Imaging spectrometer data allows land cover classification in general to be performed with greater accuracy, as the data contains more spectral information and enables the use of specific bands that show greater spectral separability than their multispectral counterparts (Yang et al. 2009; Demuro and Chisholm 2003; Hirano 2003). Species-level vegetation distribution mapping, which frequently leverage spectral libraries for each species, may also be possible with imaging spectroscopy. This frequently involves laboratory or in situ assessments of individual species spectral reflectance prior to image analysis for accurate species discrimination to take place at management-relevant scales (Zomer et al. 2008; Adam et al. 2010). The viability of such methods has been proven through lab experiments using spectrometers, spectral separability analyses, and the use of band selectors for optimal discrimination (Vaiphasa

et al. 2005; Vaiphasa et al. 2007; Wang and Sousa 2009). The increased spectral information provided by imaging spectrometers can also be applied to measure vegetation biomass with more effective models. Biomass is an important indicator of vegetation health and productivity, as well as a key parameter for models that quantify wetland response to sea level rise and resulting carbon storage loss. While passive remote sensing provides useful biochemical information for estimating vegetation biomass, active remote sensing—including radar—can provide complementary information about vegetation structure that may improve biomass estimation (Treuhaft et al. 2003). As net primary productivity varies with wetland elevation and hydroperiod (Twilley et al. 2019), biomass estimates can further be applied to assess how plant types respond to hydrological changes. In addition, biomass estimates are critical for modeling the exchange of sediments and carbon between delta channels and floodplains, as they are indicative of a marsh's sediment attenuation and accretion rates. To further study these processes, imaging spectrometers can be used to extract water quality characteristics and suspended sediment load from water spectra. Hydrology is a crucial control in wetland ecosystems that entails several parameters that may be effectively retrieved via spectroscopic measurements. Sediment loads supplied by the surrounding hydrologic system influence wetland stability as the soil surface must keep pace with RSLR through organic matter production and sediment capture producing sufficient accretion rates (Morris et al. 2002). Suspended sediment is frequently estimated with various multispectral instruments, but imaging spectrometers provide additional spectral data that can increase retrieval accuracy and transferability (Olmanson et al. 2013; Fichot et al. 2019). The environmental properties and processes above are important components for wetland accretion, and they can be estimated over large spatial scales with the application of remotely sensed data.

The following chapters use airborne imaging spectrometer and synthetic aperture radar data to model and map processes driving accretion over Louisiana's Atchafalaya and Terrebonne Basins (Figure 1). This represents a broader effort towards using remote sensing to produce landscape-scale estimates of accretionary processes and unifying those spatially-explicit estimates to project wetland elevation gain and risk of submergence. This dissertation accomplishes the following objectives:

- Develop an algorithm for correcting BRDF effects and produce spectrally consistent mosaics of surface reflectance from the airborne imaging spectrometer flightlines.
- Develop and validate an imaging spectroscopy model for estimating hydrologic suspended solid concentrations that is spatially and temporally transferable.
- Integrate imaging spectrometer measurements with synthetic aperture radar to improve estimates of wetland aboveground biomass.
- Determine the biochemical and physical structural characteristics that are associated with wetland aboveground biomass and resolvable from remote sensing data.
- Map the distribution of wetland vegetation species in the Wax Lake Delta and quantify successional patterns of key plant types that occurred with deltaic development and accretion.
- Assess how key wetland vegetation types' aboveground biomass varies by marsh platform elevation.

**References**

Abuelgasim, Abdelgadir A., and Alan H. Strahler. 1994. "Modeling Bidirectional Radiance Measurements Collected by the Advanced Solid-State Array Spectroradiometer (ASAS) over Oregon Transect Conifer Forests." *Remote Sensing of Environment* 47 (2): 261–75.

Adam, Elhadi, and Onisimo Mutanga. 2009. "Spectral Discrimination of Papyrus Vegetation (Cyperus Papyrus L.) in Swamp Wetlands Using Field Spectrometry." *ISPRS Journal of Photogrammetry and Remote Sensing* 64 (6): 612–20.

Adam, Elhadi, Onisimo Mutanga, and Denis Rugege. 2010. "Multispectral and Hyperspectral

Remote Sensing for Identification and Mapping of Wetland Vegetation: A Review." *Wetlands Ecology and Management* 18 (3): 281–96.

Barras, J., S. Beville, D. Britsch, S. Hartley, S. Hawes, J. Johnston, P. Kemp, Q. Kinler, A. Martucci, J. Porthouse, D. Reed, K. Roy, S. Sapkota, and J. Suhayda. 2003. *Historical and Projected Coastal Louisiana Land Changes: 1978-2050*. Reston, VA.

Barras, J.A., J.C. Bernier, and R.A. Morton. 2008. "Land area change in coastal Louisiana—A multidecadal perspective (from 1956 to 2006): U.S. Geological Survey Scientific Investigations Map 3019, scale 1:250,000", 14 p. pamphlet. Reston, VA.

Byrd, Kristin B., Jessica L. O'Connell, Stefania Di Tommaso, and Maggi Kelly. 2014. "Evaluation of Sensor Types and Environmental Controls on Mapping Biomass of Coastal Marsh Emergent Vegetation." *Remote Sensing of Environment* 149: 166–80.

Chmura, Gail L., Shimon C. Anisfeld, Donald R. Cahoon, and James C. Lynch. 2003. "Global carbon sequestration in tidal, saline wetland soils." *Global Biogeochemical Cycles* 17 (4):22-1—22-12.

Collings, Simon, Peter Caccetta, Norm Campbell, and Xiaoliang Wu. 2010. "Techniques for BRDF Correction of Hyperspectral Mosaics." *IEEE Transactions on Geoscience and Remote Sensing* 48 (10): 3733–46.

Day, John W., Alejandro Y. Arancibia, William J. Mitsch, Ana L. Lara-Dominguez, Jason N. Day, Jae-Young Ko, Robert Lane, Joel Lindsey, and David Z. Lomeli. 2003. "Using Ecotechnology to address water quality and wetland habitat loss problems in the Mississippi basin: a hierarchical approach." *Biotechnology Advances* 22 (1–2):135–159.

Day, J. W., D. F. Boesch, E. J. Clairain, G. P. Kemp, S. B. Laska, W. J. Mitsch, K. Orth, H.

Mashriqui, D. J. Reed, L. Shabman, C. a Simenstad, B. J. Streever, R. R. Twilley, C. C. Watson, J. T. Wells, and D. F. Whigham. 2007. “Restoration of the Mississippi Delta: lessons from Hurricanes Katrina and Rita”. *Science* 315 (5819):1679–84.

Demuro, Martina, and Laurie Chisholm. 2003. “Assessment of Hyperion for Characterizing Mangrove Communities.” In *Proceedings of the International Conference the AVIRIS 2003 Workshop*, 18–23.

Fichot, Cédric G., Bryan D. Downing, Brian A. Bergamaschi, Lisamarie Windham-Myers, Mark Marvin-Dipasquale, David R. Thompson, and Michelle M. Gierach. 2016. “High-Resolution Remote Sensing of Water Quality in the San Francisco Bay-Delta Estuary.” *Environmental Science and Technology* 50 (2): 573–83.

FitzGerald, Duncan M., Michael S. Fenster, Britt A. Argow, and Ilya V. Buynevich. 2008. “Coastal Impacts Due to Sea-Level Rise.” *Annual Review of Earth and Planetary Sciences* 36 (1):601–647.

Gao, F., C. B. Schaaf, A. H. Strahler, Y. Jin, and X. Li. 2003. “Detecting Vegetation Structure Using a Kernel-Based BRDF Model.” *Remote Sensing of Environment* 86 (2): 198–205.

Hirano, Akira, Marguerite Madden, and Roy Welch. 2003. “Hyperspectral Image Data for Mapping Wetland Vegetation.” *Wetlands* 23 (2): 436–48.

Kennedy, R. E., W. B. Cohen, and G. Takao. 1997. “Empirical Methods to Compensate for a View-Angle-Dependent Brightness Gradient in AVIRIS Imagery.” *Remote Sensing of Environment* 291 (62):277–291.

Kim, W., D. Mohrig, R. R. Twilley, C. Paola, and G. Parker. 2009. Is It Feasible to Build New Land in the Mississippi River Delta? *Eos Trans. AGU* 90 (42):373–374.

Krauss, Ken W, Karen L McKee, Catherine E Lovelock, Donald R Cahoon, Neil Saintilan, Ruth

Reef, and Luzhen Chen. 2014. “How Mangrove Forests Adjust to Rising Sea Level.” *The New Phytologist* 202 (1): 19–34.

Krauss, Ken W., Jamie A. Duberstein, Thomas W. Doyle, William H. Conner, Richard H. Day, L. Wayne Inabinette, and Julie L. Whitbeck. 2009. “Site Condition, Structure, and Growth of Baldcypress along Tidal/Non-Tidal Salinity Gradients.” *Wetlands* 29 (2): 505–19.

Lin, Yuan, and Zhang Liquan. 2006. “Identification of the Spectral Characteristics of Submerged Plant Vallisneria Spiralis.” *Acta Ecologica Sinica* 26 (4): 1005–10.

Lucht, Wolfgang, Crystal Barker Schaaf, and Alan H. Strahler. 2000. “An Algorithm for the Retrieval of Albedo from Space Using Semiempirical BRDF Models.” *IEEE Transactions on Geoscience and Remote Sensing* 38 (2 II): 977–98.

McLeod, Elizabeth, Gail L. Chmura, Steven Bouillon, Rodney Salm, Mats Björk, Carlos M. Duarte, Catherine E. Lovelock, William H. Schlesinger, and Brian R. Silliman. 2011. “A blueprint for blue carbon: Toward an improved understanding of the role of vegetated coastal habitats in sequestering CO2.” *Frontiers in Ecology and the Environment* 9 (10):552–560.

Morris, James T., P. V. Sundareshwar, Christopher T. Nietch, Björn Kjerfve, and D. R. Cahoon. 2002. “Responses of Coastal Wetlands to Rising Sea Level.” *Ecology* 83 (10): 2869–77.

Morton, Robert, Julie Bernier, and John Barras. 2006. “Evidence of Regional Subsidence and *Associated Interior Wetland Loss Induced by Hydrocarbon Production, Gulf Coast Region,* USA.” *Environmental Geology* 50 (2): 261–74.

Olmanson, Leif G., Patrick L. Brezonik, and Marvin E. Bauer. 2013. “Airborne Hyperspectral

Remote Sensing to Assess Spatial Distribution of Water Quality Characteristics in Large Rivers: The Mississippi River and Its Tributaries in Minnesota." *Remote Sensing of Environment* 130: 254–65.

Roberts, H. H., J. M. Coleman, S. J. Bentley, and N. Walker. 2003. "An Embryonic Major Delta lobe: A New generation of Delta Studies in the Atchafalaya-Wax lake Delta System." *Gulf Coast Association of Geological Societies Transactions* 53:690–703.

Song, Conghe, Brian L. White, and Benjamin W. Heumann. 2011. "Hyperspectral Remote Sensing of Salinity Stress on Red (Rhizophora Mangle) and White (Laguncularia Racemosa) Mangroves on Galapagos Islands." *Remote Sensing Letters* 2 (3): 221–30.

Treuhaft, Robert N., Gregory P. Asner, and Beverly E. Law. 2003. "Structure-Based Forest Biomass from Fusion of Radar and Hyperspectral Observations." *Geophysical Research Letters* 30 (9): 1472.

Twilley, Robert R., Samuel J. Bentley, Qin Chen, Douglas A. Edmonds, Scott C. Hagen, Nina S.N. Lam, Clinton S. Willson, et al. 2016. "Co-Evolution of Wetland Landscapes, Flooding, and Human Settlement in the Mississippi River Delta Plain." *Sustainability Science* 11 (4): 711–31.

Twilley, R. R., J. W. Day, A. E. Bevington, E. Castañeda-moya, A. Christensen, G. Holm, L. R. Heffner, R. Lane, A. Mccall, A. Aarons, S. Li, A. Freeman, and A. S. Rovai. 2019. "Ecogeomorphology of coastal deltaic floodplains and estuaries in an active delta: Insights from the Atchafalaya Coastal Basin." *Estuarine, Coastal and Shelf Science* 227 (August).

Vaiphasa, Chaichoke, Suwit Ongsomwang, Tanasak Vaiphasa, and Andrew K. Skidmore. 2005.

"Tropical Mangrove Species Discrimination Using Hyperspectral Data: A Laboratory Study." *Estuarine, Coastal and Shelf Science* 65 (1–2): 371–79.

Vaiphasa, Chaichoke, Andrew K. Skidmore, Willem F. de Boer, and Tanasak Vaiphasa. 2007. "A Hyperspectral Band Selector for Plant Species Discrimination." *ISPRS Journal of Photogrammetry and Remote Sensing* 62 (3): 225–35.

Wang, Le, and Wayne P. Sousa. 2009. "Distinguishing Mangrove Species with Laboratory Measurements of Hyperspectral Leaf Reflectance." *International Journal of Remote Sensing* 30 (5): 1267–81.

Yang, Chenghai, James H. Everitt, Reginald S. Fletcher, Ryan R. Jensen, and Paul W. Mausel. 2009. "Evaluating AISA + Hyperspectral Imagery for Mapping Black Mangrove along the South Texas Gulf Coast." *Photogrammetric Engineering & Remote Sensing* 75 (4): 425–35.

Zomer, Robert J., Antonio Trabucco, and Susan L. Ustin. 2008. "Building spectral libraries for wetlands land cover classification and hyperspectral remote sensing." *Journal of Environmental Management* 90 (7):2170–2177.

# Chapter 1

## Imaging Spectroscopy BRDF Correction for Mapping Louisiana's Coastal Ecosystems

### 1.1. Abstract

This study presents the Adaptive Reflectance Geometric Correction (ARGC), a Bidirectional Reflectance Distribution Function (BRDF) correction algorithm to address intensity gradients across remotely sensed images. The ARGC is developed and tested on data from the Airborne Visible/Infrared Imaging Spectrometer-Next Generation (AVIRIS-NG) collected over Louisiana's Atchafalaya River Delta, an area of complex wetland vegetation and waterbodies suited to AVIRIS-NG's fine spatial and spectral resolutions. Changing view and solar geometry, in conjunction with surfaces' anisotropic properties, impact a scene's observed reflectance. As traditional BRDF corrections may not be appropriate for wetland environments that have distinctive vegetation and hydrologic structures, more flexible functional corrections are shown to improve results. We compared two existing methods and the ARGC. The first method fits a quadratic function over image column averages, and the second is based on the inversion of the Ross-Thick and Li-Sparse kernels. Building upon the principles of these methods, the ARGC uses a multiple regression-based BRDF correction whereby the image's solar and view geometric descriptors form the independent variables. Each BRDF correction method was applied to the set of six partially overlapping AVIRIS-NG scenes. Assuming the actual surface reflectance of a given land cover type is independent of geometry, we used adjacent images' overlapping regions to quantitatively assess each correction method's efficacy. The ARGC produced the lowest overall Root Mean Square Difference and the lowest overlap Mean Absolute Difference across the vast

majority of bands. The ARGC is proposed as a practical new BRDF correction option for investigators using AVIRIS-NG data.

## 1.2. Introduction

Aerial and satellite images are influenced by the bidirectional reflectance distribution function (BRDF), which results in variation in observed reflectance or radiance intensity across an image. A surface's BRDF describes its unique reflectance properties as a function of solar incidence angle, instrument viewing geometry, and wavelength (Nicodemus et al. 1977; Schaepman-Strub et al. 2006). The BRDF's anisotropic reflectance properties arise from the physical structure of the measured surface, manifesting in effects such as specular reflectance over a mirror-like surface, sunglint reflectance over water, volume scattering over leafy vegetation, and shadow-driven reflectance over forests (Lucht et al. 2000; Abuelgasim and Strahler 1994). As each distinct surface present in an image has different anisotropic scattering properties, each surface's BRDF has a different impact on the observed albedo (Lucht et al. 2000). The BRDF is itself a signal containing biophysical information about the measured surface (Gao et al. 2003). However, if a sensor's view angle varies with respect to the angle of illumination during image acquisition, then some normalization must be applied if surface properties are to be analyzed independently of observation geometry.

In terms of remotely sensed imagery, then, the BRDF causes changes in illumination intensity across an image for each spectral band. Some wavelengths are influenced more than others, with BRDF effects being more prominent in visible and shortwave infrared (SWIR) regions, and weaker in the near-infrared (NIR) region (Schill et al. 2004). In order to compare data acquired from different geometries, investigators often adjust the surface reflectance to

approximate nadir-viewing spectra. Without adequate correction, BRDF effects inhibit seamless mosaicking of multiple images due to changes in the observed reflectance of a given region in adjacent images. These differences and apparent discontinuities make it difficult to maintain spatial uniformity of reflectance retrievals (Kennedy et al. 1997; Collings et al. 2010). However, modeling and correcting for BRDF effects is challenging due to the unique anisotropic properties of each observed surface that cause variability in BRDF effects across scenes containing distinct surface types. Given these impacts, a priori knowledge and pre-analysis of a study area can improve BRDF models (Li et al. 2001), leading to a widespread call for integrating a generalized land cover classification into the BRDF modelling process (Kennedy et al. 1997; Collings et al. 2010).

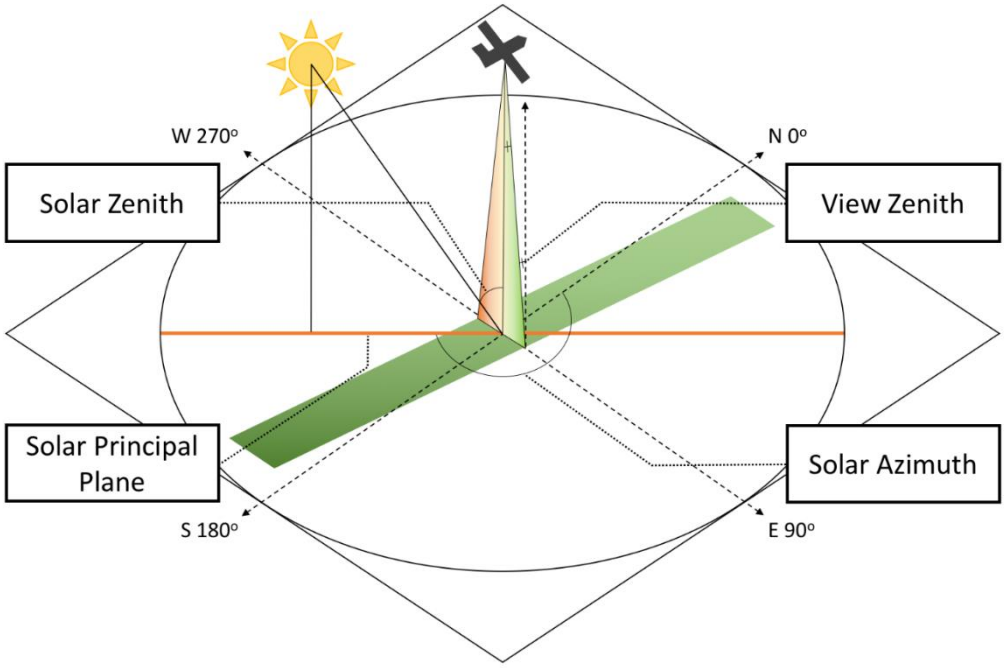


**Figure 1-1.** The solar and instrument geometry governing the BRDF. View zenith angle denotes the angle between zenith directly above the observation point and the instrument's vertical position, which varies for each pixel across the flightline. The varying across-track view zenith angles are represented by the red-green gradient within the instrument's view, also depicted in Figure 1-5. The solar zenith at each observed point is the angle between the zenith and the sun's vertical position. The solar azimuth is the angle between true north and the sun's horizontal position over the ground, while the solar principal plane (SPP) is the plane of direct surface illumination based on solar position. The angles depicted here roughly approximate those present in the data utilized in this study (Figure 1-2).

Several BRDF correction methods have been developed, each of which is based on different assumptions. These methods are typically semi-empirical, and are implemented by fitting a BRDF model to the image data and using it to remove the BRDF effects. Kennedy et al. (1997) first identified BRDF effects in Airborne Visible/Infrared Imaging Spectrometer (AVIRIS) data as a view angle-dependent, across-track pattern in illumination intensity. By averaging the reflectance values in each column of the vertically oriented image, whereby column number offers a proxy for view angle, a trend can be identified to approximate, and in turn remove, the BRDF effects. We will refer to this method as the "quadratic fit" approach based on the correction's functional form. While the quadratic fit method offers a univariate model for BRDF correction, kernel-based models describe bidirectional reflection with multivariate models that account for additional angular and surficial parameters. In addition to instrument view angle, kernel-driven models utilize the solar zenith and relative azimuth, angles which define the Solar Principal Plane (SPP) (Figure 1-1). The SPP is the plane of direct illumination, and its position relative to the flight line's orientation, if unaligned, largely determines a surface's observed BRDF shape and creates the need to normalize observed data to a constant view due to differences in sampling. Kernels, then, are functions that incorporate different BRDF components, including a volumetric term that describes the surface as features on top of a Lambertian surface and a geometric term that describes surface feature geometry and shadowing effects (Collings et al. 2010). The kernel parameters are estimated from image reflectance data to model the BRDF (Li et al. 2001; Wanner et al. 1995; Gao et al. 2003). While there are numerous kernels, each of which makes different structural assumptions about a surface (e.g. different leaf area index (LAI) constant values), the most prevalent method uses a linear combination of the Ross Thick and Li Sparse kernels (Lucht et al. 2000; Collings et al. 2010; Wanner et al. 1995; Hu et al. 1999; Colgan et al. 2012). The Ross Thick

kernel assumes a thick vegetation canopy and is thus based on an approximation for large LAI values. The Li Sparse kernel is based on modeled areal proportions sunlit vegetation crown, sunlit ground, shaded crown, and shaded ground reflectance. The quadratic fit and kernel methods each have tradeoffs. For example, the quadratic fit relies on a single simplistic non-geophysical variable to describe BRDF effects (Kennedy et al. 1997), while kernel functions rely on mathematical assumptions (Wanner et al. 1995) that may not be valid in certain situations, e.g. regions such as wetlands where the landcover is not well described by the selected kernel.

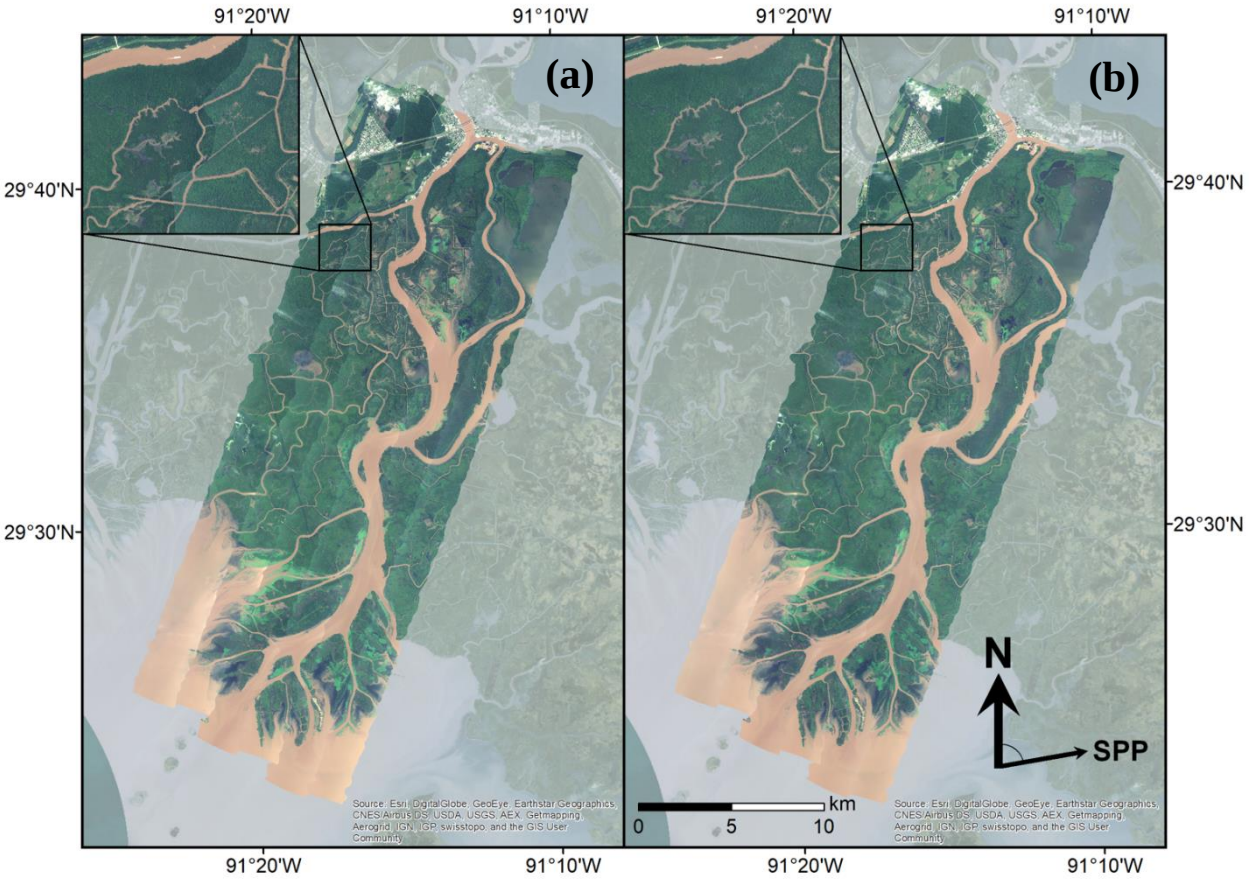


**Figure 1-2.** Mosaics with BRDF effects and applied correction. (a) A pre-correction true-color mosaic of the six AVIRIS-NG flightlines captured over the Atchafalaya River Delta. BRDF effects manifest in each scene as a general east-west variation in intensity, which are most visible along each seam where one scene's darker edge abuts the adjacent scene's lighter edge. (b) The mosaic after application of the multiple regression-based BRDF correction method developed in this study. The SPP's orientation during image acquisition ranged from 79.0 to 86.4 degrees, while the flightlines were oriented at 21 degrees.

While these BRDF correction techniques have been widely applied to multispectral data, far less work has been done with imaging spectroscopy data (Collings et al. 2010). Imaging spectroscopy, also known as hyperspectral imaging, provides a more complete measurement of the radiance spectrum for each location. In other words, it approximates a surface's complete radiance or reflectance spectrum for each image location or pixel, enabling remote measurement of physical, chemical, or biological characteristics.

The enhanced spectral coverage provided by imaging spectrometers is especially valuable for remote sensing of coastal wetlands. Wetland vegetation types are often difficult to distinguish due to the prevalence of wet soil and water (Zomer et al. 2009), the similarity of species' reflectance spectra, and highly variable local hydrology, soil, and atmospheric vapor interference (Lin and Liquan 2006; Adam et al. 2010). Additionally, wetland vegetation naturally has a high degree of spatial variability due to steep environmental gradients and resultant short ecotones (Adam et al. 2010; Adam and Mutanga 2009). High spatial and spectral resolution of imagery can help to mitigate these effects. However, remote sensing data collected over wetlands have a high degree of spatial complexity, with different vegetation communities, exposed sediment, and water systems intertwined throughout. This may complicate the BRDF effects in a given scene, and therefore requires an adaptive approach.

NASA's Airborne Visible/Infrared Imaging Spectrometer-Next Generation (AVIRIS-NG) provides very high spatial and spectral resolution. There is currently no standard BRDF correction algorithm for AVIRIS-NG data, and this paper provides a first assessment of existing and new methods for AVIRIS-NG data collected over the Atchafalaya River Delta in Louisiana. Building on this, this study's primary objective is to devise the optimal method for producing spectrally consistent AVIRIS-NG mosaic images, for which correcting a scene to nadir-viewing reflectance

is necessary. BRDF effects within coastal wetlands are examined by surface type and the corrected data's spectral consistency and integrity are quantified.

## 1.3. Data and Algorithm Development

### *1.3.1. Data*

AVIRIS-NG, the successor to the AVIRIS-Classic sensor that has been operational since 1986, is an airborne Visible Shortwave Infrared (VSWIR) spectrometer developed at NASA's Jet Propulsion Laboratory. The instrument measures 14-bit radiance between 380 to 2510 nm wavelengths with an approximately 5 nm spectral resolution (Hamlin et al. 2011; Thompson et al. 2014; Thompson et al. 2015). The data utilized for this study consist of six 432-band images with a 3.8 m spatial resolution collected over the Atchafalaya River Delta on June 6, 2015 with a 21 degree flightline orientation. Each raw dataset was atmospherically corrected using a physics-based algorithm (Thomposn et al. 2015; Bue et al. 2015) evolved from the ATmospheric REMoval (ATREM) codebase (Gao et al. 1993) to produce a surface reflectance image. These data were captured continuously from 2:23 PM to 3:47 PM. As the data were not captured at solar noon (12:04 PM) to approximate direct illumination, the solar zenith angle increased through the afternoon, thereby enhancing BRDF effects in the imagery. This is visible in the mosaic of the uncalibrated data (Figure 1-2), where the BRDF is apparent in the general East-West trend in illumination intensity. The discontinuities along the mosaic seams inhibit consistent analysis across multiple images. For vegetation mapping with airborne data, the BRDF introduces systematic discontinuities across mosaicked scenes via cross-track reflectance variation that can distort classification results (Colgan et al. 2012). The BRDF may have similar confounding effects

on wetland biomass and hydrologic suspended sediment concentration analyses through its impacts on observed spectral intensity.

### *1.3.2. Preclassification*

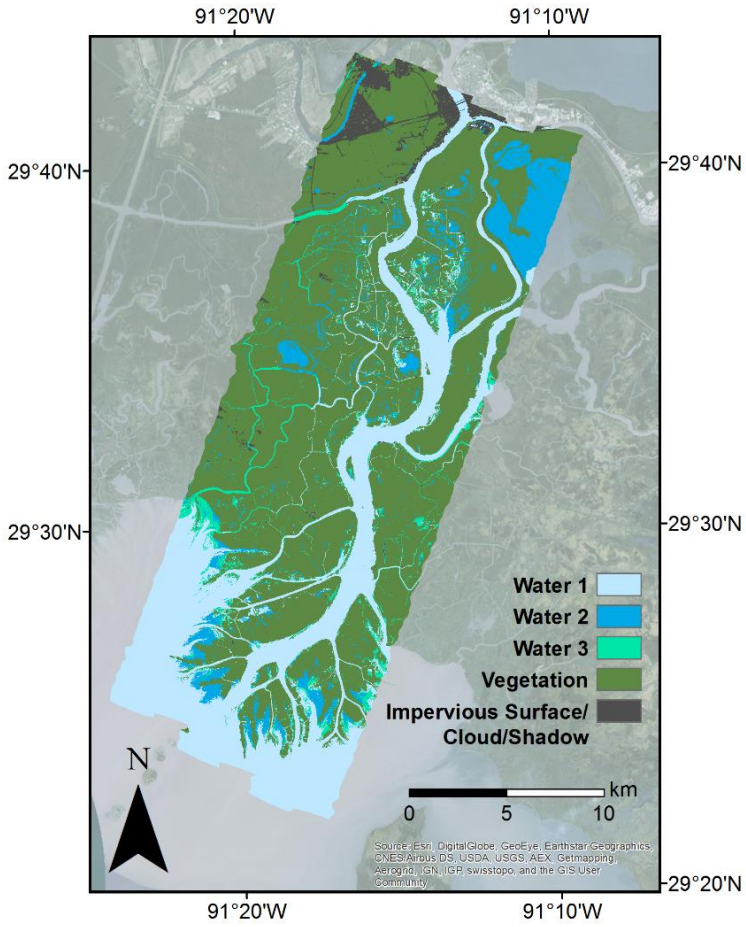


**Figure 1-3.** Land cover preclassification derived from the AVIRIS-NG scenes.

Any BRDF modeling procedure is impacted by the land cover type present in the data. Thus, many studies integrate *a priori* knowledge and a preclassification with broad land cover classes that have generally distinct anisotropic properties so that BRDF can be adaptively modeled separately for each class (Kennedy et al. 1997; Li et al. 2001). Our study site (Figure 1-2) contains a complex system of vegetation, impervious surfaces, and surface water. The spatial arrangement

of these land cover classes makes a general application of a single BRDF modelling process inappropriate, as the regional prominence of different features would distort the derived relationships with solar and instrument geometry. Consequently, we developed a preclassification scheme to identify regions of relatively uniform anisotropic properties for BRDF modeling. This preclassification utilized bands corresponding to 446.5, 486.5, 566.7, 661.8, 862.2, 1568.4, and 2234.6 nm along with normalized difference vegetation index (NDVI), and normalized difference water index (NDWI). These bands, which correspond to Landsat 8 band centers, were selected to reduce computational requirements otherwise needed for the 432 bands and proved sufficient for implementing a mask for clouds and impervious surfaces in a simple land cover classification. Clouds and impervious surfaces were removed by thresholding minimum values from the 446.5 nm band, 2234.6 nm band, and a normalized blue/green ratio. These designated pixels were then dilated to better encompass cloud cover. Shadows were removed with thresholds in NDVI, NDWI, and the 2234.6 nm band, using a spatial median filter to promote contiguous shaded regions. The remaining pixels were divided into water and vegetation, being the most spectrally distinct land cover types present, using a k-means classifier with 2 classes. Vegetation cover with a BRDF that significantly departs from the overall modeled BRDF will cause residual errors.

Vegetated land cover was left grouped in one class to develop an ensemble BRDF correction over the entire class. This region also contains several spectrally distinct water bodies. If the BRDF models were fitted to each resulting water class based on statistics gathered from all constituent pixels, different waterbodies' reflectances would be distorted. For example, if water were treated as a single class for BRDF correction, the large freshwater lake in the northeast would appear brighter than if corrected separately due to the Atchafalaya River's prevalence. Due to the high sediment load within the river's surface waters, the reflectance measurements in other surface

waters would be altered by correction algorithms that make use of a mean reflectance term and may impact trends modeled by each correction method. Accordingly, we created three spectrally distinct water subclasses from the first classification's resultant water pixels, again using a k-means classifier. These three waterbody types were visually identified and generally corresponded to sediment-laden river and gulf water, low-sediment lakes and channels, and waterbodies with submerged vegetation. BRDF corrections were then performed separately for each class in Figure 1-3.

### *1.3.3. Quadratic Fit*

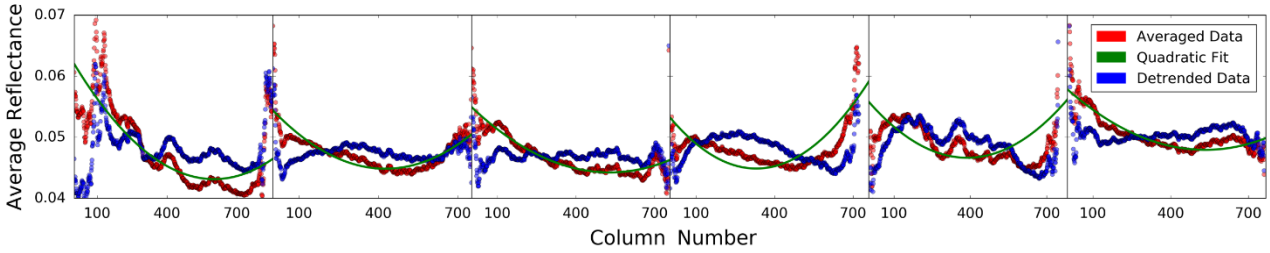


**Figure 1-4.** Applying the quadratic fit correction. This figure shows an example of the uncorrected column averages, quadratic function fit, and corrected column averages across the six scenes. These plots were derived from the 661.8 nm band over the vegetation class.

This study compared three BRDF correction methods, implementing two established methods and a newly developed algorithm. The first established method involved fitting a quadratic function to average column intensity values across the scene. This approach examined changes in brightness as a function of instrument view angle in order to approximate BRDF across each spectral band (Kennedy et al. 1997). In this method, each pixel value within a column of a vertically-oriented (i.e. the airplane path oriented straight up) scene before orthorectification is averaged and the column number served as a proxy for view zenith angle, a primary driver of the BRDF. In this case, other solar angles were assumed to remain constant over the length of the

scene. Fitting a quadratic function to these averaged column values estimated BRDF effects in that scene (Kennedy et al. 1997). We then subtracted the modeled BRDF from the observed data in order to estimate the equivalent nadir-viewing reflectance (Figure 1-4). This quadratic fitting process was applied separately for the vegetation and water classes to account for their distinct BRDF effects and then repeated for all 432 bands individually in each scene.

### *1.3.4. Kernels*

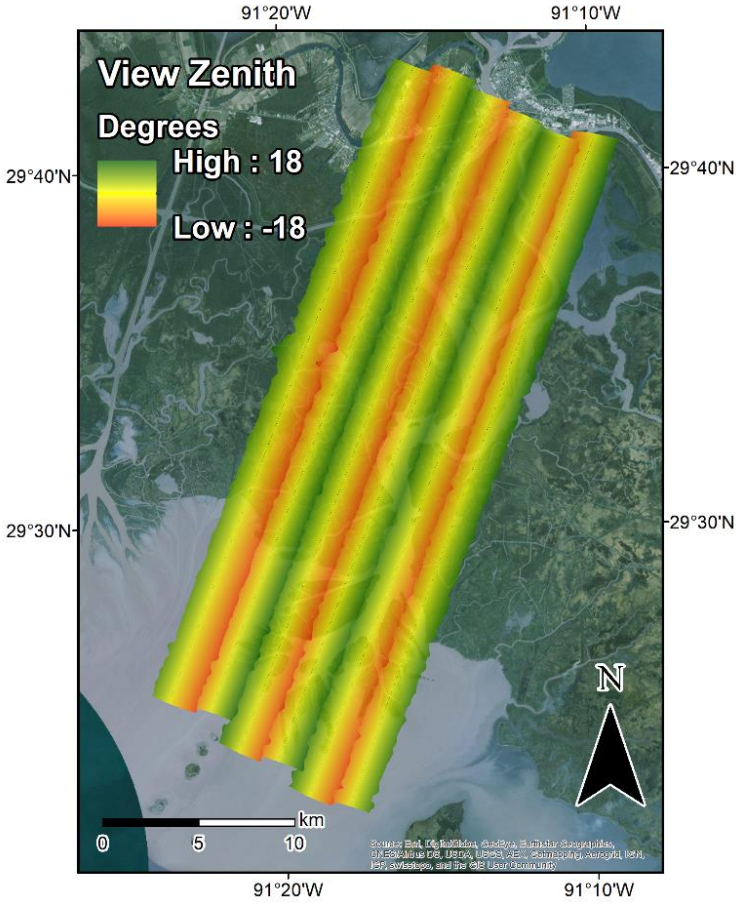


**Figure 1-5.** The view zenith angles over the footprint of each AVIRIS-NG image.

Whereas the quadratic fit-based correction method used column averages as a proxy for view zenith angle, the kernel and regression-based methods were parameterized with a combination of view zenith, solar zenith, and solar azimuth angles. Solar zenith and solar azimuth

angles for either end of each scene were calculated using each scene's start and end collection times and coordinates. Using the scene's footprint, the start and end values for each solar angle were interpolated to approximate the zenith and azimuth at each pixel at the time of capture (Figure 1-5). The actual angle used for calculating BRDF kernel values or input into a BRDF regression model is relative azimuth angle—the angle between the solar azimuth and instrument azimuth. As the airborne instrument is constantly above the scene center and the across-track distance is relatively small, the instrument azimuth angle is assumed to be a constant 0 degrees. Therefore, relative azimuth angle is the solar azimuth angle subtracted from 0. Given the AVIRIS-NG's 36-degree field of view, the view zenith angle matrix was generated by setting the values in each of the unorthorectified scene's columns evenly from -18 to 18, starting on the edge corresponding to the airplane's left (Figure 1-5).

The use of kernels in semi-empirical BRDF models is perhaps the most widely applied method, often implemented as a linear combination of the Ross Thick and Li Sparse kernels (Lucht et al. 2000; Collings et al. 2010; Wanner et al. 1995; Hu et al. 1999; Colgan et al. 2012). The Earth Observation Land Data Assimilation System's (EO-LDAS) (Lewis et al. 2012) Python package was implemented to calculate Ross Thick and Li Sparse kernel values using the view zenith, solar zenith, and relative azimuth arrays. The Ross Thick and Li Sparse kernels respectively represent volumetric and geometric reflectance components (Collings et al. 2010). These geometric arrays were then disaggregated by cover type (Figure 1-3) and the corresponding kernel values were inverted with a least squares operation against the measurement for each spectral band. This process returned a kernel weight value for each derived model. The following equation (1), taken from Collings et al. (2010), was then implemented to approximate the nadir-viewing signal:

$$\hat{\rho}_{ijl} = \rho_{ijl} - \sum_{k=1}^{K} \beta_{ijk}(H_k(\xi_{il}) - \bar{H}_{ik}) \quad (1)$$

whereby $\hat{\rho}_{ijl}$ is the estimated measurement when a given pixel of a given band is viewed from at nadir, $\rho_{ijl}$ is the corresponding observed reflectance, $K$ is the kernel, $\beta_{ijk}$is the kernel weight, $H_k(\xi_{il})$ is the Kth kernel value, and $\bar{H}_{ik}$ is the Kth kernel mean value for the given spectral band and class. The $\beta_{ijk}(H_k(\xi_{il}) - \bar{H}_{ik})$ term in (1) is itself the modeled BRDF. It is calculated for each land cover class in a given scene, the modeled BRDF is subtracted from the observed reflectance for each band, returning a corrected image.

### *1.3.5. Multiple Regression*

Lastly, this study developed the Adaptive Reflectance Geometric Correction (ARGC), a multiple-regression approach for BRDF modelling that employs elements from the two established methods. Like the quadratic fit-based method it empirically derived an equation from geometric inputs, but made use of the same three angles used in the kernel method as independent variables to provide a more flexible model. These angular inputs were chosen to mimic the Ross Thick-Li Sparse kernel parameters and offer a direct comparison between a purely empirical approach and a physical model approach. However, the multiple regression method did not require the physical and structural assumptions that underlie kernel models, instead assuming that the regression model for each surface type captured the physical characteristics that impacted its BRDF shape. For each class and each band, an Ordinary Least Squares multiple regression model, which minimizes the resultant residuals' sum of squares, was derived whereby the observed reflectance values formed the dependent variable and the view zenith, solar zenith, and relative azimuth angles each formed the independent variables. In doing so, the effects of the flightline's orientation are largely

accounted for by the view zenith angle as the observed across-track variation in illumination intensity is impacted by the SPP's relative orientation. The model reflectance functions were generated from the three input geometry arrays followed by subtraction of the mean reflectance $\bar{\rho}$ for each class, as follows:

$$BRDF = x_1(VZA) + x_2(RAA) + x_3(SZA) + x_4 - \bar{\rho} \quad (2)$$

In (2), $x_1$-$x_3$ denote the coefficients for each geometric variable, while $x_4$ is the modeled intercept value and $\bar{\rho}$ is average reflectance. As the BRDF can be considered as an additive effect on the true radiance or reflectance of pixels (Collings et al. 2010), the modeled BRDF array was then subtracted from the original band to correct its effects.

### *1.3.6. Statistical Analysis*

After each of the six scenes were processed with all three BRDF correction methods, we compared spectral consistency and integrity of the corrected data. Spectral consistency refers to how well multiple measurements of the same spectra match. Given a particular ground sample, the measured pixel for the sample in two images should present the same spectrum in each after an ideal correction, irrespective of viewing and illumination geometry. Spectral consistency is thus best measured by comparing data from scene overlaps. Spectral integrity describes how well pixels' spectral shapes are preserved after the BRDF correction (Collings et al. 2010). It is important to consider the application in weighing the importance of these two factors. As this study aimed to optimize a mosaicking of several scenes, higher spectral consistency took precedence over integrity.

Visually, a high degree of spectral consistency will result in an improved nearly-seamless mosaic wherein the illumination intensity differences along abutting scene edges is minimized.

That is, a given observation will exhibit similar spectral intensity irrespective of viewing geometry. Aside from visual inspection, the overlapping regions of each scene pair allow the improvement in spectral consistency to be quantified. For all three correction methods, all overlap pixel values were extracted from each corrected scene along with the corresponding uncorrected scene. The Mean Absolute Difference (MAD) in the overlap between the corrected scene pairs provides a measure of spectral consistency improvement across all bands when compared to that of the uncorrected data. For both the water and vegetation classes in each overlap region, the pixel values in each band were averaged for both scenes and differenced. The absolute value of the five overlap region difference values were averaged to calculate the MAD for each band. A MAD closer to zero indicates a higher degree of spectral consistency. The overlap Root Mean Square Difference (RMSD) ratio provides an additional measure of spectral consistency for each correction method as it measures the departure of the local reflectance spectra from the general correction BRDF model, which results from structurally complex land cover. The RMSD for each corrected scene pair overlap was calculated from all pixels across the 350 designated good bands in accordance with (3) and (4):

$$\text{RMSD} = \frac{\sum_{n=1}^{n} RMS_1 - RMS_2}{n} \tag{3}$$

$$\text{RMSD Ratio} = \frac{\text{RMSD}_{corrected}}{\text{RMSD}_{uncorrected}} \tag{4}$$

In (3), *n* designates each of the five overlaps while $RMS_1$ and $RMS_2$ are the Root Mean Square (RMS) of the two scenes' pixel values within each overlap, respectively. 82 of the 432 AVIRIS-NG bands were removed from analysis, as they were located in areas of the spectrum where atmospheric absorption was high. We divided the RMSD after the correction by the RMSD for the

corresponding uncorrected data and averaged the ratios to assess accuracy for the scene (4). This assessment followed the methodology outlined by Collings et al. (2010). Values lower than one indicate improved spectral consistency, an RMSD ratio of one indicates no relative improvement, and values greater than one indicate degraded consistency.

Spectral angle, when calculated based on each corrected pixel spectrum paired with the corresponding uncorrected pixel spectrum as the reference, provides a measure of the change in the overall spectral shape (Collings et al. 2010; Rashmi et al. 2014). As the spectral angle is unaffected by BRDF effects, this provides a measure of spectral integrity by which smaller values indicate less spectral distortion (Collings et al. 2010). We calculated spectral angle arrays for each corrected dataset by implementing the spectral angle equation noted by Rashmi et al. (2014):

$$\alpha = \cos^{-1}\left(\frac{\sum_{i=1}^{nb} t_i r_i}{\sqrt{\sum_{i=1}^{nb} t_i^2}\sqrt{\sum_{i=1}^{nb} r_i^2}}\right) \quad (5)$$

Where *nb* is the number of bands, *t* is each pixel spectrum, *r* is the reference spectrum, and $\alpha$ is the resultant spectral angle. Each uncorrected pixel is thus the reference spectrum and the corresponding corrected pixel is the target spectrum. The Root Mean Square (RMS) for each scene's spectral angle array was then calculated, and the six RMS values were averaged for each method.

### 1.4. Methodological Comparison Results

Across the majority of bands, the multiple regression-based algorithm produced results with the lowest MAD (Figure 1-6). Of the 350 designated good bands, 307 showed the lowest difference value for the multiple regression correction, 19 for quadratic fitting, and 24 for the kernel-based method. The multiple regression correction's effects in RGB bands are also visible

in Figure 1-1, which provides a visualization of the improvement in the processed mosaic. Additionally, the multiple regression-based correction indicates the greatest overall improvement in spectral consistency with an overlap RMSD ratio of 0.93, and a significant improvement in vegetation specifically with a ratio of 0.14 (Table 1-1), corroborating the improvement shown in Figure 1-6. Separating correction algorithm performance into water and vegetation components shows greatest overlap error reduction by the ARGC generally. While the MAD values across all wavelengths in water show marginal improvement by the ARGC compared to other methods over water, along with an RMSD ratio of 1.05, the corresponding results over vegetation show greatly increased spectral consistency.

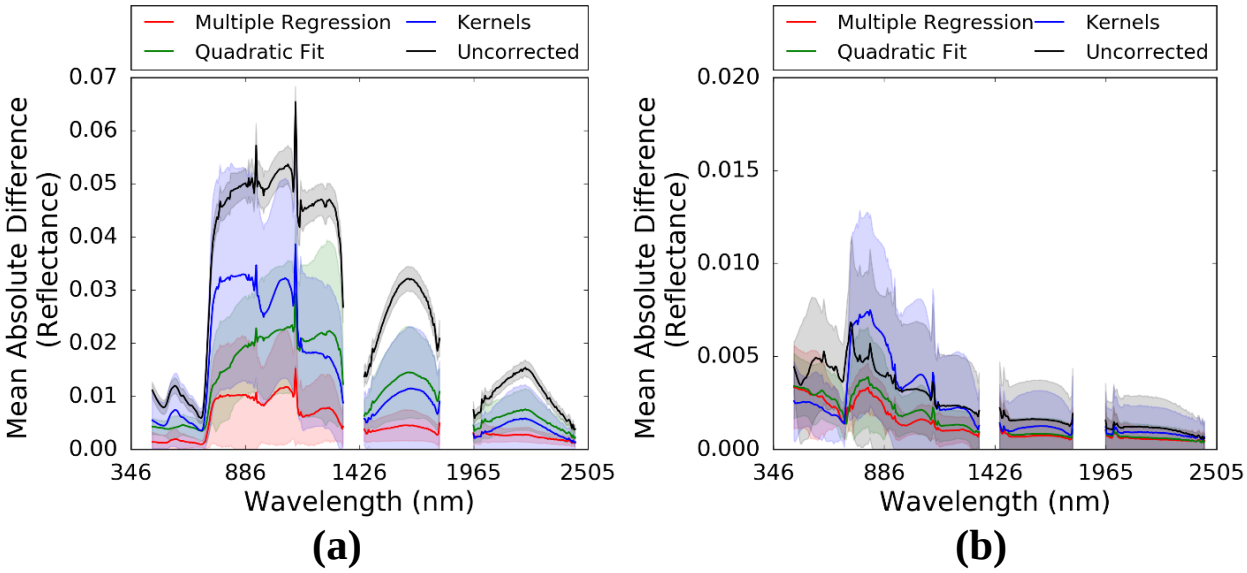


**Figure 1-6.** Spectral consistency assessment for the corrections. Mean absolute difference of reflectance across each band for each of the corrected and uncorrected datasets in (a) vegetation and (b) water. Shaded area shows one standard deviation around the mean value.

The spectral angle mean values for each corrected dataset are reported in Table 1-2. These figures each indicate that the quadratic fit correction method resulted in the lowest overall spectral angle values, while the multiple regression resulted in the highest values. However, the spectral

angle mean for the multiple regression dataset was only slightly higher than that of the kernel-based method across each class, and the spectral angles are overall low. Further, spectral angle means and their confidence intervals, while greater overall and more variant over water, are low and less variant within the vegetation class.

**Table 1-1.** Spectral consistency assessment

| | Overlap RMSD Ratio | |
|---|---|---|
| | Water | Vegetation |
| Quadratic Fit | 1.03 | 0.41 |
| Kernels | 0.95 | 0.52 |
| Multiple Regression | 1.05 | 0.14 |

**Table 1-2.** Spectral integrity assessment

| | Spectral Angle Mean (95% Confidence Interval) | |
|---|---|---|
| | Water | Vegetation |
| Quadratic Fit | 0.03 (0.03006, 0.03009) | 0.02 (0.01981, 0.01983) |
| Kernels | 0.05 (0.04652, 0.04646) | 0.03 (0.02503, 0.02505) |
| Multiple Regression | 0.05 (0.05008, 0.05012) | 0.03 (0.02674, 0.02676) |

### 1.5. Assessment and Implementation

This study quantified and assessed the overall performance of different BRDF correction methods as applied to AVIRIS-NG data. Collings et al. (2010) use of overlap, spatial smoothness, and spectral smoothness penalty terms to produce optimized mosaics. These terms require significant additional computation, processing, and interpretation tailored to a given dataset. This

study, conversely, does not apply penalty terms in order to objectively assess correction performance. Instead, it provides an assessment of a generalized BRDF algorithm that can be broadly applied to AVIRIS-NG data.

Figure 1-6 shows that the ARGC's multiple regression correction method most effectively reduces the discrepancy in scene overlaps, enabling view-invariant reflectance estimates. The greatest MAD in the uncorrected data exists over the NIR region, which then also sees the greatest error reduction by the multiple regression correction. Schill et al. (2004) show that NIR wavelengths within 1100–1300 nm are least affected by BRDF effects within vegetation canopies, while those between 2080 and 2430 nm are most impacted. Figure 1-7 corroborates these findings, showing that the NIR region has the lowest overall remaining overlap error. As the BRDF is least impactful in this region (Schill et al. 2004), it follows that the regression-based algorithm most effectively detects and corrects BRDF effects here.

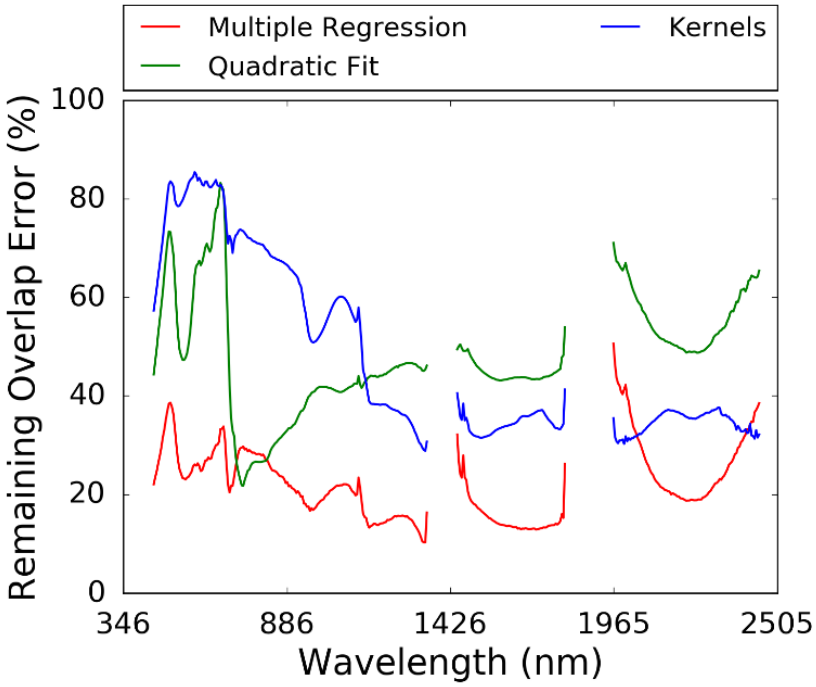


**Figure 1-7.** Post-correction remaining overlap error (%). Calculated across all bands and all pixels for each correction method. These error values are calculated by dividing the MADs for each method by that of the uncorrected data in Figure 1-6.

However, the visible and SWIR regions—especially the second SWIR region from 2080-2430 nm—show relatively higher remaining overlap error. In the visible and SWIR regions, lower amounts of light are reflected compared to the NIR, in turn lowering scattering effects. Higher scattering causes the distribution of BRDF effects to be more azimuthally symmetric (Schill et al. 2004), and thus more easily detected and corrected. SWIR correction performance may also be prone to variance in signal to noise ratio (SNR). The multiple regression correction's efficacy across these spectral regions, more so than the quadratic fit and kernel corrections, largely falls in line with vegetation scattering mechanisms that govern the BRDF.

There are several reasons these methods perform differently. As previously discussed, the multiple regression and quadratic fit methods both display the same general error reduction profile across the visible, NIR, and SWIR regions (Figure 1-6). However, it is likely that the multiple regression correction reduced significantly more error than the quadratic fit method because it included more angular variables relevant to the BRDF and provided more free parameters for model complexity. While the view zenith has the largest bearing on the model, the solar zenith and azimuth influence the BRDF shape and across-track intensity values differently at either end of the scene due to their change over the instrument's collection period. Utilizing these three angles together in the ARGC provides the optimal approximation of the BRDF, though limiting the number of independent observations by excising either solar angle in the same statistical approach would sufficiently approximate the BRDF's changing shape. While solely utilizing view zenith in a univariate regression model would yield similar results to the implemented quadratic fit method, discarding solar angle information would impact the spectral consistency across scene overlaps.

These same angular variables are used in the kernel method, though, which underperformed according to the MAD. This may partly be due to the Ross Thick and Li Sparse

kernels being developed with different structural assumptions and mathematical constants tuned to dryland vegetation parameters (Wanner et al. 1995). While other kernels, such as the Ross Thin, Li Dense, and Roujean, have been used, the combination of the Ross Thick and Li Sparse kernels has seen the widest use and demonstrated effectiveness (Wanner et al. 1995; Collings et al. 2010). Sunglint reflectance dominates BRDF effects over water (Lucht et al. 2000), and the prevalence of water in the Atchafalaya River imagery may degrade the kernel correction's quality over the water classes. While the kernel method performed well over water for visible bands, it underperforms in the NIR and SWIR regions relative to other methods. This relative quality suggests that the kernel functions themselves do not properly account for spectral features that largely attenuate radiation rather than reflecting or scattering it. The limited observation angular distribution of each flightline may also impact the efficacy of the kernels' inversion results. It is important to note that while the multiple regression method produces the lowest error in the overlap, and thus the greatest spectral consistency, it produces the highest spectral angle RMS and thus the lowest spectral integrity. This is likely due to the relative constraints of each approach. Statistically, the multiple regression modeling process has considerable freedom in deriving the modeled BRDF for each band, though the kernel model is constrained by additional biophysical parameters, e.g. LAI. The quadratic fit is also constrained by its single angular variable and forced function shape. These constraints help to explain its greater spectral integrity, though the freedom associated with multiple regression is a key factor in its significantly smaller resultant overlap differences. Likewise, the multiple regression model is more prone to producing outlier pixels, especially where noise such as distortion effects along scene edges are present, likely due to a slightly increased propensity for overfitting to noise in the data resulting from its flexibility. These outlier pixels in turn produce a greater spectral angle RMS than other methods. However, for the

purposes of developing a near-seamless mosaic for further analysis the reduction in overlap error was deemed the more important metric (Figure 1-2).

The ARGC methodology developed for this study was specifically written to assess the data collected over the Atchafalaya River. Further analysis and algorithm development must be performed for a generalized AVIRIS-NG BRDF correction. A key challenge in BRDF modelling is discriminating between actual features within the scene and those induced by geometric effects so as not to erroneously influence the model. As the Atchafalaya River is made up of a complex of vegetated wetlands, water, and developed surfaces, it was necessary for this study to divide the surface types of interest due to their different BRDFs. All vegetation was grouped to develop an ensemble BRDF correction, though residual errors may persist due to vegetation cover heterogeneity. Other datasets may have a variety of vegetation BRDFs based on differing cover types, creating an issue for a universal correction algorithm as the number of land cover classes in the *a priori* classification may vary with different landscapes. In those circumstances, vegetation could be clustered into finer subcategories using an unsupervised strategy. It should be noted that any *a priori* classification or clustering approach must result in groupings that sufficiently disaggregate an image so as to not distort their constituent land cover type spectra while also remaining sufficiently broad to limit BRDF-induced classification errors. Classification errors would otherwise skew the BRDF correction, as the reflectance values from incorrectly designated pixels would affect the fitted model. Additionally, while this study examined a wetland region with only marginal topographic effects, other datasets will be impacted by topographic illumination effects. Topography must also be addressed in a generalized algorithm, or the resultant shading would skew the regression model. This may be addressed by implementing slope and aspect, derived from a digital elevation model, as independent variables in the multiple

regression model. While these issues must be addressed to improve on and generalize the multiple regression algorithm for BRDF correction of AVIRIS-NG data, the method developed in this study has proven effective for correcting and mosaicking data in Louisiana's coastal wetlands and may be applied to imaging spectroscopy studies in other coastal wetlands.

### 1.6. Conclusion

This study outlines the development and assessment of BRDF correction methods for AVIRIS-NG data collected over Louisiana's Atchafalaya River and its surrounding wetlands. We investigated BRDF kernels, quadratic functions, and the multiple regression-based ARGC. The multiple regression method best reduced the difference in reflectance measurements of adjacent scene overlaps, producing the mosaic with the highest spectral consistency and lowest discrepancies among scene edges.

Airborne imaging spectrometers, including AVIRIS-NG, provide the high spatial and spectral resolution data that enable analysis of wetland health and hydrology. Imaging spectrometer data can improve wetland vegetation classification effectiveness *vis a vis* multiband observations, with spectral measurements enabling statistical analyses and algorithms such as spectral separability analysis and spectral mixture analysis. These methods can provide greater accuracy and additional compositional insight (Hirano et al. 2003; Yang et al. 2009; Demuro and Chisholm 2003; Vaiphasa et al. 2005; Vaiphasa et al. 2007; Wang and Sousa 2009; Byrd et al. 2014), especially as they concern analysis of coastal wetland degradation and hydrologic changes in the face of increasingly stressed coastal environments (Chen et al. 1992; Sterckx et al. 2007; Olmanson et al. 2013; Fichot et al. 2016; Allison et al. 2012). High resolution imaging spectrometer data has great utility for addressing these concerns, though imaging spectroscopy in

general faces limitations in data availability, computational intensiveness, and user-readiness. BRDF correction is a key part of overcoming these limitations as BRDF effects inevitably influence analyses, particularly when large mosaics of multiple flightlines are needed. The multiple regression method developed in this study is proposed as an operational tool for correcting BRDF effects observed in AVIRIS-NG data to enable further environmental analysis and promote the applicability of this rich dataset.

### 1.7. References


Abuelgasim, Abdelgadir A., and Alan H. Strahler. 1994. "Modeling Bidirectional Radiance Measurements Collected by the Advanced Solid-State Array Spectroradiometer (ASAS) over Oregon Transect Conifer Forests." *Remote Sensing of Environment* 47 (2): 261–75.

Adam, Elhadi, and Onisimo Mutanga. 2009. "Spectral Discrimination of Papyrus Vegetation (Cyperus Papyrus L.) in Swamp Wetlands Using Field Spectrometry." *ISPRS Journal of Photogrammetry and Remote Sensing* 64 (6): 612–20.

Adam, Elhadi, Onisimo Mutanga, and Denis Rugege. 2010. "Multispectral and Hyperspectral Remote Sensing for Identification and Mapping of Wetland Vegetation: A Review." *Wetlands Ecology and Management* 18 (3): 281–96.

Allison, Mead A., Charles R. Demas, Bruce A. Ebersole, Barbara A. Kleiss, Charles D. Little, Ehab A. Meselhe, Nancy J. Powell, Thad C. Pratt, and Brian M. Vosburg. 2012. "A Water and Sediment Budget for the Lower Mississippi-Atchafalaya River in Flood Years 2008-2010: Implications for Sediment Discharge to the Oceans and Coastal Restoration in Louisiana." *Journal of Hydrology* 432–433 (February): 84–97.

Bue, Brian D., David R. Thompson, Michael Eastwood, Robert O. Green, Bo Cai Gao, Didier

Keymeulen, Charles M. Sarture, Alan S. Mazer, and Huy H. Luong. 2015. “Real-Time Atmospheric Correction of AVIRIS-NG Imagery.” *IEEE Transactions on Geoscience and Remote Sensing* 53 (12): 6419–28.

Byrd, Kristin B., Jessica L. O’Connell, Stefania Di Tommaso, and Maggi Kelly. 2014. “Evaluation of Sensor Types and Environmental Controls on Mapping Biomass of Coastal Marsh Emergent Vegetation.” *Remote Sensing of Environment* 149: 166–80.

Chen, Zhimin, Paul J. Curran, and Jim D. Hansom. 1992. “Derivative Reflectance Spectroscopy to Estimate Suspended Sediment Concentration.” *Remote Sensing of Environment* 40 (1): 67–77.

Colgan, Matthew S., Claire A. Baldeck, Jean baptiste Féret, and Gregory P. Asner. 2012. “Mapping Savanna Tree Species at Ecosystem Scales Using Support Vector Machine Classification and BRDF Correction on Airborne Hyperspectral and LiDAR Data.” *Remote Sensing* 4 (11): 3462–80.

Collings, Simon, Peter Caccetta, Norm Campbell, and Xiaoliang Wu. 2010. “Techniques for BRDF Correction of Hyperspectral Mosaics.” *IEEE Transactions on Geoscience and Remote Sensing* 48 (10): 3733–46.

Demuro, Martina, and Laurie Chisholm. 2003. “Assessment of Hyperion for Characterizing Mangrove Communities.” In *Proceedings of the International Conference the AVIRIS 2003 Workshop*, 18–23.

Fichot, Cédric G., Bryan D. Downing, Brian A. Bergamaschi, Lisamarie Windham-Myers, Mark Marvin-Dipasquale, David R. Thompson, and Michelle M. Gierach. 2016. “High-Resolution Remote Sensing of Water Quality in the San Francisco Bay-Delta Estuary.” *Environmental Science and Technology* 50 (2): 573–83.

Gao, Bo Cai, Kathleen B. Heidebrecht, and Alexander F.H. Goetz. 1993. “Derivation of Scaled Surface Reflectances from AVIRIS Data.” *Remote Sensing of Environment* 44 (2–3): 165–78.

Gao, F., C. B. Schaaf, A. H. Strahler, Y. Jin, and X. Li. 2003. “Detecting Vegetation Structure Using a Kernel-Based BRDF Model.” *Remote Sensing of Environment* 86 (2): 198–205.

Hamlin, L., R. O. Green, P. Mouroulis, M. Eastwood, D. Wilson, M. Dudik, and C. Paine. 2011. “Imaging Spectrometer Science Measurements for Terrestrial Ecology: AVIRIS and New Developments.” *IEEE Aerospace Conference Proceedings*, 1–8.

Hirano, Akira, Marguerite Madden, and Roy Welch. 2003. “Hyperspectral Image Data for Mapping Wetland Vegetation.” *Wetlands* 23 (2): 436–48.

Hu, Baoxin, Wolfgang Lucht, and Alan H. Strahler. 1999. “The Interrelationship of Atmospheric Correction of Reflectances and Surface Brdf Retrieval: A Sensitivity Study.” *IEEE Transactions on Geoscience and Remote Sensing* 37 (2 I): 724–38.

Kennedy, R. E., W. B. Cohen, and G. Takao. 1997. “Empirical Methods to Compensate for a View-Angle-Dependent Brightness Gradient in AVIRIS Imagery.” *Remote Sensing of Environment* 291 (62):277–291.

Lewis, P., J. Gómez-Dans, T. Kaminski, J. Settle, T. Quaife, N. Gobron, J. Styles, and M. Berger. 2012. “An Earth Observation Land Data Assimilation System (EO-LDAS).” *Remote Sensing of Environment* 120: 219–35.

Li, Xiaowen, Feng Gao, Jindi Wang, and Alan Strahler. 2001. “A Priori Knowledge Accumulation and Its Application to Linear BRDF Model Inversion.” *Journal of Geophysical Research* 106 (Dll): 925–35.

Lin, Yuan, and Zhang Liquan. 2006. “Identification of the Spectral Characteristics of Submerged

Plant Vallisneria Spiralis." *Acta Ecologica Sinica* 26 (4): 1005–10.

Lucht, Wolfgang, Crystal Barker Schaaf, and Alan H. Strahler. 2000. "An Algorithm for the Retrieval of Albedo from Space Using Semiempirical BRDF Models." *IEEE Transactions on Geoscience and Remote Sensing* 38 (2 II): 977–98.

Nicodemus, F.E., J.C. Richmond, and J.J. Hsia. 1977. "Geometrical Considerations and Nomenclature for Reflectance." Vol. 160. National Bureau of Standards, US Department of Commerce, Washington, DC.

Olmanson, Leif G., Patrick L. Brezonik, and Marvin E. Bauer. 2013. "Airborne Hyperspectral Remote Sensing to Assess Spatial Distribution of Water Quality Characteristics in Large Rivers: The Mississippi River and Its Tributaries in Minnesota." *Remote Sensing of Environment* 130: 254–65.

Rashmi, S., Swapna Addamani, and S. Venkat. 2014. "Spectral Angle Mapper Algorithm for Remote Sensing Image Classification." *IJISET–International Journal of Innovative Science, Engineering & Technology* 1 (4): 201–5.

Schaepman-Strub, G., M. E. Schaepman, T. H. Painter, S. Dangel, and J. V. Martonchik. 2006. "Reflectance Quantities in Optical Remote Sensing-Definitions and Case Studies." *Remote Sensing of Environment* 103 (1): 27–42.

Schill, Steven, John Jensen, George Raber, and Dwayne Porter. 2004. "Temporal Modeling of Bidirectional Reflection Distribution Function (BRDF) in Coastal Vegetation." *GIScience & Remote Sensing* 41 (2): 116–35.

Sterckx, Sindy, Els Knaeps, Mark Bollen, Koen Trouw, and Rik Houthuys. 2007. "Retrieval of Suspended Sediment from Advanced Hyperspectral Sensor Data in the Scheldt Estuary at Different Stages in the Tidal Cycle." *Marine Geodesy* 30 (1–2): 97–108.

Thompson, David R., Bo Cai Gao, Robert O. Green, Dar A. Roberts, Philip E. Dennison, and Sarah R. Lundeen. 2015. “Atmospheric Correction for Global Mapping Spectroscopy: ATREM Advances for the HyspIRI Preparatory Campaign.” *Remote Sensing of Environment* 167: 64–77.

Thompson, David R., Robert O. Green, Didier Keymeulen, Sarah K. Lundeen, Yasha Mouradi, Daniel Cahn Nunes, Rebecca Castano, and Steve A. Chien. 2014. “Rapid Spectral Cloud Screening Onboard Aircraft and Spacecraft.” *IEEE Transactions on Geoscience and Remote Sensing* 52 (11): 6779–92.

Vaiphasa, Chaichoke, Suwit Ongsomwang, Tanasak Vaiphasa, and Andrew K. Skidmore. 2005. “Tropical Mangrove Species Discrimination Using Hyperspectral Data: A Laboratory Study.” *Estuarine, Coastal and Shelf Science* 65 (1–2): 371–79.

Vaiphasa, Chaichoke, Andrew K. Skidmore, Willem F. de Boer, and Tanasak Vaiphasa. 2007. “A Hyperspectral Band Selector for Plant Species Discrimination.” *ISPRS Journal of Photogrammetry and Remote Sensing* 62 (3): 225–35.

Wang, Le, and Wayne P. Sousa. 2009. “Distinguishing Mangrove Species with Laboratory Measurements of Hyperspectral Leaf Reflectance.” *International Journal of Remote Sensing* 30 (5): 1267–81.

Wanner, W., X. Li, and a. H. Strahler. 1995. “On the Derivation of Kernels for Kernel-Driven Models of Bidirectional Reflectance.” *Journal of Geophysical Research* 100 (D10): 21077.

Yang, Chenghai, James H. Everitt, Reginald S. Fletcher, Ryan R. Jensen, and Paul W. Mausel.

2009. “Evaluating AISA + Hyperspectral Imagery for Mapping Black Mangrove along the South Texas Gulf Coast.” *Photogrammetric Engineering & Remote Sensing* 75 (4): 425–35.

Zomer, Robert J., Antonio Trabucco, and Susan L. Ustin. 2008. “Building spectral libraries for wetlands land cover classification and hyperspectral remote sensing.” *Journal of Environmental Management* 90 (7):2170–2177.

# Chapter 2

## Improving the Transferability of Suspended Solid Estimation in Wetland and Deltaic Waters with an Empirical Hyperspectral Approach

### 2.1. Abstract

The deposition of suspended sediment is an important process that helps wetlands accrete surface material and maintain elevation in the face of sea level rise. Optical remote sensing is often employed to map total suspended solids (TSS), though algorithms typically have limited transferability in space and time due to variability in water constituent compositions, mixtures, and inherent optical properties. This study used *in situ* spectral reflectances and their first derivatives to compare empirical algorithms for estimating TSS using hyperspectral and multispectral data. These algorithms were applied to imagery collected by NASA's Airborne Visible/Infrared Imaging Spectrometer-Next Generation (AVIRIS-NG) over coastal Louisiana, USA, and validated with a multiyear *in situ* dataset. The best performing models were then applied to independent spectroscopic data collected in the Peace–Athabasca Delta, Canada, and the San Francisco Bay–Delta Estuary, USA, to assess their robustness and transferability. A derivative-based partial least squares regression (PLSR) model applied to simulated AVIRIS-NG data showed the most accurate TSS retrievals ($R^2$ = 0.83) in these contrasting deltaic environments. These results highlight the potential for a more broadly applicable generalized algorithm employing imaging spectroscopy for estimating suspended solids.

### 2.2. Introduction

Coastal wetlands provide many ecosystem services that are compromised when relative sea level rise (RSLR) rates, resulting from the combination of eustatic sea level rise and land

subsidence, exceed accretion rates (Morton et al. 2006). Wetland accretion in dynamic coastal settings is controlled by a combination of organic matter production and sediment capture, together producing accretion rates matching RSLR (Morris et al. 2002). While vegetation biomass and productivity contribute to accretion via organic matter accumulation, exogenic mineral suspended sediment is delivered to wetlands from external sources. Although subsidence rates in alluvial wetlands are often exacerbated by local groundwater withdrawal, hydrocarbon extraction, surficial sediment dewatering, and tectonic activity, they are most impacted by a reduced mineral sediment input (Burkett et al. 2003; Ericson et al. 2006).

Louisiana's coastal wetlands provide an example of how alterations in sediment supply can impact a marsh's ability to maintain surface elevation that can keep pace with RSLR. The extensive engineering of the Mississippi Deltaic Plain (MDP) has limited the Mississippi River's natural distributary network to the Atchafalaya River and Wax Lake Delta (Figure 2-1) and largely cut off the freshwater input and sediment delivery from the river to surrounding wetlands in the Terrebonne and Barataria basins (Twilley et al. 2016). This has resulted in subsidence rates of 13 ± 6 and 7 ± 3 mm/year in the lower Atchafalaya and Terrebonne basins respectively, which are exacerbated by global eustatic sea level rise of approximately 1–2 mm/year (Twilley et al. 2016; DeLaune et al. 2013). Increasing RSLR rates across the MDP alter the hydrology that regulates vegetation patterns, increasing saline intrusion and nutrient delivery along with flood duration and frequency (Krauss et al. 2009; Song et al. 2011). If local RSLR exceeds the rate of wetland surface elevation increase, plant communities will become submersed, drown, and convert to open water (Morris et al. 2002; Krauss et al. 2014). Measuring total suspended solids (TSS)—which describes the amount of organic and inorganic suspended particles in a water column (Glysson et al. 2000)—

provides critical information to assess causes of wetland dynamics, as changes in supply may help explain wetland submergence.

While *in situ* measurements may offer some insight into the spatial distribution of suspended sediment, the collection and processing of measurements over large areas is often infeasible, especially for investigating spatial variability through time (Curran and Novo 1988). A more comprehensive spatially explicit measurement of the suspended sediment concentrations in natural waterways and dredged channels could facilitate the quantitative assessment of the adjacent wetlands' stability and help explain the possible causes of degradation and loss. There is thus an urgent need to develop repeatable and transferable sediment retrieval methods that may be implemented in vulnerable regions such as the MDP. To develop and optimize such methods, it is necessary to assess different remote sensing instruments and approaches.

High spatial resolution optical remote sensing presents a valuable tool for retrieving information about the various optically active water constituents present in rivers and wetland channels, including chromophoric dissolved organic matter (CDOM), phytoplankton, and suspended sediment (Griffin et al. 2011; Olmanson et al. 2013; Fichot et al. 2016). The curvilinear relationship between red or near-infrared (NIR) reflectance and TSS has enabled the mapping of suspended sediment concentrations in surface waters using multispectral sensors (e.g. Moderate Resolution Imaging Spectroradiometer (MODIS), Sea-Viewing Wide Field-of-View Sensor (SeaWIFS), and Landsat) (Miller et al. 2004; Warrick et al. 2004; Ritchie and Cooper 2001). The availability of satellite-borne multispectral sensor data has led to a proliferation of methodologies for measuring water quality indicators such as turbidity or TSS in turbid and optically complex waters (Ritchie and Cooper 2001; Nechad et al. 2010; Doxaran et al. 2014; Dogliotti et al. 2015; Chen et al. 2015). Empirical approaches are commonly used to retrieve TSS concentrations—or

equivalently total suspended matter (TSM), suspended particulate matter (SPM), or suspended sediment concentration (SSC)—due to their simplicity in development and implementation, as well as for their explanatory power in a given system (Doxaran et al. 2002; Li et al. 2003; Ouillon et al. 2004; Han et al. 2006; Wang and Lu 2010; Pavelsky and Smith 2009; Volpe et al. 2011). However, most of these algorithms tend to have limited applicability across different optically complex water bodies and through time (Warrick et al. 2004; Chen et al. 2015). Two important factors limit the performance of such algorithms. First, variations in the composition and physico-chemical characteristics of the different optically active water constituents affect the relationship between the optical properties and the concentration of the constituents. Second, the mixtures of these constituents also vary. This is entailed in the relative concentrations of particulate inorganic matter (PIM) and particulate organic matter (POM), which together make up TSS. These effects govern a water body's inherent optical properties (IOPs), with IOP effects on remote-sensing reflectance being further dependent on instrument viewing geometry and illumination conditions (Curran and Novo 1988; Mobley et al. 2010). Additionally, water depth, or bottom reflectance, impacts observed reflectance independently from IOPs. For best performance, empirical algorithms typically need to be parameterized individually for a given optically complex water body (Lee et al. 2016; Dorji and Fearns 2016).

Imaging spectrometer data, which contain hundreds or thousands of contiguous spectral bands, can be potentially useful for estimating and mapping suspended sediment concentrations. To inform future sensor development and remote sensing campaigns, it is thus important to assess whether imaging spectrometers enable significant improvements in accuracy and retrieval capability compared to multispectral sensors. Imaging spectroscopy, which by definition is concerned with the interaction of electromagnetic radiation with matter, is commonly referred to

as hyperspectral remote sensing. In addition to standard empirical approaches, imaging spectrometers enable methods that make use of additional spectral data. For example, contiguous spectral reflectance measurements facilitate the calculation of derivative spectra, which highlight spectral shape and can be used to identify absorption features, as well as reduce illumination variability across images (Tsai and Philpot 1998; Louchard et al. 2002). Field or laboratory-based spectrometers may also complement imaging spectrometer data by providing more accurate, targeted sample data for deriving relationships that can be scaled to imagery (Lee et al. 2016; Forget et al. 2001; Knaeps et al. 2015; Kromkamp et al. 2006; Sterckx et al. 2007), identifying spectral characteristics and absorption features within target spectra (Louchard et al. 2002; Choe et al. 2008; Martínez-Carreras et al. 2010), and developing generalized models (Forget et al. 2001; Chen et al. 1992). Such methodologies have been applied to suspended sediment mapping with data from Hyperion (Brando and Dekker 2003), an imaging spectrometer onboard the EO-1 satellite, and numerous airborne sensors (Olmanson et al. 2013; Senay et al. 2001; Palacios et al. 2015). These imaging spectroscopy approaches should allow for developing optimized empirical algorithms for constituent retrieval that account for changes in water properties. Here, we test this hypothesis by applying such empirical methods to airborne imaging spectrometer data in order to estimate TSS in complex wetland environments without site-specific calibration.

This study's first objective is to determine whether imaging spectrometer data provides a significant improvement over multispectral data and established generalized approaches for estimating TSS across a range of deltaic and estuarine settings (Figure 2-1). We then use these results to develop a TSS retrieval algorithm to map suspended solid concentrations in coastal Louisiana with a multiyear airborne imaging spectrometer dataset. The resultant sediment data products will contribute to assessments of the region's sediment budget and the health of the

surrounding coastal wetlands. Further, assessment of the model's robustness and transferability will inform the development of a more accurate and broadly applicable TSS retrieval algorithm.

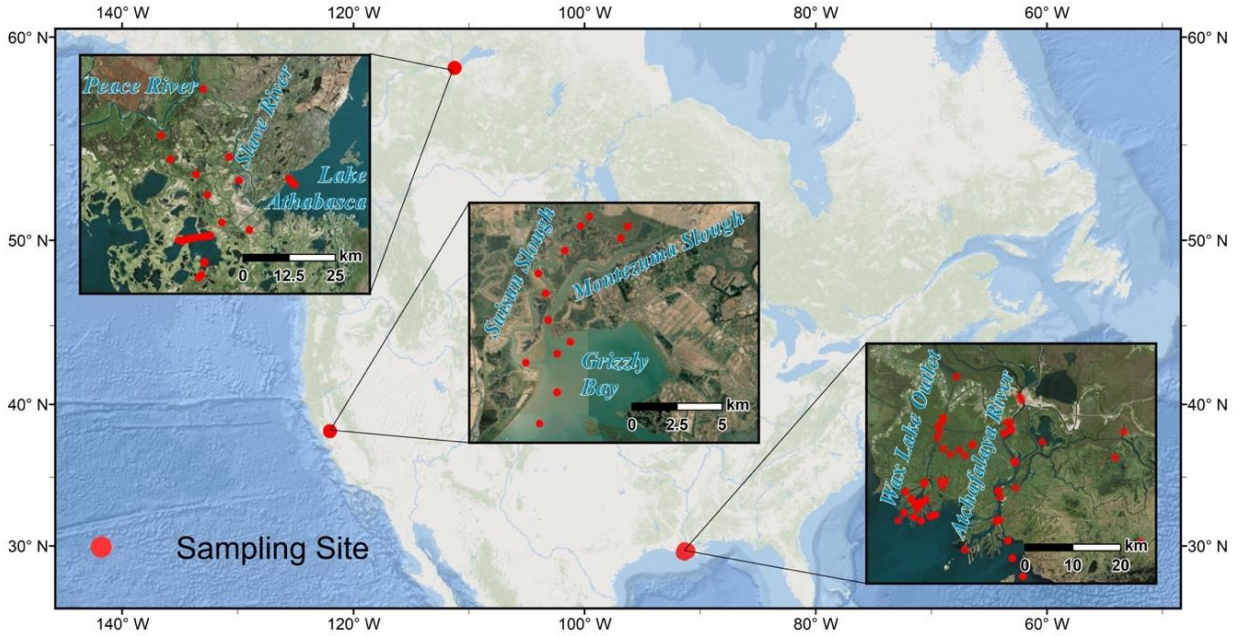


**Figure 2-1.** Study areas corresponding to water sample and spectroscopic measurement locations: Canada's Peace–Athabasca Delta (top-left), Grizzly Bay in California's San Francisco Bay–Delta Estuary (middle), and the Louisiana's Wax Lake Delta and Atchafalaya River—this study's primary study area (bottom-right).

## 2.3. Materials and Methods

This study used paired *in situ* TSS samples and reflectance spectra (n = 35) collected simultaneously in the Atchafalaya River, Wax Lake outlet, and surrounding water bodies to develop and validate models relating spectral signatures to TSS. These models were applied to multiyear airborne imaging spectrometer and simulated MODIS data to obtain spatially explicit TSS maps validated with independent *in situ* measurements (2015 n = 17, 2016 n = 22). The robustness of our TSS retrieval model approaches across diverse deltaic and estuarine

environments was assessed with independent datasets collected in the Peace–Athabasca Delta (n = 40) and the San Francisco Bay–Delta Estuary (n = 13).

### *2.3.1. Airborne Imaging Spectrometer Data Acquisition with AVIRIS-NG*

The Airborne Visible–Infrared Imaging Spectrometer-Next Generation (AVIRIS-NG) measures 14-bit radiance from 380 to 2510 nm wavelengths with a ~5-nm spectral resolution (Hamlin et al. 2011; Thompson et al. 2015). The primary data used in this study consists of one mosaic of flightlines from 2015 and two from 2016. The 2015 mosaic is a composite of 40 flightlines collected over Louisiana's coastal wetlands from May 9 to June 6 and contains 432 bands at a 3.8-m spatial resolution. The 2016 data were each collected continuously on October 17 and 18, with 11 and 13 flightlines respectively, and contain 425 bands at a 5.4-m spatial resolution. Each raw dataset was atmospherically corrected using the physics-based ATmospheric REMoval (ATREM) algorithm to derive a surface reflectance image (Thompson et al. 2015; Gao et al. 1993; Bue et al. 2015), with water pixels that approximate exact normalized water-leaving reflectance ($\rho_w$) (Morel and Gentili 1996). Remote-sensing reflectance ($R_{rs}$) corresponds to the water-leaving radiance through a solid angle normalized to the above-surface downwelling irradiance and is the measure of reflectance most commonly used for remote sensing of water bodies (Mobley et al. 2010). Assuming isotropic reflectance across the water surface, $R_{rs}$ was derived from $\rho_w$ by dividing the measured reflectance by $\pi$ in accordance with the NASA Ocean Biology Processing Group's standards for sensors such as MODIS and VIIRS (Mobley et al. 2010).

### *2.3.2. Field Measurements for Algorithm Development*

#### *2.3.2.1. Total Suspended Solids Measurements*

Total suspended solids were measured from *in situ* water samples collected throughout the Atchafalaya River, Wax Lake outlet, and surrounding waterways. We collected 35 samples in October 2016 and 17 samples in June 2015. The various sampling sites were chosen to cover a variety of apparent sediment concentrations and water types along the river-coastal ocean continuum (Figure 2-1). Water samples were collected just below the water surface and approximately in the middle of their given channels. Samples were stored on ice and transported to a laboratory, where they were filtered through pre-weighed, pre-combusted 0.7-µm glass-fiber filters (GF/F). After being rinsed of salts, filters were dried at 110°C until a constant weight was attained in order to derive volumetric TSS measurements accurate to hundredths mg/L following the ESS Method 340.2 protocol (Environmental Protection Agency 1993).

#### *2.3.2.2. In Situ Spectral Reflectance Measurements*

At each water sample location, reflectance spectra were collected using an Analytical Spectral Devices, Inc. (ASD), FieldSpec® 3 spectrometer (Analytik Ltd, Cambridge, United Kingdom). To control for the variable atmospheric moisture content and cloud activity in this coastal region, data were collected in Digital Number (DN) format and by alternating between the white reference calibration panel and the target water surface at nadir and away from the boat hull. Ten alternating pairs of measurements were captured at nadir for each target site, in accordance with established protocols (Doxaran et al. 2002; Gómez 2014). Each set of *in situ* spectra was then processed to compile a table of reflectance data with which to model TSS.

The ratio of above-water radiance over that of white-reference radiance was divided by $\pi$ and by the albedo of the white reference panel (~99%) to derive estimates of water-leaving

radiance—though uncorrected for the influence of skylight reflectance—divided by the downwelling irradiance at the surface (Östlund et al. 2001). The spectrometer data was truncated to the visible–near-infrared (VNIR) domain, ranging from 400–1000 nm to excise shortwave infrared (SWIR) bands where water attenuates radiation. Each spectrum was inspected for irregularities, e.g., erroneous steps in the spectrum, contamination by floating matter, or abnormal brightness caused by sun glint, with a small number (less than 5% of individual samples) being discarded. These selected spectra were then averaged together for each sample site, calculating a single reflectance spectrum with 1-nm spectral resolution paired with each water sample's TSS value.

#### *2.3.2.3. Simulation of AVIRIS-NG and MODIS Remote Sensing Reflectance*

Spectra were convolved to match AVIRIS-NG's 5-nm sampling by using a Gaussian function defined by each AVIRIS-NG band's Full Width at Half-Maximum (FWHM) reported in the flightline header file. Each 1-nm reflectance value from the *in situ* spectra that fell within the corresponding 5-nm AVIRIS-NG band was input into the function and the output values were normalized by dividing outputs by the sum of their absolute values. The normalized output and observed reflectance matrices were multiplied to return each simulated AVIRIS-NG band response. A correction was then applied to the "uncorrected" spectra to account for the reflectance of skylight at the air-water interface and derive $R_{rs}$. Percent cloud cover was estimated based on observation at each sample site, while solar zenith angle was calculated for each location using its associated GPS point and time. Wind speed, atmospheric pressure, and air temperature measured for each time and location were obtained from the nearest local meteorological station in Morgan City, Louisiana (Station ID: KLAMORGA15, N 29°41'23'', W 91°11'42'', data accessed at

https://www.timeanddate.com/weather/@4333811). These parameters were used as inputs for Hydrolight® simulations of the ratios of skylight surface reflected (upwelling) radiance at nadir normalized to the downwelling irradiance. Estimates of skylight surface reflectance were then subtracted from the uncorrected spectra to make the correction. A final correction was made from these spectra by subtracting the reflectance value measured at 1000 nm from each spectrum, under the assumption that water-leaving radiance at 1000 nm are null and that any residual measured reflectance is caused by uncorrected sunglint. This is similar to the correction based on 750-nm reflectance performed by Gómez (2014), though 1000 nm was selected in order to include the spectral feature around 800 nm in further analysis (Chen et al. 1992). For range of TSS values employed here (8.98–74.39 mg/L), $R_{rs}$ is negligible at 1000 nm (Doxaran et al. 2002). The same bias correction was also calculated and applied for the AVIRIS-NG $R_{rs}$ data to reduce glint impacts and ensure compatibility with *in situ* data. The agreement between the *in situ* and corresponding AVIRIS-NG pixel surface reflectance measurements are shown in Figure 2-A1, showing the spectral angles calculated from each corrected $R_{rs}$ sample pairing.

To further assess the utility of imaging spectrometer data against multispectral data, MODIS bands were simulated from all *in situ* and image spectra. This was accomplished for MODIS bands 1 and 2, as well as the suite of ocean color bands (8 through 16), by applying MODIS's relative spectral response (RSR) function for each band ($B_i$) to the ASD FieldSpec® 3 data with Equation 1 (Chen et al. 2015):

$$R_{rs}(B_i) = \frac{\sum_{\lambda 1}^{\lambda n} S(\lambda) R_{rs}(\lambda)}{\sum_{\lambda 1}^{\lambda n} S(\lambda)} \quad (1)$$

$\lambda_1$ and $\lambda_n$ respectively represent the lower and upper limit wavelength of each MODIS band *i*. *S(λ)* is the band's spectral response function value at each wavelength, while $R_{rs}(\lambda)$ is the measured reflectance at each wavelength.

### *2.3.3. Total Suspended Solids Algorithm Development from Simulated Sensor Data*

Typical empirical methods make use of Ordinary Least Squares Regression (OLSR) by incorporating one or more bands as the independent variables in order to estimate the dependent variable—i.e., TSS or its equivalent. However, OLSR must meet several conditions for statistical validity. Each independent variable must have a sufficient sample size, be statistically independent (i.e., not significantly collinear), and have a well-understood relationship with the dependent variable (Tobias 1995; Carrascal et al. 2009). While these assumptions are generally met by regression analyses using multispectral data, provided utilized bands are separable and independent, OLSR is not applicable to imaging spectrometer data unless a small sample of independent bands are selected from the image cube. Partial Least Squares Regression (PLSR) instead offers an ideal tool for developing regression models for ecological studies employing imaging spectroscopy (Carrascal et al. 2009), as it can make use of the high number of adjacent narrow bands approximating a surface's full reflectance spectrum. The high volume of contiguous bands offers additional spectral information, though their adjacency violates OLSR's assumption of independence. PLSR applies a transformation to multidimensional data onto the selected number of synthetic components. Unlike Principal Components Analysis, this transformation is dependent on the relationship between the dependent and independent variables. The component scores are then used to weight and calculate the model coefficients for each independent variable. PLSR is a valuable tool for imaging spectroscopy applications as it emphasizes predictive

capability rather than determining variable relationships and deemphasizes the need for a large sample size, which is often difficult to develop in ecological research (Martínez-Carreras et al. 2010; Tobias 1995; Carrascal et al. 2009). Further, by employing spectral slope in place of reflectance, derivative spectroscopy is highly effective for developing such models (Tsai and Philpot 1998; Louchard et al. 2002).

The October 2016 *in situ* TSS and *in situ* spectral $R_{rs}$ data from Louisiana were used to develop a set of PLSR models and determine the optimal parameters for a TSS algorithm. In addition to $R_{rs}$, we calculated the first derivatives of these spectra, thereby providing the spectral slope at each band (Figure 2-2). For the simulated AVIRIS-NG data—derived from the *in situ* ASD FieldSpec® 3 spectra—both the reflectance and derivative datasets were used in PLSR models. Reflectance and slope values thus represented the explanatory variables while the corresponding TSS value represented the dependent variable. The resultant model parameters were then used to calculate each band's (*i*) associated Variable Importance in Projection (VIP) values with Equation 2 (Mehmood et al. 2012):

$$VIP_i = \sqrt{p \sum_{a=1}^{A} [(q_a^2 \, t'_a t_a)(w_{ai}/\|w_a\|)^2] / \sum_{a=1}^{A} (q_a^2 t'_a t_a)} \qquad (2)$$

where $w_a$ is the loading weights defining the direction in the space spanned by the explanatory variables and $t_a$ is the score vector (the loading weights multiplied by the explanatory variables). $p$ is the X-loading, computed by regressing the explanatory variables on the score vector, and $q_a$ is component $a$'s Y-loading, computed the same way but with the dependent variable. The loading $(w_{ai}/\|w_a\|)^2$ represents the importance of variable $i$ and explains the variance in each PLS component $(q_a^2 t'_a t_a)$ (Mehmood et al. 2012). The components are the new predictor

variables calculated from linear combinations of the original predictor variables. Hence the $VIP_i$ weights measure the contribution of each variable according to that variance. A VIP value greater than one typically indicates a variable that is beneficial to the model's predictive power (Mehmood et al. 2012; Farrés et al. 2015). With spectroscopic data, applying a VIP filter may identify the specific absorption features and spectral characteristics that are most associated with the dependent variable (Farrés et al. 2015). By limiting model inputs to only those bands with a strong weighting, spectral domains that bear little association and thus introduce noise into the model may be excised. Models were thus redeveloped based on a reduced set of bands where VIP < 1 (Figure 2-2).

For models based on field spectrometer data convolved to AVIRIS-NG spectral resolutions, further testing was required to finalize the models by determining the optimal number of PLSR components. The 1-, 2-, 3-, 4-, and 5-component models were developed with this process, based on derivatives, and applied to all spectral datasets. The 1-component model produced a low model $R^2$, while the 5-component model produced high validation Root Mean Square Errors (RMSE) as a result of overfitting, indicating each model's invalidity. The 2-, 3-, and 4-component models each produced similarly high model $R^2$ values and low RMSE values from validation points, with no single model producing superior results across all validation datasets. As these model performances were not significantly different, succeeding models were developed with 2 components to minimize the risk of overfitting and attain greater transferability through simplified parametrization. Both the reflectance and derivative-based AVIRIS-NG model coefficients are reported in Table 2-A1. We evaluated the overall quality of the PLSR fits by calculating $R^2$, RMSE, and Mean Relative Error (MRE).

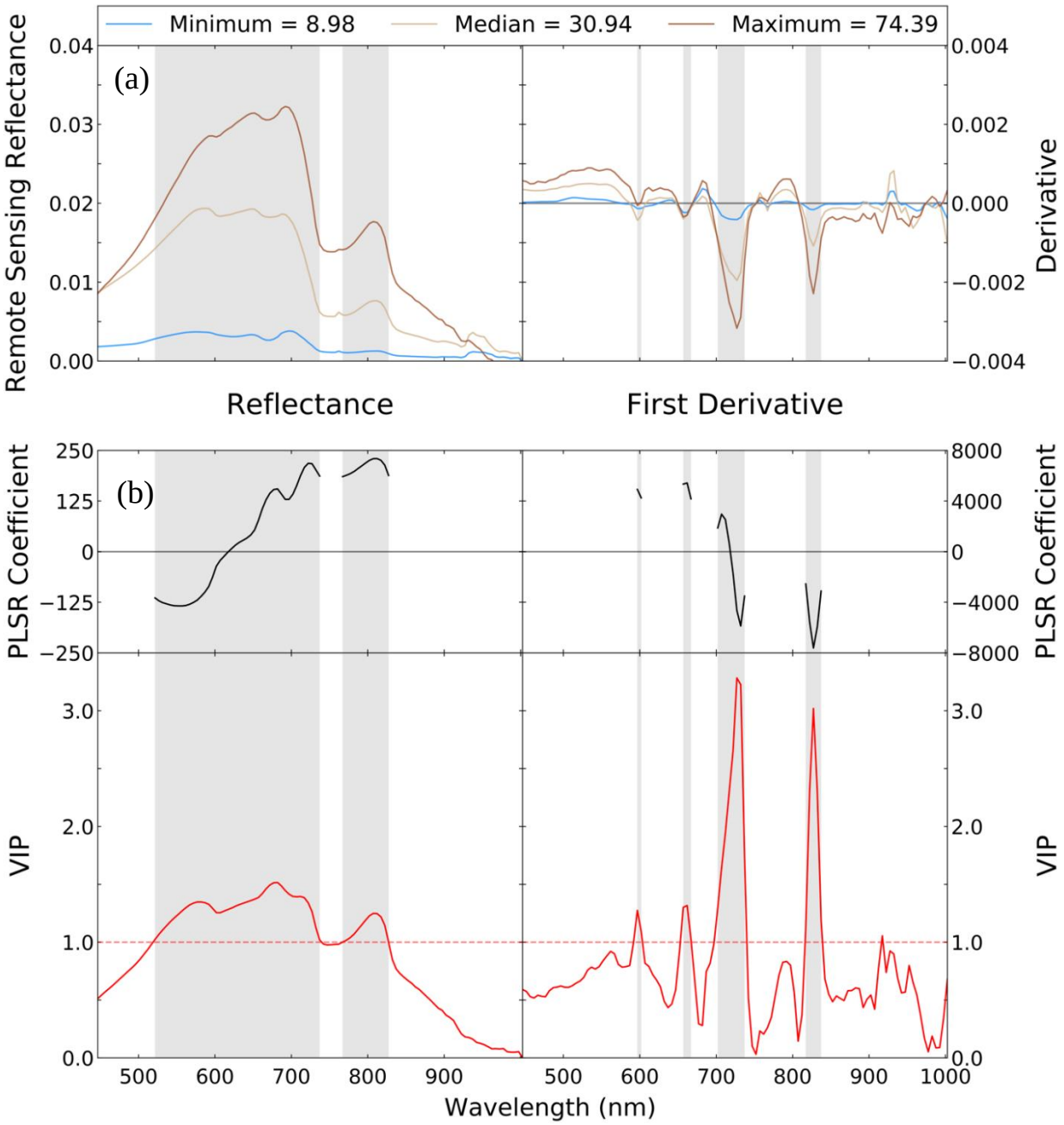


**Figure 2-2**. Partial least squares regression (PLSR) analysis. (a) Sample spectra plots for the 2016 Louisiana field spectrometer reflectance measurements (left), representing the paired spectra for the sample set's minimum (8.98 mg/L), median (30.94 mg/L), and maximum (74.39 mg/L) TSS measurements, and the corresponding first derivatives (right). (b) PLSR model summaries for simulated Airborne Visible–Infrared Imaging Spectrometer-Next Generation (AVIRIS-NG) reflectance and first derivative. The red lines indicate the Variable Importance in Projection (VIP) value at each band (bottom) for the initial PLSR model, and the black lines (top) indicate the models' coefficient value for each utilized band (also reported in Table 2-A1). Shaded regions indicate the utilized wavelengths in the final PLSR models, where the associated VIP > 1.

Many remote sensing studies have shown that imaging and ground-based spectrometers can be employed to construct empirical relationships using particular spectral domains, but such analyses are not directly applicable to spaceborne multispectral datasets (Pavelsky and Smith 2009). Standard multispectral data are likely preferable if such relationships offer only marginal improvements due to methodological simplicity and the ubiquity of multispectral sensors relative to imaging spectrometers. The AVIRIS-NG-based models were compared to the performance of the MODIS-based models to provide an assessment of imaging spectroscopy's efficacy compared to standard multispectral datasets and approaches. Each AVIRIS-NG band within a MODIS band's range had the corresponding RSR function value applied as per Equation 1 to create imagery simulating MODIS's spectral response without degrading the spatial resolution. The above PLSR modelling process was first repeated with the simulated MODIS ocean color bands (band 8–16) (Table 2-1), resulting in Equation 3:

$$TSS = -1440.73\rho_{11} - 1546.45\rho_{12} + 1467.11\rho_{13} + 1830.09\rho_{14} + 2273.30\rho_{15} + 12.64 \quad (3)$$

where $\rho_{11}$-$\rho_{15}$ correspond to the reflectance values for MODIS bands 11–15. Further, simulations of MODIS bands 1 (red, 620–670 nm) and 2 (NIR, 841–876 nm) were applied in univariate linear OLSR models to derive equations 4 and 5, respectively:

$$TSS = 2071.07\rho_1 - 2.64 \quad (4)$$

$$TSS = 9077.91\rho_2 + 6.97 \quad (5)$$

These models mirror the models developed by Chen et al. (2015) with MODIS Terra and Aqua L2 Surface Reflectance (MOD09 and MYD09, respectively) imagery. The three models described here were developed with simulated MODIS reflectance values, applying the convolution

described above to the ASD FieldSpec® 3 reflectance data collected in Louisiana in October 2016. Results were validated from the TSS product generated from AVIRIS-NG bands convolved to MODIS spectral resolution.

**Table 2-1.** Simulated MODIS Partial Least Squares Regression Model*

| MODIS Band | Wavelength (nm) | VIP | Coefficient |
|---|---|---|---|
| 8 | 405–420 | 0.35 | |
| 9 | 438–448 | 0.48 | |
| 10 | 483–493 | 0.75 | |
| 11 | 526–536 | 1.05 | −1440.73 |
| 12 | 546–556 | 1.17 | −1546.45 |
| 13 | 662–672 | 1.40 | 1467.11 |
| 14 | 673–683 | 1.48 | 1830.09 |
| 15 | 743–753 | 1.04 | 2273.30 |
| 16 | 862–877 | 0.63 | |
| Constant | | | 12.64 |

*Model in equation format shown in Equation 3

Additionally, we applied the generalized model developed by Nechad et al. (2010) to assess the various model performances against a widely used and validated algorithm applicable to multiple sensors. We used the published model coefficients for 712.5 nm, as the hyperspectrally tabulated model performance peaks at this wavelength ($R^2$ = 82.9). TSS was retrieved with the following equation:

$$TSS = \frac{A^{\rho}\pi R_{rs}}{1 - \pi R_{rs}/C^{\rho}} + B^{\rho} \quad (6)$$

where $A^{\rho}$, $B^{\rho}$, and $C^{\rho}$ are coefficients for 712.5 nm listed by Nechad et al. (2010), being 606.12, 1.19, and 18.98 respectively, and $R_{rs}$ is the remote sensing reflectance at 712.5 nm.

Each of the six models (Table 2-2) derived from *in situ* TSS and $R_{rs}$ measurements was then applied to the three AVIRIS-NG $R_{rs}$ mosaics. To generate a water mask from the original AVIRIS-NG surface reflectance imagery, clouds and artificial surfaces were first removed. Minimum threshold values in the 446.5 nm band, the 2234.6 nm band, and a normalized blue (486.5 nm)/green (566.7 nm) ratio (0.06, 0.1, and -0.15, respectively) were found to satisfactorily identify cloud and artificial surface pixels together based on visual inspection. The identified pixels were then dilated to better encompass clouded areas. A two-cluster k-means classification algorithm, based on bands corresponding to 446.5, 486.5, 566.7, 661.8, 862.2, 1568.4, and 2234.6 nm in addition to normalized difference vegetation index (NDVI) and normalized difference water index (NDWI), accurately divided the remaining pixels into land—including submerged and floating vegetation—and water (Jensen et al. 2017). MODIS-based models were then applied to the relevant simulated bands, as per Equation 1, that replicate MODIS spectral responses at the AVIRIS-NG data's spatial resolution. The reflectance-based PLSR model was simply subset to the band selection highlighted in Figure 2-2 for the application of the model coefficients. It should be noted that reflectance-based models are typically very sensitive to $R_{rs}$ absolute values, and that retrieval errors may be compounded by radiometric errors. For AVIRIS-NG, the instrument is prone to aircraft wobble-induced variations in observed reflectance. This is the case for the *in situ* pixel reflectance sample pairs shown in Figure 2-A1 that show abnormally high spectral angles, as the points coincide with a strand of glint that causes abnormally high reflectance in the NIR. However, the shapes of key spectral features retain better matches across the samples. This provides further motivation for applying a derivative-based model, as the first derivative of reflectance is less prone to radiometric errors, bidirectional reflectance distribution function effects, and overall illumination variations. For the derivative-based PLSR model, the first

derivative of each water pixel spectrum was calculated through the VNIR domain, and the resultant array was subset to the selected derivative bands with a VIP greater than 1 (Figure 2-2). Each model was correspondingly applied to its band subset, with the resulting values being broadcast into mask's water pixels while other classes were set to null. A $3 \times 3$ median filter was applied to the TSS arrays to smooth data and diminish the effects of illumination variations, producing the final TSS maps (Figure 2-7) from the 2015 and 2016 mosaics.

### *2.3.4. Validation*

#### *2.3.4.1. Assessing Model Temporal Transferability: Validation with AVIRIS-NG in Coastal Louisiana*

**Table 2-2.** Total suspended solids (TSS) model performances in the Louisiana study site

| | **MODIS Band 1** | **MODIS Band 2** | **Generic (712.5 nm; Nechad et al. 2010)** | **MODIS PLSR** | **AVIRIS-NG Reflectance PLSR** | **AVIRIS-NG Derivative PLSR** |
|---|---|---|---|---|---|---|
| Model $R^2$ | 0.53 | 0.80 | - | 0.82 | 0.82 | 0.83 |
| 2015 MRE (%) | 25.51 | 189.00 | 24.28 | 43.83 | 51.01 | 28.88 |
| 2016 MRE (%) | 23.51 | 18.24 | 17.92 | 13.75 | 13.06 | 14.87 |
| 2015 RMSE (mg/L) | 12.53 | 39.91 | 11.08 | 24.46 | 29.18 | 12.69 |
| 2016 RMSE (mg/L) | 9.78 | 6.42 | 7.38 | 6.29 | 5.88 | 6.34 |

*Mean Relative Error (MRE) and Root Mean Square Errors (RMSE) values are derived from validation datasets (2015 n = 17, 2016 n = 22). Training n = 35.

Our TSS maps were independently validated with the Louisiana field data collected in 2015, in addition to those points collected in 2016 (Table 2-2). Of the original 35 *in situ* TSS and $R_{rs}$ pairs used to parameterize the model, 22 samples coincided spatially and temporally (within 1.5 h of the flight windows) with AVIRIS-NG flightlines and were used for initial validation of the TSS maps. It should be noted that these 2016 *in situ* field spectrometer samples were included in the model parameterization, though their coincident AVIRIS-NG pixel spectra were analyzed for validation. The 17 samples from 2015 thus provided independent validation and allowed assessment of each model's temporal transferability (i.e., the same site but different time period). The average TSS value in a $3 \times 3$ pixel window surrounding each sample point—selected for generalization and to minimize spatial errors that may exist between GPS points and image georeferencing—was extracted and compared to the *in situ* TSS measurements. These values were used to create validation scatterplots and calculate RMSE and MRE values for each model and year.

#### *2.3.4.2. Assessing Model Spatial Transferability: Applications in Grizzly Bay and the Peace–Athabasca Delta*

We collected independent validation data to test our TSS algorithms. These included Portable Remote Imaging Spectrometer (PRISM) $R_{rs}$ data collected over the Grizzly Bay region of the San Francisco Bay–Delta Estuary (Figure 2-1) on April 28, 2014 (Fichot et al. 2016). NASA's airborne PRISM instrument here attained data from 350–1050 nm at a 2.6-m spatial resolution (Fichot et al. 2016), and again employed ATREM (Thompson et al. 2015) to derive $R_{rs}$ from raw radiance. Given PRISM's 2.83 nm spectral sampling, compared to AVIRIS-NG's 5 nm, each pixel's reflectance spectrum was interpolated to calculate the specific reflectance value corresponding to each AVIRIS-NG band center. ASD FieldSpec® 3 data collected in Canada's

Peace–Athabasca Delta (Long and Pavelsky 2012; Long and Pavelsky 2013) in June and July, 2011, provided further validation data. The 1-nm resolution field spectra from this dataset were processed to simulate AVIRIS-NG and MODIS band responses, following the methods used on the Louisiana field spectrometer data. A total of 13 coincident TSS samples accompanied the PRISM data, and 176 were collected in the Peace–Athabasca Delta with the *in situ* reflectance measurements.

These independent validation data were leveraged to assess the derivative-based PLSR model's transferability in space (Table 2-3). The model was implemented on the Grizzly Bay PRISM data (Fichot et al. 2016) after resampling to match AVIRIS-NG's spectral resolution. The first derivatives of the interpolated image spectra were calculated, and the PLSR model coefficients and constant developed with the Louisiana field spectrometer data were directly applied to the data to retrieve TSS values. The resultant TSS map had the median filter applied and coincident TSS sample points (ranging from 23.03–67.29 mg/L) were used for value extraction and validation. The Peace–Athabasca field spectrometer dataset (Long and Pavelsky 2012; Long and Pavelsky 2013), then, encompasses a wide range of TSS values in its 176 samples (Table 2-3), with a maximum of over 3600 mg/L—well beyond the range of the training dataset collected in Louisiana. The PLSR model was again applied to this tabular dataset's reflectance derivatives. The totality of the datasets analyzed here provides validation for the algorithm itself, rather than individual maps.

## 2.4. Results

### *2.4.1. Simulated MODIS and Generalized Model Assessment*

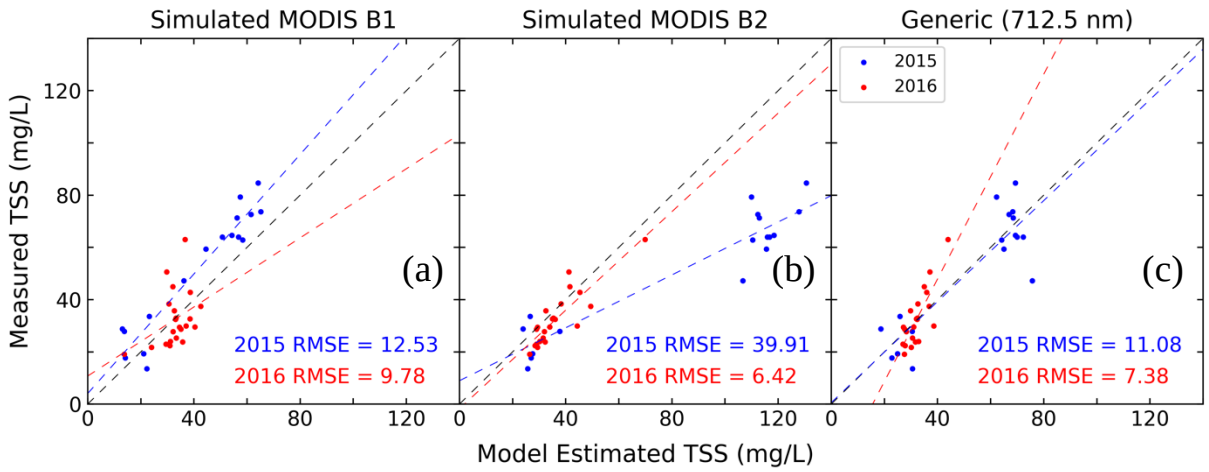


**Figure 2-3.** Univariate model validation scatterplots. Produced for the simulated MODIS ordinary least squares (OLSR) and generalized (712.5 nm) (Nechad et al. 2010) models based on the 2015 and 2016 Atchafalaya and Wax Lake Delta datasets. The (a) Band 1 and (b) Band 2 models mirror those developed by Chen et al. (2015) but are parameterized with the 2016 Louisiana $R_{rs}$ data to investigate the performance of established multispectral methods relative to imaging spectroscopy models. The generic model (c) utilizes the hyperspectrally tabulated model coefficients published by Nechad et al. (2010) and $R_{rs}$ for 712.5 nm.

The two model approaches that utilize MODIS bands 1 and 2, as outlined by Chen et al. (2015), and the PLSR models developed here are summarized in Table 2-3. Validation of the 2015 Louisiana data indicated that the linear regression model produced with the simulated MODIS band 1 (Table 2-2) produced the lowest RMSE and MRE at 12.53 mg/L and 25.51%, respectively. Of the two MODIS-based OLSR models, only the band 1 linear regression model, leveraging red broadband reflectance that is typically most sensitive to sediment loads (Pavelsky and Smith 2009), produced low error for both 2015 and 2016 (Figure 2-3). The band 2 model exhibits a high degree of clustering between low and high TSS values, with high overestimation error for water samples with high sediment loads. The 1:1 line (Figure 2-3; Figure 2-4) represents a perfect estimation, where model estimation equals the validation sample. A tight grouping of points and higher correlation value relative to the 1:1 line thus indicates a higher quality model. The linear regression models based on bands 1 and 2 each produced reasonable error metrics for 2016, the

year in which the data was collected, but only the band 1 model indicates suitable temporal transferability to the 2015 data (Figure 2-3).

Additionally, The MODIS PLSR model exhibits many of the same characteristics as the band 2 model. The model based on the simulated MODIS ocean color band suite is subject to similar clustering of low and high TSS values while also entailing a significant bias that results in a systematic overestimation at higher TSS concentrations (Figure 2-4).

### *2.4.2. AVIRIS-NG Assessment*

**Table 2-3**. Validation data and results for the derivative-based PLSR algorithm.

| | **Atchafalaya and Wax Lake Deltas (2015)** | **Atchafalaya and Wax Lake Deltas (2016)** | **San Francisco Bay–Delta Estuary (Fichot et al. 2016)** | **Peace–Athabasca Delta* (Long and Pavelsky 2012; Long and Pavelsky 2013)** |
|---|---|---|---|---|
| Instrument | AVIRIS-NG | AVIRIS-NG | PRISM | ASD FieldSpec® 3 |
| Dates | May 7–June 12, 2015 | October 17–18, 2016 | April 28, 2014 | June 24–July 6, 2011 |
| *n* | 17 | 22 | 13 | 40 |
| TSS Sample Range (mg/L) | 13.53–84.67 | 19.11–62.99 | 23.03–67.29 | 3.93–109.64 |
| Chlorophyll-a Sample Range (µg/L) | - | - | 1.67–6.63 | 3.87–14.89 |
| CDOM Sample Range | - | - | 23.61–56.26 ($a$(350) ($m^{-1}$)) | 136.76–566.03 (ppb) |
| RMSE (mg/L) | 12.69 | 6.34 | 7.80 | 15.95 |
| MRE (%) | 28.88 | 14.87 | 13.24 | 76.56 |
| Validation $R^2$ | 0.69 | 0.62 | 0.76 | 0.80 |

*TSS samples were limited to ≤109.64 mg/L, the sample value at which validation results begin to degrade. chromophoric dissolved organic matter (CDOM) was derived from an *in situ* fluorometer (Eureka Manta Multiprobe) and is reported here in units ppb of a standard.

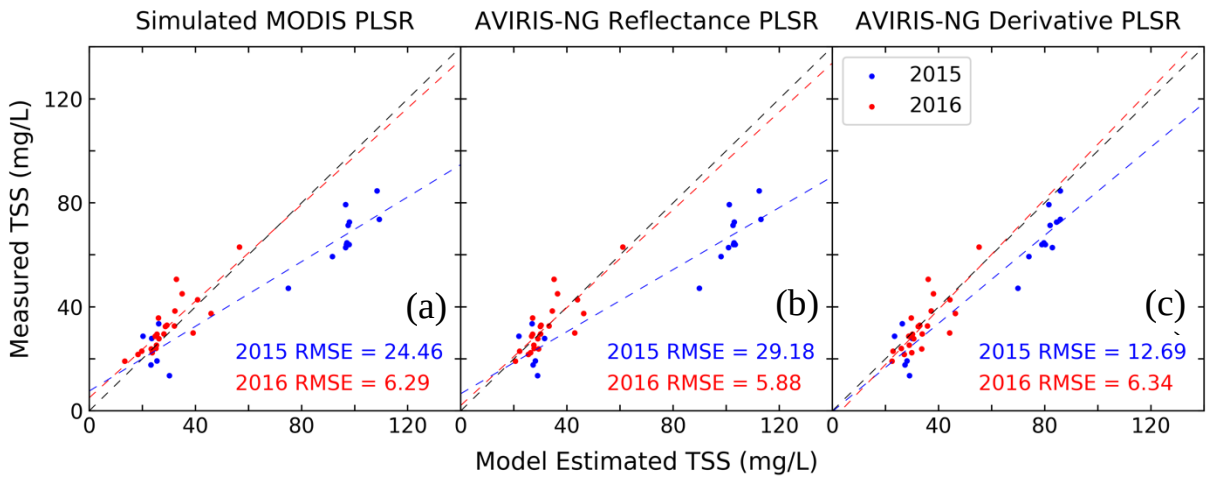


**Figure 2-4**. Partial least squares regression (PLSR) model validation scatterplots. Produced for the PLSR models applied to the 2015 and 2016 coastal Louisiana datasets: (a) simulated MODIS ocean color band reflectance, (b) AVIRIS-NG reflectance, and (c) AVIRIS-NG derivative.

For the AVIRIS-NG data, the first derivative-based PLSR model produced the highest model $R^2$ value at 0.83 (Table 2-2), based on the *in situ* training data. The RMSE for the 2016 set of sample points, calculated with the extracted TSS map values for validation, indicates the lowest error produced at 6.34 mg/L. This derivative-based model outperformed the PLSR model applied to AVIRIS-NG reflectance, which produced results similar to those of the MODIS PLSR model. As the derivative-based PLSR and the MODIS band 1 models exhibited low error for both years in Louisiana, each was examined in other study sites for transferability.

### *2.4.3. Independent Imaging Spectroscopy Validation*

To assess transferability, we selected three high performance models—the MODIS band 1 model, the generalized 712.5 nm model (Nechad et al. 2010), and the AVIRIS-NG PLSR derivative model—and conducted additional independent validation data from other wetlands. The first dataset consisted of PRISM flightlines collected over the San Francisco Bay–Delta Estuary's

Grizzly Bay and coincident *in situ* TSS measurements (Fichot et al. 2016). The MODIS band 1 and the derivative-based PLSR models were applied to the PRISM remote sensing reflectance data using the model coefficients derived from the Louisiana data. Validation of the resultant TSS maps revealed RMSEs of 13.81 and 7.80 mg/L for the MODIS band 1 and derivative-based PLSR TSS retrievals, respectively (Table 2-3), with corresponding MREs of 33.64 and 13.24%. The distribution of measured versus model-estimated TSS points relative to the 1:1 line (Figure 2-5), however, indicates a significant difference in model performances. The MODIS band 1 model shows little variance in the predicted values, with most points clustered at 40-50 mg/L, displaying significant biases at lower and higher concentrations. The results show a similar pattern in the generalized model application. The derivative-based PLSR model, conversely, shows a tight grouping of points close to the 1:1 line, with a slight underestimation bias, such that the model estimated TSS values are highly correlated with the corresponding true values.

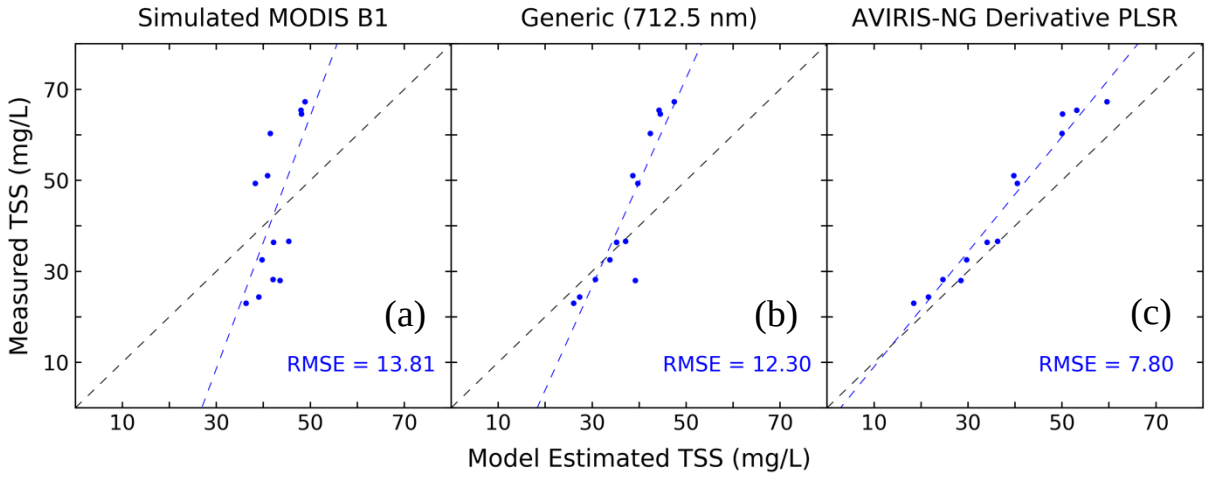


**Figure 2-5.** San Francisco Bay-Delta Estuary validation results. Produced from the total suspended solids (TSS, mg/L) retrieval using the PRISM dataset with the (a) simulated MODIS band 1 regression model, (b) generalized model at 712.5 nm (Nechad et al. 2010), and (c) first derivative-based partial least squares regression (PLSR) model. The PLSR model shows significantly better performance, with a lower RMSE and a line of best fit that has better agreement with the 1:1 line. Additional error metrics are listed in Table 2-3.

Similar patterns persist in the Peace–Athabasca Delta validation results, where the derivative-based PLSR model attains an $R^2$ of 0.80 relative to the 1:1 line, performing better than the MODIS band 1 model at 0.54 (Figure 2-6). The MODIS band 1 and generalized models return higher RMSEs (23.92 and 24.25 mg/L, respectively) than the AVIRIS-NG counterpart (15.95 mg/L). Whereas the PLSR model again shows a tight correlation along the fitted line and a slope closer to the 1:1 line, the univariate models appear to saturate around 60 mg/L. Clustering around this level is likely due to the distribution of sample points in the training dataset. The TSS retrieval model was iterated through a selection of the data points with increasing TSS loads. The resultant validation showed steadily degrading results with the inclusion of values above 109.64 mg/L, whereby the coefficients of determination and RMSEs decreased from 0.80 and 15.95, respectively. We therefore limited the validation sample set to this maximum value. It should be noted that the maximum TSS value of the 2016 Louisiana *in situ* training samples was 74.39 mg/L, and the resultant PLSR model's predictive capacity only degraded beyond 109.64 mg/L in this independent sample set.

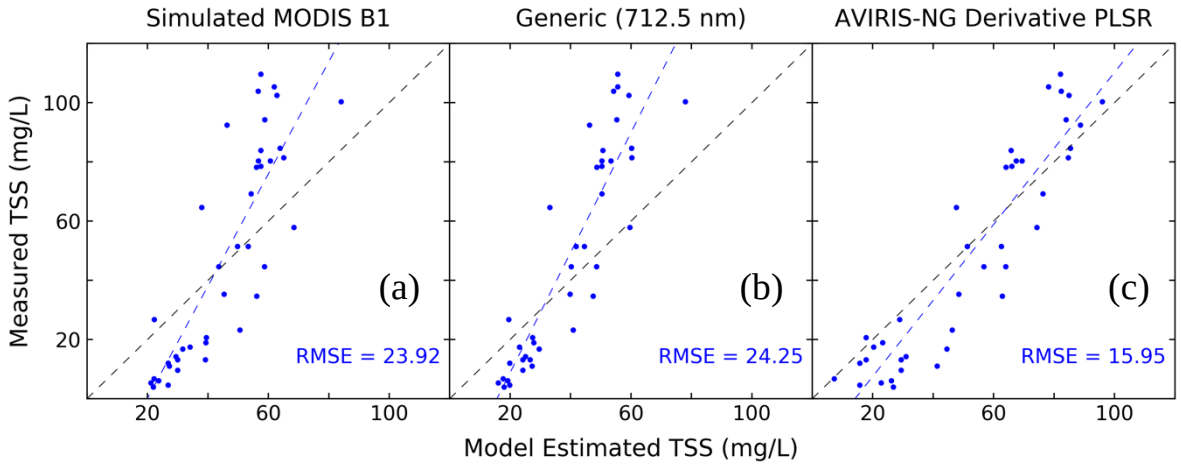


**Figure 2-6.** Peace-Athabasca Delta validation results. Produced from the total suspended solids (TSS, mg/L) retrieval using the field spectrometer dataset with the (a) simulated MODIS band 1 regression model, (b) generalized model at 712.5 nm, and (c) first derivative-based partial least squares regression (PLSR) model. Similar to Figure 2-5, the PLSR results here again show superior performance, with a lower RMSE and a line of best fit closer to the 1:1 line. Table 2-3 contains additional error metrics for the latter model.

Since the first derivative-based PLSR model performed the best across a variety of datasets, we used this approach to create maps of TSS (mg/L) from the AVIRIS imagery of the Atchafalaya River and surrounding waterways and the PRISM imagery of the San Francisco Bay–Delta Estuary's Grizzly Bay (Figure 2-7; Figure 2-8). Qualitative observations of the Louisiana TSS maps (Figure 2-7) show the region's sediment load concentrated in the Wax Lake outlet and Atchafalaya River, with high sediment concentrations aligning with higher runoff in the summer months compared to lower concentrations in October. Likewise, the Grizzly Bay map shows higher TSS values in the Suisun and Montezuma Sloughs, while the lakes west of Lake Athabasca show comparatively higher sediment concentrations than their surrounding waterways (Figure 2-8).

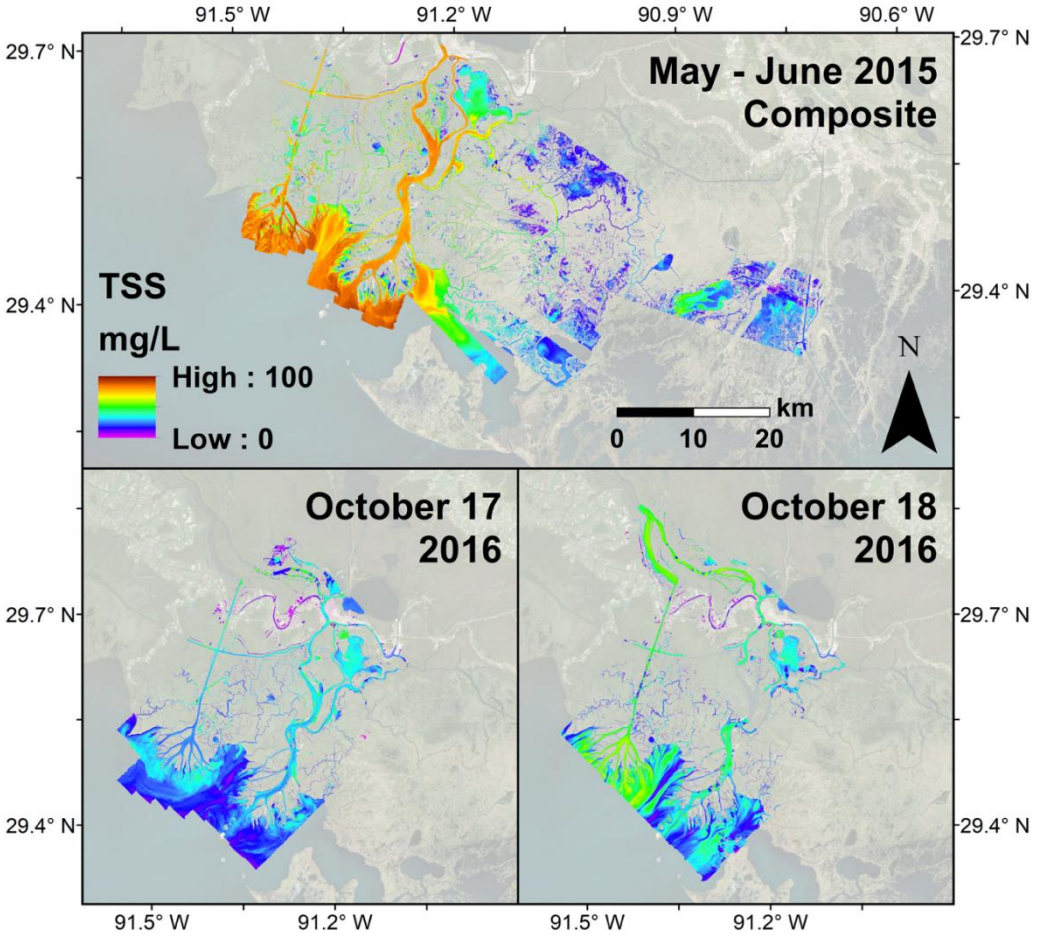


**Figure 2-7**. Total suspended solids (TSS, mg/L) maps of the Atchafalaya Basin. Produced with the modified derivative-based partial least squares (PLSR) algorithm applied to the 2015 and 2016 AVIRIS-NG mosaics.

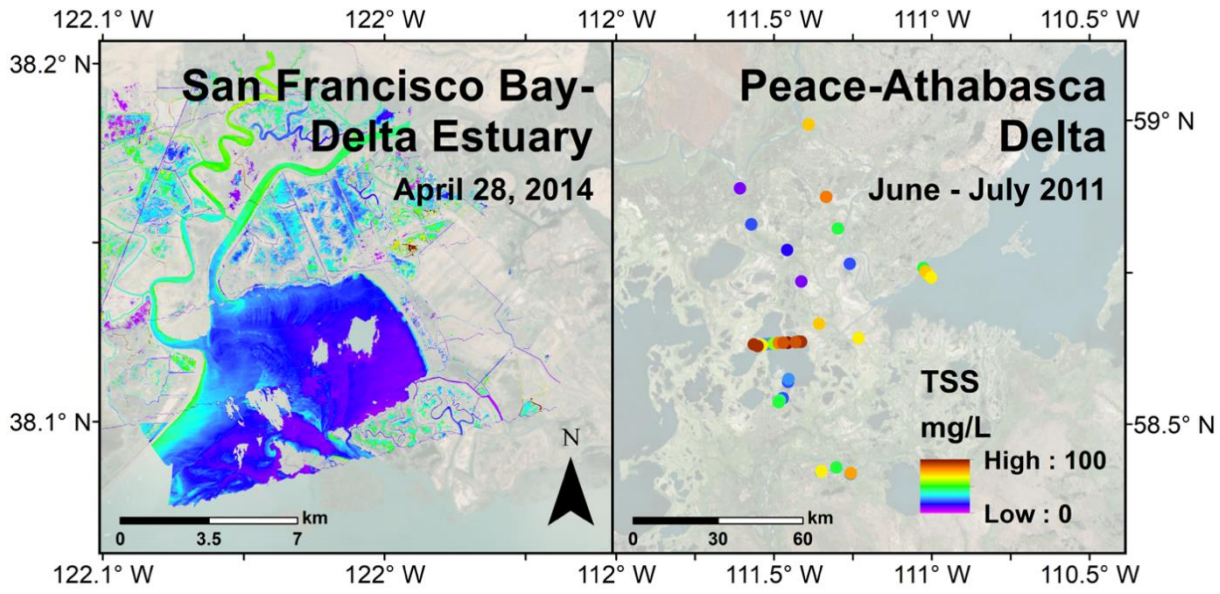


**Figure 2-8**. Validation site total suspended solids (TSS, mg/L) maps. Produced from the (a) San Francisco Bay–Delta Estuary PRISM dataset and (b) Peace–Athabasca Delta field spectrometer sample points.

### 2.5. Discussion

Our AVIRIS-NG first derivative-based PLSR model produced reasonably accurate estimates of TSS across several contrasting wetlands and time periods. Our results suggest that this approach may be broadly applicable for a variety of turbid deltaic and estuarine water bodies with TSS values up to approximately 110 mg/L. While the simpler single-band MODIS method exhibited low error when it was parameterized and applied within the same region, it is not applicable to other sites. Similarly, the generalized model (Nechad et al. 2010) did not attain low errors and good 1:1 fits across the various datasets. Our analysis demonstrates the robustness of the PLSR method based on spectral derivatives across different sites and periods, and its potential applicability to other areas.

Other water constituents present in the surface waters, including phytoplankton and CDOM, tend to vary independently from suspended sediments in these optically complex systems.

Furthermore, the characteristics and properties of suspended particles can vary with time and across systems, affecting the relationship between their inherent optical properties and concentrations. These factors can limit the applicability of simple empirical algorithms for retrieving waterborne variables like TSS (Lee et al. 1999). While these constituents were not measured from the 2015 and 2016 Louisiana water sample data, Walker and Rabalais' (2006) study of the chlorophyll *a* (Chl-a) dynamics in the Louisiana continental shelf show Chl-a concentrations ranging from approximately 3 to 9 µg/L throughout the year in their Atchafalaya River study site. Chl-a concentrations are likely typically higher than those in the San Francisco Bay–Delta Estuary site, but lower than in the Peace–Athabasca Delta (Table 2-3).

The relative concentration of water contents and optically active constituents may explain some of the error present in the model. To assess the impact of inorganic content variability, we examined the relationships between the predicted TSS residuals and silicate (Si) for both the 2015 and 2016 Louisiana data (Figure 2-A2). For these data, Si serves as a proxy for PIM and shows much higher concentrations in the May–June 2015 period where runoff is higher. Results show a weak correlation and a non-significant relationship between Si content and the 2016 predictions ($p = 0.08$, $R^2 = 0.14$) but a stronger correlation and more significant relationship for 2015 ($p = 0.03$, $R^2 = 0.28$). This indicates that the relative concentration of PIM and POM introduces some error into the model. However, given that the derivative-based PLSR model's error metrics perform best and the validation line of best fit is closest to the 1:1 line relative to all other tested models, we conclude that this approach diminishes the impact of PIM/POM differences on TSS retrievals. We additionally quantified the relationships of chlorophyll and CDOM concentrations with TSS residuals in the San Francisco Bay–Delta Estuary and Peace–Athabasca Delta datasets (Figure 2-A3; Figure 2-A4) to assess the impact of organic contents. Chl-a and CDOM

measurements in the Peace–Athabasca Delta were derived from fluorescence measurements made with a Eureka Manta Multiprobe, while Chl-a and CDOM in the San Francisco Bay Delta Estuary were taken from WETLabs WETStar fluorometer measurements, with Chl-a concentrations being derived from fluorescence with a linear calibration. Results show significant relationships at a $p<0.05$ level between TSS residuals and both Chl-a ($p = 0.04$, $R^2 = 0.32$) and CDOM absorption coefficients at 350 nm ($m^{-1}$) ($p < 0.01$, $R^2 = 0.62$) in the simulated MODIS band 1 model. This indicates that both constituents caused a systematic bias in the TSS retrieval. Conversely, the AVIRIS-NG derivative-based PLSR model showed no significant relationship for either Chl-a ($p = 0.07$) or CDOM ($p = 0.06$), indicating that the model was less impacted by those constituents within the present ranges. The Peace–Athabasca Delta data showed that Chl-a was not significant for either model ($p = 0.34$ for MODIS band 1, $p = 0.18$ for AVIRIS-NG derivative PLSR). However, CDOM was significant for both the MODIS ($p = 0.01$, $R^2 = 0.18$) and AVIRIS-NG ($p<0.01$, $R^2 = 0.48$) models. Higher CDOM likely cause increased error in the PLSR-based models, though the model effectively limits chlorophyll's influence on TSS retrievals. It should be noted that the sites examined in this study are not phytoplankton-dominated water bodies, with relatively low chlorophyll concentrations. It is thus possible that our model will be less applicable in waters where particles are dominated by phytoplankton. However, this analysis indicates that the derivative-based PLSR model diminishes the impact of such constituents on TSS retrievals relative to standard empirical reflectance-based approaches.

The linear relationship between $R_{rs}$ in the red region (MODIS Band 1) and TSS observed in coastal Louisiana (Figure 2-3) was reasonably strong, thereby suggesting that variations in the other water constituents and in the characteristics of the particles have limited effects on that relationship. Otherwise, the MODIS band 1 model would have returned significantly higher errors

for the 2015 validation dataset, as the models that included band 2 did. This is consistent with other general algorithms that make use of red spectral wavelengths as a proxy for turbidity or TSS (Nechad et al. 2010; Dogliotti et al. 2015; Stumpf and Pennock 1989). The superior performance of the other models that implement NIR reflectance in Chen et al.'s (2015) study may owe to their data's high sediment concentrations (5.8–577.2 mg/L), as reflectance across the broader NIR domain—rather than the narrower feature at 800 nm (Figure 2-2)—may then have greater predictive power. Validation of the MODIS band 1 in the San Francisco Bay–Delta Estuary shows poor model performance, most likely due to the differences in specific IOPs and mixture of water constituents in this environment compared to Louisiana. This poor performance demonstrates the fundamental limitation of many empirical reflectance-based sediment retrieval models, as they are prone to differences in water characteristics, instrumentation, and correction algorithms.

The derivative-based model empirically identified and exploited the variations in the reflectance shape that are most strongly associated with sediment concentration. The magnitude of the PLSR coefficients in the reflectance-based model does not significantly vary in the absorption features present across the utilized VNIR domain (Figure 2-2). The derivative-based model, conversely, puts significant weight on the narrow green and red spectral features, as well as the red-edge and NIR feature characteristics, as evidenced by its VIP and coefficient values. This causes the difference in RMSE values between the 2015 and 2016 validation for the various PLSR models in the Louisiana study area (Figure 2-4). While RMSE does not vary significantly for the models in 2016, the 2015 RMSE values show that derivative spectroscopy reduces error outside of the study site/period used for parameterization. Spectral derivatives, focused on the four highlighted regions, appear to mitigate the impacts of differences among hydrologic environments, waterborne constituents, and ranges of sediment concentrations. This is apparent in shallow

regions such as lakes, channels, and delta fringes that show appropriately low TSS values (Figure 2-7). As our sampling design accounted for a variety of apparent water turbidity, coloring, and depth, TSS retrievals in these water bodies do not appear to be errant despite multispectral sensors frequently mixing bottom reflectance signals with suspended sediment in optically shallow waters (Volpe et al. 2011). Furthermore, spectral derivatives are less sensitive to variability in illumination conditions and radiometric corrections (Chen et al. 1992; Demetriades-Shah et al. 1990). The location and shape of the peaks around 710 and 810 nm are primarily affected by the amount of scattering material (Gitelson 2007; Kutser et al. 2016), and are generally applicable for suspended sediment retrievals from sensors with the applicable bands. However, this study shows that employing spectral derivatives and VIP together allows for a more accurate characterization of those features. The spectral slope calculated across each identified feature's edge, for which imaging spectroscopy is necessary, serves as a superior predictor compared to the peak's reflectance magnitude as it describes the feature shape and diminishes the impact of variations in illumination intensity (Tsai and Philpot 1998). While the model incorporated into the TSS mapping algorithm exhibits low error (Table 2-4), and we have quantified the potential bias caused by some water constituents, some external error sources have not been quantified. One such error source pertains to individual flight lines in the AVIRIS-NG mosaic. A few select areas of water close to the scene's edge are more impacted by bidirectionality and sun glint. Variability in aerosols and adjacency effects are another likely source contributing to uncertainty in the retrievals. Similar to the case of band-ratio algorithms, the use of spectral derivatives rather than reflectance can spectrally-correlated sources of uncertainty (Tsai and Philpot 1998). Regardless, the TSS model and validated map results remain of sufficiently high quality for water quality monitoring.

We recommend that this proposed model not be applied to water bodies with suspended sediment concentrations exceeding the ranges assessed in our datasets, e.g., clear inland lakes (Spyrakos et al. 2018), extremely turbid waters (TSS > ~110 mg/L), or phytoplankton-dominated water bodies, as further work and data is needed to expand and assess its wider applicability. Our derivative model was able to accurately estimate TSS up to 109.64 mg/L, a value higher than the maximum TSS in the training data, 74.39 mg/L. However, in the highly turbid Peace–Athabasca Delta dataset, retrieval error increased with samples above 109.64 mg/L, where the original dataset extended above 3600 mg/L. The elevated MRE value in the Peace–Athabasca Delta dataset is also skewed by the high relative error in very low TSS ranges, despite the good correlation of predicted and actual values around the 1:1 line. Further, the higher maximum TSS value in the Peace–Athabasca Delta dataset relative to that of the Grizzly Bay dataset accounts for its higher RMSE (Figure 2-5; Figure 2-6). The ratios of the RMSE to maximum TSS sample value is not significantly different in Grizzly Bay (0.12) and Peace–Athabasca Delta (0.15). The extreme high and low turbidity cases indicate that the derivative-based PLSR model's current iteration is suited to moderate to high TSS ranges in deltaic or estuarine environments, and that a more comprehensive spectral library is needed to develop a universal model. Validation in these independent sites across appropriate TSS concentrations is indicative of imaging spectroscopy's power to identify important spectral features and of the strength of this empirical approach. TSS itself may not induce any unique spectral absorption features such as those caused by phytoplankton, but this analysis shows that TSS concentrations are closely associated with those identified here (Figure 2-2). Accurately identifying and quantifying those spectral features via imaging spectroscopy thus allows for TSS retrieval while controlling for other constituents' influence.

Our Louisiana TSS maps, especially the 2015 map that coincides with peak runoff provide insight into the patterns of wetland degradation and loss in our study area. Water gauge data (USGS gauge 07381600, lower Atchafalaya River at Morgan City, LA) shows gauge heights ranging from 4.96–5.98 feet for the May–June 2015 data timeframes. This shows high river stage, and thereby high runoff and sediment loads, for May–June 2015 compared to gauge heights of 2.53–2.91 and 2.89–3.21 feet on October 17 and 18, 2016, respectively. The maps show comparatively high TSS values in the main channels but little sediment supply in adjacent wetlands, a pattern that closely aligns with past distributions of wetland aggradation and degradation (Barras et al. 2003). Wetlands see little sediment delivery due to the prevalence of levees along main rivers and spoil banks alongside dredged channels throughout Louisiana. Whereas a natural distributary network consistently deposits sediment throughout the wetland area, the highly engineered Louisiana coast now sees sediment-bearing water largely constrained to the Mississippi River, Atchafalaya River, and the Wax Lake outlet. While these delta systems and their adjacent wetlands are aggrading, this dynamic has deprived the wetlands outside these systems of surficial material needed for accretion, making them vulnerable to RSLR and submergence in the process (Twilley et al. 2016).

## 2.6. Conclusion

This study successfully developed and validated an imaging spectroscopy method to estimate TSS concentrations in relatively turbid deltaic and estuarine water bodies. The model's transferability is an important quality for estimating sediment loads from different imaging spectrometer datasets, which will allow for future estimation of wetland sedimentation. The VIP-filtered first derivative-based PLSR model attained an $R^2$ of 0.83, indicating a strong correlation between the identified spectral characteristics and total suspended solids. Low RMSE values from

validation across multiple study sites and time periods also indicate the robustness of this empirical model. While simpler regression methods based on more readily available multispectral data such as MODIS may be sufficient for TSS retrieval in a given study site, we demonstrated that imaging spectroscopy facilitates more robust and transferable methods. In addition to the increased spectral information and the ability to identify important narrow spectral features, imaging spectroscopy also enables the use of spectral derivatives. Derivatives emphasize a spectrum's shape, which is a compounded function of both PIM and POM. While variation of these optical entities across sites limits the accuracy of TSS retrievals, using derivatives limits the influence of such confounding effects in remotely sensed imagery, increasing transferability compared to standard approaches.

Though this method appears accurate for the multiple study sites assessed here, we recommend that more data be collected in hydrologic settings with a wider range of sediment concentrations and characteristics to expand model applicability. Future studies may employ the data and methods described in this study to develop a more comprehensive spectral library, encompassing TSS ranges below and above this study's parameters, with a variety of optically active water constituent concentrations. This should entail efforts to assess varying concentrations of PIM and POM. Additionally, the features identified by VIP analysis can inform specialized sensor designs for consistent suspended sediment retrievals. Such an instrument may employ narrow bands at the left and rightmost edges of each feature to calculate a difference or index capturing its magnitude and position. Building on the transferability presented here, doing so will present another step towards a universal sediment retrieval algorithm.

## 2.7. References

Barras, J, S Beville, D Britsch, S Hartley, S Hawes, J Johnston, P Kemp, et al. 2003. "Historical

and Projected Coastal Louisiana Land Changes: 1978-2050." Vol. 334. US Geological Survey, Reston, VA.

Brando, Vittorio E., and Arnold G. Dekker. 2003. "Satellite Hyperspectral Remote Sensing for Estimating Estuarine and Coastal Water Quality." *IEEE Transactions on Geoscience and Remote Sensing* 41 (6 PART I): 1378–87.

Bue, Brian D., David R. Thompson, Michael Eastwood, Robert O. Green, Bo Cai Gao, Didier Keymeulen, Charles M. Sarture, Alan S. Mazer, and Huy H. Luong. 2015. "Real-Time Atmospheric Correction of AVIRIS-NG Imagery." *IEEE Transactions on Geoscience and Remote Sensing* 53 (12): 6419–28.

Burkett, Virginia R., David B. Ziklkoski, and David A. Hart. 2003. "Sea-Level Rise and Subsidence: Implications for Flooding in New Orleans, Louisiana." In *U.S. Geological Survey Subsidence Interest Group Conference: Proceedings of the Technical Meeting, Galveston, Texas, November 27-29, 2001*, 63–70.

Carrascal, Luis M., Ismael Galván, and Oscar Gordo. 2009. "Partial Least Squares Regression as an Alternative to Current Regression Methods Used in Ecology." *Oikos* 118 (5): 681–90.

Chen, Shuisen, Liusheng Han, Xiuzhi Chen, Dan Li, Lin Sun, and Yong Li. 2015. "Estimating Wide Range Total Suspended Solids Concentrations from MODIS 250-m Imageries: An Improved Method." *ISPRS Journal of Photogrammetry and Remote Sensing* 99: 58–69.

Chen, Zhiqiang, P. Curran, and Jim D. Hansom. 1992. "Derivative Reflectance Spectroscopy to Estimate Suspended Sediment Concentration." *Remote Sensing of Environment* 40 (1): 67–77.

Choe, Eunyoung, Freek van der Meer, Frank van Ruitenbeek, Harald van der Werff, Boudewijn

de Smeth, and Kyoung Woong Kim. 2008. “Mapping of Heavy Metal Pollution in Stream Sediments Using Combined Geochemistry, Field Spectroscopy, and Hyperspectral Remote Sensing: A Case Study of the Rodalquilar Mining Area, SE Spain.” *Remote Sensing of Environment* 112 (7): 3222–33.

Curran, Paul, and E.M. Novo. 1988. “The Relationship between Suspended Sediment Concentration and Remotely Sensed Spectral Radiance: A Review.” *Journal of Coastal Research* 4 (3): 351–68.

DeLaune, R. D., M. Kongchum, J. R. White, and A. Jugsujinda. 2013. “Freshwater Diversions as an Ecosystem Management Tool for Maintaining Soil Organic Matter Accretion in Coastal Marshes.” *Catena* 107: 139–44.

Demetriades-Shah, Tanvir H., Michael D. Steven, and Jeremy A. Clark. 1990. “High Resolution Derivative Spectra in Remote Sensing.” *Remote Sensing of Environment* 33 (1): 55–64.

Dogliotti, A. I., K. G. Ruddick, B. Nechad, D. Doxaran, and E. Knaeps. 2015. “A Single Algorithm to Retrieve Turbidity from Remotely-Sensed Data in All Coastal and Estuarine Waters.” *Remote Sensing of Environment* 156: 157–68.

Dorji, Passang, and Peter Fearns. 2016. “A Quantitative Comparison of Total Suspended Sediment Algorithms: A Case Study of the Last Decade for MODIS and Landsat-Based Sensors.” *Remote Sensing* 8 (10).

Doxaran, David, Jean Marie Froidefond, Samantha Lavender, and Patrice Castaing. 2002. “Spectral Signature of Highly Turbid Waters: Application with SPOT Data to Quantify Suspended Particulate Matter Concentrations.” *Remote Sensing of Environment* 81 (1): 149–61.

Doxaran, David, Nicolas Lamquin, Young Je Park, Constant Mazeran, Joo Hyung Ryu,

Menghua Wang, and Antoine Poteau. 2014. “Retrieval of the Seawater Reflectance for Suspended Solids Monitoring in the East China Sea Using MODIS, MERIS and GOCI Satellite Data.” *Remote Sensing of Environment* 146 (April 2012): 36–48.

Environmental Protection Agency. “ESS Method 340.2: Total Suspended Solids, Mass Balance (Dried at 103-105 ºC) Volatile Suspended Solids (Ignited at 550 ºC).” 1993. Madison, WI, USA.

Ericson, Jason P., Charles J. Vörösmarty, S. Lawrence Dingman, Larry G. Ward, and Michel Meybeck. 2006. “Effective Sea-Level Rise and Deltas: Causes of Change and Human Dimension Implications.” *Global and Planetary Change* 50 (1–2): 63–82.

Farrés, Mireia, Stefan Platikanov, Stefan Tsakovski, and Roma Tauler. 2015. “Comparison of the Variable Importance in Projection (VIP) and of the Selectivity Ratio (SR) Methods for Variable Selection and Interpretation.” *Journal of Chemometrics* 29 (10): 528–36.

Fichot, Cédric G., Bryan D. Downing, Brian A. Bergamaschi, Lisamarie Windham-Myers, Mark Marvin-Dipasquale, David R. Thompson, and Michelle M. Gierach. 2016. “High-Resolution Remote Sensing of Water Quality in the San Francisco Bay-Delta Estuary.” *Environmental Science and Technology* 50 (2): 573–83.

Forget, Philippe, Pierre Broche, and Jean Jacques Naudin. 2001. “Reflectance Sensitivity to Solid Suspended Sediment Stratification in Coastal Water and Inversion: A Case Study.” *Remote Sensing of Environment* 77 (1): 92–103.

Gao, Bo Cai, Kathleen B. Heidebrecht, and Alexander F.H. Goetz. 1993. “Derivation of Scaled Surface Reflectances from AVIRIS Data.” *Remote Sensing of Environment* 44 (2–3): 165–78.

Gitelson, A. 2007. “The Peak near 700 Nm on Radiance Spectra of Algae and Water:

Relationships of Its Magnitude and Position with Chlorophyll Concentration." *International Journal of Remote Sensing* 13 (17): 3367–73.

Glysson, G. Douglas, John R. Gray, and Lisa M. Conge. 2000. "Adjustment of Total Suspended Solids Data for Use in Sediment Studies." In *Building Partnerships*, 104:1–10. Reston, VA: American Society of Civil Engineers.

Gómez, Raúl Aguirre. 2014. "Spectral Reflectance Analysis of the Caribbean Sea." *Geofisica Internacional* 53 (4): 385–98.

Griffin, Claire G., Karen E. Frey, John Rogan, and Robert M. Holmes. 2011. "Spatial and Interannual Variability of Dissolved Organic Matter in the Kolyma River, East Siberia, Observed Using Satellite Imagery." *Journal of Geophysical Research: Biogeosciences* 116 (3): 1–12.

Hamlin, L., R. O. Green, P. Mouroulis, M. Eastwood, D. Wilson, M. Dudik, and C. Paine. 2011. "Imaging Spectrometer Science Measurements for Terrestrial Ecology: AVIRIS and New Developments." *IEEE Aerospace Conference Proceedings*, 1–8.

Han, Z, Y -Q Jin, and C -X Yun. 2006. "Suspended Sediment Concentrations in the Yangtze River Estuary Retrieved from the CMODIS Data." *International Journal of Remote Sensing* 27 (19): 4329–36.

Jensen, Daniel J., Marc Simard, Kyle C. Cavanaugh, and David R. Thompson. 2017. "Imaging Spectroscopy BRDF Correction for Mapping Louisiana's Coastal Ecosystems." *IEEE Transactions on Geoscience and Remote Sensing* 56 (3): 1739–48.

Knaeps, E., K. G. Ruddick, D. Doxaran, A. I. Dogliotti, B. Nechad, D. Raymaekers, and S. Sterckx. 2015. "A SWIR Based Algorithm to Retrieve Total Suspended Matter in Extremely Turbid Waters." *Remote Sensing of Environment* 168: 66–79.

Krauss, Ken W, Karen L McKee, Catherine E Lovelock, Donald R Cahoon, Neil Saintilan, Ruth Reef, and Luzhen Chen. 2014. “How Mangrove Forests Adjust to Rising Sea Level.” *The New Phytologist* 202 (1): 19–34.

Krauss, Ken W., Jamie A. Duberstein, Thomas W. Doyle, William H. Conner, Richard H. Day, L. Wayne Inabinette, and Julie L. Whitbeck. 2009. “Site Condition, Structure, and Growth of Baldcypress along Tidal/Non-Tidal Salinity Gradients.” *Wetlands* 29 (2): 505–19.

Kromkamp, Jacco C., Edward P. Morris, Rodney M. Forster, Claire Honeywill, Scott Hagerthey, and David M. Paterson. 2006. “Relationship of Intertidal Surface Sediment Chlorophyll Concentration to Hyperspectral Reflectance and Chlorophyll Fluorescence.” *Estuaries and Coasts* 29 (2): 183–96.

Kutser, Tiit, Birgot Paavel, Charles Verpoorter, Martin Ligi, Tuuli Soomets, Kaire Toming, and Gema Casal. 2016. “Remote Sensing of Black Lakes and Using 810 Nm Reflectance Peak for Retrieving Water Quality Parameters of Optically Complex Waters.” *Remote Sensing* 8 (6): 497.

Lee, Zhongping, Curtis D. Mobley, Jennifer S. Patch, Kendall L. Carder, and Robert G. Steward. 1999. “Hyperspectral Remote Sensing for Shallow Waters: Deriving Bottom Depths and Water Properties by Optimization.” *Applied Optics* 38 (18): 3831.

Lee, Zhongping, Shaoling Shang, Gong Lin, Jun Chen, and David Doxaran. 2016. “On the Modeling of Hyperspectral Remote-Sensing Reflectance of High-Sediment-Load Waters in the Visible to Shortwave-Infrared Domain.” *Applied Optics* 55 (7): 1738–50.

Li, Rong-Rong, Yoram J. Kaufman, Bo-Cai Gao, and Curtiss O. Davis. 2003. “Remote Sensing

of Suspended Sediments and Shallow Coastal Waters." *IEEE Transactions on Geoscience and Remote Sensing* 41 (3): 559–66.

Long, Colleen M., and Tamlin M. Pavelsky. 2012. "Water Quality and Spectral Reflectance, Peace-Athabasca Delta, Canada, 2010–2011." ORNL DAAC. Oak Ridge, TN, USA.

Long, Colleen M., and Tamlin M. Pavelsky. 2013. "Remote Sensing of Suspended Sediment Concentration and Hydrologic Connectivity in a Complex Wetland Environment." *Remote Sensing of Environment* 129: 197–209.

Louchard, Eric M., R. Pamela Reid, Carol F. Stephens, Curtiss O. Davis, Robert A. Leathers, T. Valerie Downes, and Robert Maffione. 2002. "Derivative Analysis of Absorption Features in Hyperspectral Remote Sensing Data of Carbonate Sediments." *Optics Express* 10 (26): 1573–84.

Martínez-Carreras, Núria, Andreas Krein, Thomas Udelhoven, Francesc Gallart, Jean F. Iffly, Lucien Hoffmann, Laurent Pfister, and Desmond E. Walling. 2010. "A Rapid Spectral-Reflectance-Based Fingerprinting Approach for Documenting Suspended Sediment Sources during Storm Runoff Events." *Journal of Soils and Sediments* 10 (3): 400–413.

Mehmood, Tahir, Kristian Hovde Liland, Lars Snipen, and Solve Sæbø. 2012. "A Review of Variable Selection Methods in Partial Least Squares Regression." *Chemometrics and Intelligent Laboratory Systems* 118 (September 2017): 62–69.

Miller, Richard L., and Brent A. McKee. 2004. "Using MODIS Terra 250 m Imagery to Map Concentrations of Total Suspended Matter in Coastal Waters." *Remote Sensing of Environment* 93 (1–2): 259–66.

Morel, André, and Bernard Gentili. 1996. "Diffuse Reflectance of Oceanic Waters. III.

Implication of Bidirectionality for the Remote-Sensing Problem." *Applied Optics* 35 (24): 4850–62.

Morris, James T., P. V. Sundareshwar, Christopher T. Nietch, Björn Kjerfve, and D. R. Cahoon. 2002. "Responses of Coastal Wetlands to Rising Sea Level." *Ecology* 83 (10): 2869–77.

Morton, Robert, Julie Bernier, and John Barras. 2006. "Evidence of Regional Subsidence and *Associated Interior Wetland Loss Induced by Hydrocarbon Production, Gulf Coast Region,* USA." *Environmental Geology* 50 (2): 261–74.

Nechad, B., K. G. Ruddick, and Y. Park. 2010. "Calibration and Validation of a Generic Multisensor Algorithm for Mapping of Total Suspended Matter in Turbid Waters." *Remote Sensing of Environment* 114 (4): 854–66.

Olmanson, Leif G., Patrick L. Brezonik, and Marvin E. Bauer. 2013. "Airborne Hyperspectral Remote Sensing to Assess Spatial Distribution of Water Quality Characteristics in Large Rivers: The Mississippi River and Its Tributaries in Minnesota." *Remote Sensing of Environment* 130: 254–65.

Östlund, Catherine, Peter Flink, Niklas Strömbeck, Don Pierson, and Tommy Lindell. 2001. "Mapping of the Water Quality of Lake Erken, Sweden, from Imaging Spectrometry and Landsat Thematic Mapper." *Science of The Total Environment* 268 (1–3): 139–54.

Ouillon, S., P. Douillet, and S. Andréfouët. 2004. "Coupling Satellite Data with in Situ Measurements and Numerical Modeling to Study Fine Suspended-Sediment Transport: A Study for the Lagoon of New Caledonia." *Coral Reefs* 23 (1): 109–22.

Palacios, Sherry L., Raphael M. Kudela, Liane S. Guild, Kendra H. Negrey, Juan Torres-Perez,

and Jennifer Broughton. 2015. “Remote Sensing of Phytoplankton Functional Types in the Coastal Ocean from the HyspIRI Preparatory Flight Campaign.” *Remote Sensing of Environment* 167: 269–80.

Pavelsky, Tamlin M., and Laurence C. Smith. 2009. “Remote Sensing of Suspended Sediment Concentration, Flow Velocity, and Lake Recharge in the Peace-Athabasca Delta, Canada.” *Water Resources Research* 45 (11): 1–16.

Ritchie, Jerry C, and Charles M Cooper. 2001. “Remote Sensing Techniques for Determining Water Quality: Applications to TMDLs.” In *TMDL Science Issues Conference*, 367–75.

Senay, Gabriel B., Naseer A. Shafique, Bradley C. Autrey, Florence Fulk, and Susan M. Cormier. 2001. “The Selection of Narrow Wavebands for Optimizing Water Quality Monitoring on the Great Miami River, Ohio Using Hyperspectral Remote Sensor Data.” *Journal of Spatial Hydrology* 1: 1–22.

Song, Conghe, Brian L. White, and Benjamin W. Heumann. 2011. “Hyperspectral Remote Sensing of Salinity Stress on Red (Rhizophora Mangle) and White (Laguncularia Racemosa) Mangroves on Galapagos Islands.” *Remote Sensing Letter*s 2 (3): 221–30.

Spyrakos, Evangelos, Ruth O’Donnell, Peter D. Hunter, Claire Miller, Marian Scott, Stefan G. H. Simis, Claire Neil, et al. 2017. “Optical Types of Inland and Coastal Waters.” *Limnology and Oceanography*.

Sterckx, Sindy, Els Knaeps, Mark Bollen, Koen Trouw, and Rik Houthuys. 2007. “Retrieval of Suspended Sediment from Advanced Hyperspectral Sensor Data in the Scheldt Estuary at Different Stages in the Tidal Cycle.” *Marine Geodesy* 30 (1–2): 97–108.

Stumpf, Richard P., and Jonathan R. Pennock. 1989. “Calibration of a General Optical Equation

for Remote Sensing of Suspended Sediments in a Moderately Turbid Estuary." *Journal of Geophysical Research* 94 (C10): 14363.

Thompson, David R., Bo Cai Gao, Robert O. Green, Dar A. Roberts, Philip E. Dennison, and Sarah R. Lundeen. 2015. "Atmospheric Correction for Global Mapping Spectroscopy: ATREM Advances for the HyspIRI Preparatory Campaign." *Remote Sensing of Environment* 167: 64–77.

Tobias, Randall D. 1995. "An Introduction to Partial Least Squares Regression." *Proc. Ann. SAS Users Group Int. Conf., 20th, Orlando, FL,* 2–5.

Tsai, Fuan, and William Philpot. 1998. "Derivative Analysis of Hyperspectral Data." *Remote Sensing of Environment* 66 (1): 41–51.

Twilley, Robert R., Samuel J. Bentley, Qin Chen, Douglas A. Edmonds, Scott C. Hagen, Nina S.N. Lam, Clinton S. Willson, et al. 2016. "Co-Evolution of Wetland Landscapes, Flooding, and Human Settlement in the Mississippi River Delta Plain." *Sustainability Science* 11 (4): 711–31.

Volpe, V., S. Silvestri, and M. Marani. 2011. "Remote Sensing Retrieval of Suspended Sediment Concentration in Shallow Waters." *Remote Sensing of Environment* 115 (1): 44–54.

Walker, Nan D, and Nancy N Rabalais. 2006. "Relationships among Satellite Chlorophyll a, River Inputs, and Hypoxia on the Louisiana Continental Shelf, Gulf of Mexico." *Estuaries and Coasts* 29 (6): 1081–93.

Wang, J. J., and X. X. Lu. 2010. "Estimation of Suspended Sediment Concentrations Using Terra MODIS: An Example from the Lower Yangtze River, China." *Science of the Total Environment* 408 (5): 1131–38.

Warrick, J. A., L. A. K. Mertes, D. A. Siegel, and C. Mackenzie. 2004. "Estimating Suspended

Sediment Concentrations in Turbid Coastal Waters of the Santa Barbara Channel with SeaWiFS." *International Journal of Remote Sensing* 25 (10): 1995–2002.

## 2.8. Appendix

**Table 2-A1.** AVIRIS-NG PLSR Models

| Wavelength (nm) | Reflectance Coefficient | Derivative Coefficient |
|---|---|---|
| 521.69 | −114.35 | |
| 526.70 | −121.29 | |
| 531.71 | −126.00 | |
| 536.72 | −128.85 | |
| 541.73 | −131.69 | |
| 546.73 | −133.50 | |
| 551.74 | −133.90 | |
| 556.75 | −134.03 | |
| 561.76 | −133.04 | |
| 566.77 | −130.00 | |
| 571.78 | −125.50 | |
| 576.79 | −119.75 | |
| 581.80 | −110.65 | |
| 586.80 | −100.04 | |
| 591.81 | −86.46 | |
| 596.82 | −63.45 | 4916.79 |
| 601.83 | −36.07 | 4254.01 |
| 606.84 | −21.55 | |
| 611.85 | −11.63 | |
| 616.86 | −1.30 | |
| 621.86 | 7.53 | |
| 626.87 | 16.19 | |
| 631.88 | 22.89 | |
| 636.89 | 28.18 | |
| 641.90 | 33.72 | |
| 646.91 | 41.23 | |

| **Table 2-A1 Continued** | | |
|---|---|---|
| 651.92 | 53.61 | |
| 656.93 | 77.19 | 5340.10 |
| 661.93 | 105.52 | 5428.36 |
| 666.94 | 128.27 | 4177.92 |
| 671.95 | 144.25 | |
| 676.96 | 153.37 | |
| 681.97 | 154.90 | |
| 686.98 | 142.27 | |
| 691.99 | 129.23 | |
| 696.99 | 129.27 | |
| 702.00 | 141.75 | 1876.78 |
| 707.01 | 163.07 | 2963.11 |
| 712.02 | 187.93 | 2535.39 |
| 717.03 | 208.03 | 662.15 |
| 722.04 | 218.15 | −1707.08 |
| 727.05 | 217.17 | −4655.07 |
| 732.06 | 202.14 | −5867.71 |
| 737.06 | 186.78 | −3510.22 |
| 767.12 | 185.40 | |
| 772.12 | 188.71 | |
| 777.13 | 192.79 | |
| 782.14 | 198.06 | |
| 787.15 | 205.12 | |
| 792.16 | 211.90 | |
| 797.17 | 218.93 | |
| 802.18 | 225.51 | |
| 807.19 | 229.60 | |
| 812.19 | 229.79 | |
| 817.20 | 225.67 | −2548.37 |
| 822.21 | 213.75 | −5553.51 |
| 827.22 | 188.28 | −7608.68 |
| 832.23 | | −5955.38 |
| 837.24 | | −3114.65 |
| Constant | 10.13 | 12.17 |

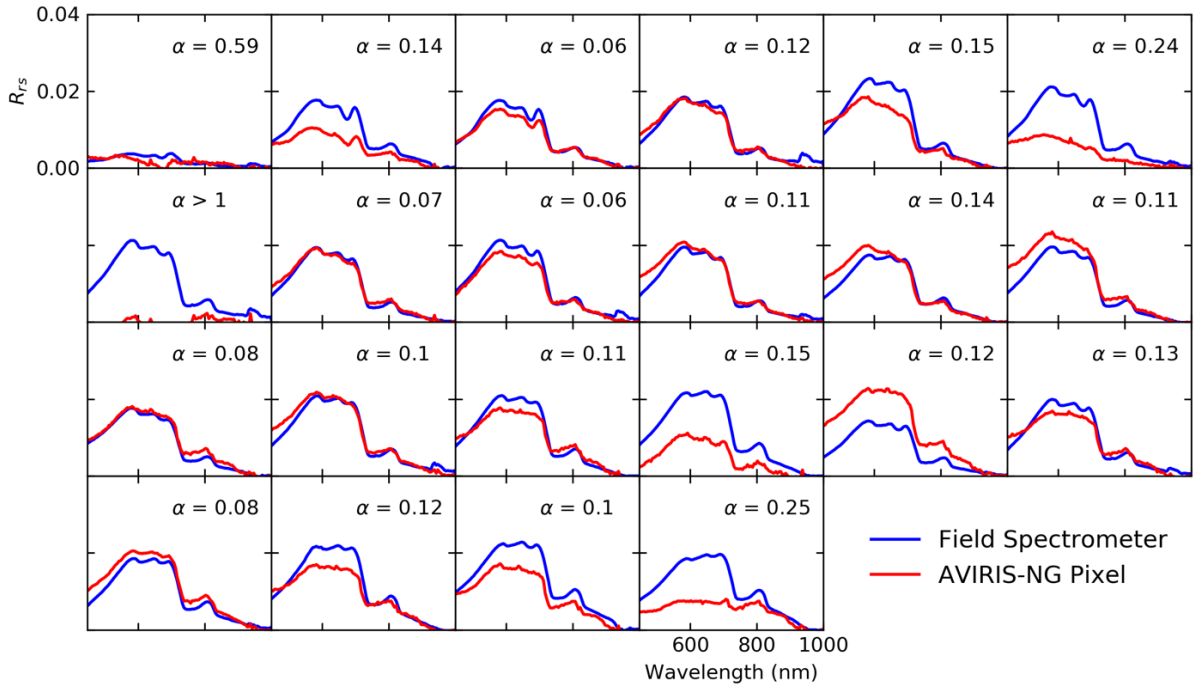


**Figure 2-A1.** Match between *in situ* and airborne instrument spectra. Plots show the remote sensing reflectance spectra derived from the ASD FieldSpec® 3 spectrometer and the corresponding AVIRIS-NG pixel spectra, with all corrections applied. Spectral angle, represented by $\alpha$, is a measure of the difference in overall spectral shape between the two samples, with 0 denoting a perfect similarity.

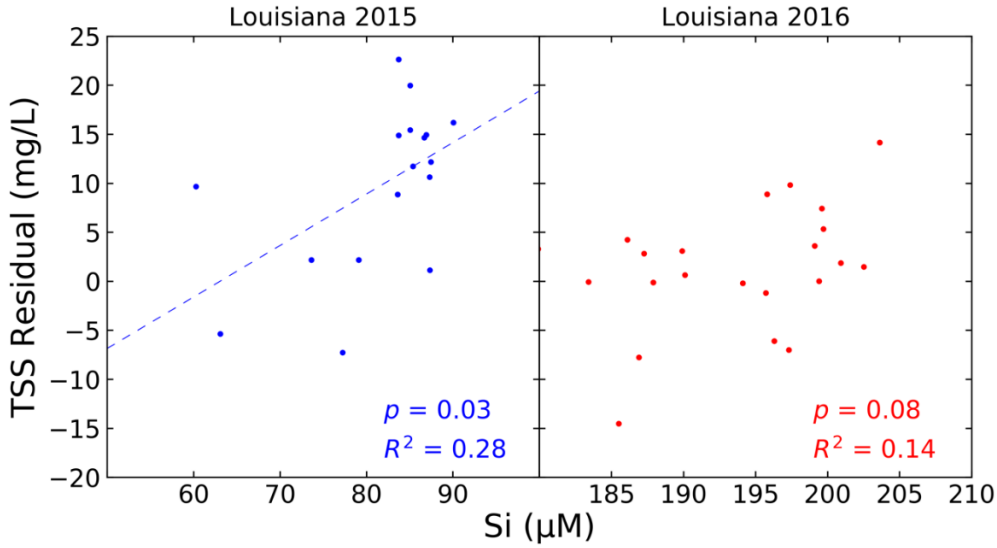


**Figure 2-A2.** Statistical relationships between predicted TSS residuals and silicate. Samples measured in micromolar for the 2015 and 2016 Louisiana *in situ* validation datasets. Silicate here serves as a proxy for particulate inorganic matter. The regression line is plotted for the 2015 data's relationships that is significant at a $p < 0.05$ level.

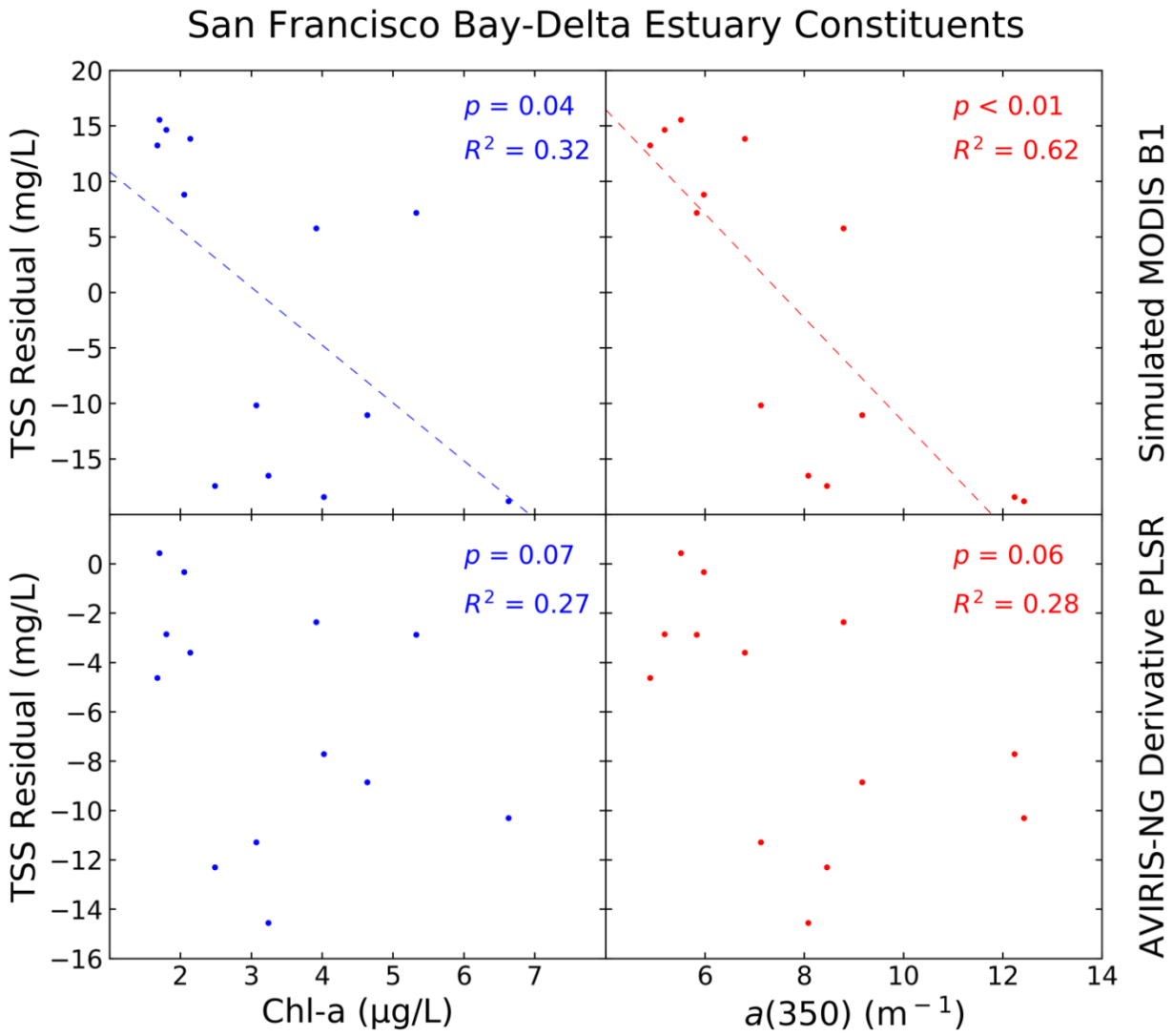


**Figure 2-A3.** San Francisco Bay–Delta Estuary relationships between TSS residuals and constituents. These include chlorophyll *a* concentration (left) and the CDOM absorption coefficient at 350 nm (right) for both the simulated MODIS B1 model (top) and the AVIRIS-NG derivative-based PLSR model (bottom). Regression lines are plotted for relationships that are significant at a $p < 0.05$ level.

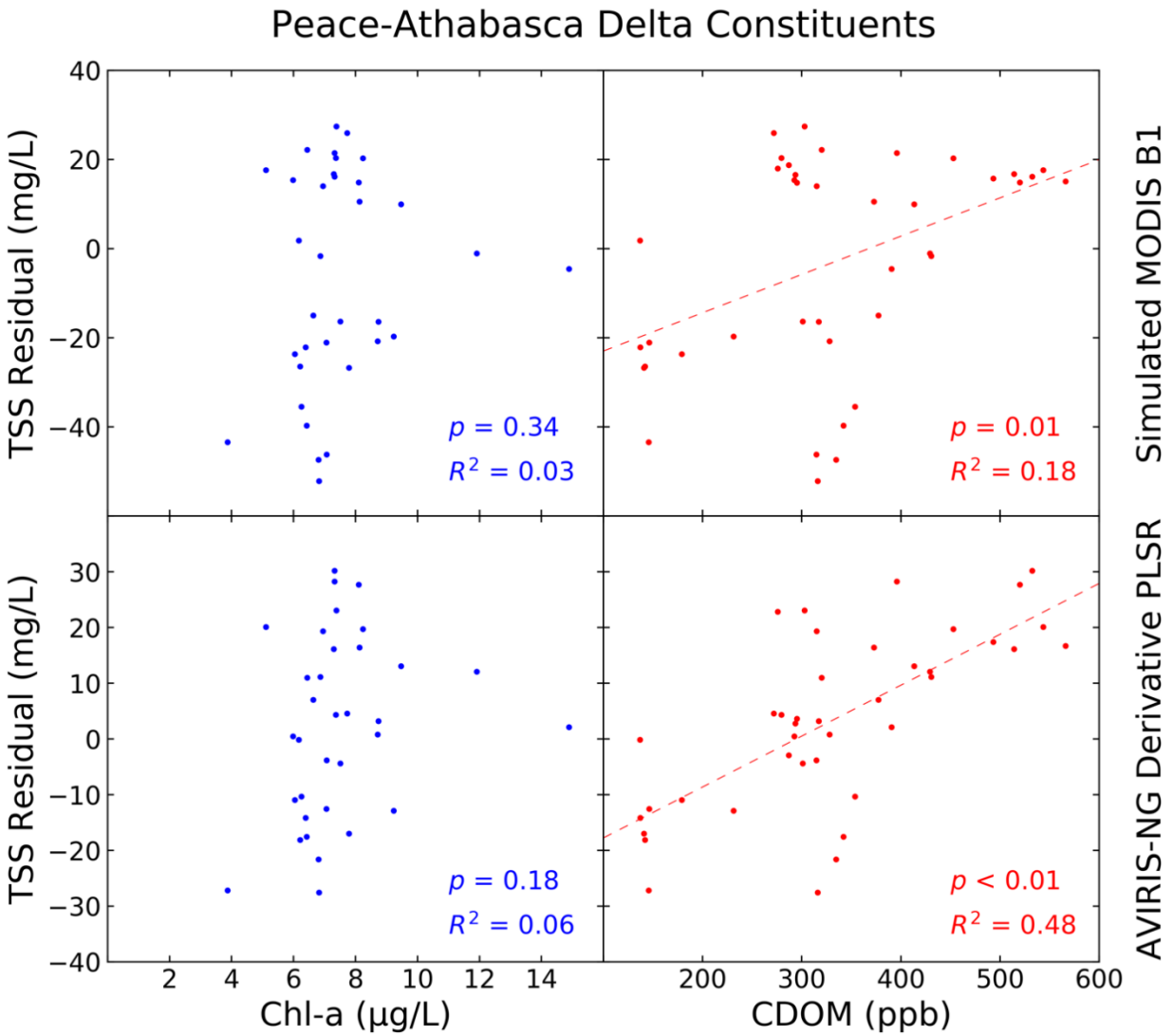


**Figure 2-A4.** Peace–Athabasca Delta relationships between TSS residuals and constituents. These include chlorophyll *a* (left) and CDOM (right) concentrations for both the simulated MODIS B1 model (top) and the AVIRIS-NG derivative-based PLSR model (bottom). CDOM is listed in parts per billion of a standard solution used to calibrate the fluorescence probe. Regression lines are plotted for relationships that are significant at a $p < 0.05$ level.

# Chapter 3

## Integrating Imaging Spectrometer and Synthetic Aperture Radar Data for Estimating Wetland Vegetation Aboveground Biomass in Coastal Louisiana

### 3.1. Abstract

Aboveground biomass (AGB) plays a critical functional role in coastal wetland ecosystem stability, with high biomass vegetation contributing to organic matter production, sediment accretion potential, and the surface elevation's ability to keep pace with relative sea level rise. Many remote sensing studies have employed either imaging spectrometer or synthetic aperture radar (SAR) for AGB estimation in various environments for assessing ecosystem health and carbon storage. This study leverages airborne data from NASA's Airborne Visible/Infrared Imaging Spectrometer-Next Generation (AVIRIS-NG) and Uninhabited Aerial Vehicle Synthetic Aperture Radar (UAVSAR) to assess their unique capabilities in combination to estimate AGB in coastal deltaic wetlands. Here we develop AGB models for emergent herbaceous and forested wetland vegetation in coastal Louisiana. In addition to horizontally emitted, vertically received (HV) backscatter, SAR parameters are expressed by the Freeman–Durden polarimetric decomposition components representing volume and double-bounce scattering. The imaging spectrometer parameters include normalized difference vegetation index (NDVI), reflectance from 290 visible-shortwave infrared (VSWIR) bands, the first derivatives from those bands, or partial least squares (PLS) x-scores derived from those data. Model metrics and cross-validation indicate that the integrated models using the Freeman-Durden components and PLS x-scores improve AGB estimates for herbaceous and forested wetland vegetation. In our study domain over Louisiana's Wax Lake Delta (WLD), we estimated a mean herbaceous wetland AGB of 3.58 Megagrams/hectare (Mg/ha) and a total of 3551.31 Mg over 9.92 $km^2$, and a mean forested wetland

AGB of 294.78 Mg/ha and a total of 27,499.14 Mg over 0.93 $km^2$. While the addition of SAR-derived values to imaging spectrometer data provides a nominal error decrease for herbaceous wetland AGB, this combination significantly improves forested wetland AGB prediction. This integrative approach is particularly effective in forested wetlands as canopy-level biochemical characteristics are captured by the imaging spectrometer in addition to the variable structural information measured by the SAR.

### 3.2. Introduction

In coastal wetlands, as in other ecosystems, aboveground biomass (AGB) is an important indicator of vegetation health and productivity, as well as a key parameter for quantifying marsh response to sea level rise and resulting carbon storage loss. Vegetation biomass contributes to several ecosystem processes with feedbacks including nutrient allocation, sedimentation and accretion rates, riverine and tidal inundation, and weather patterns (Zhang et al. 1997; Morris et al. 2002; Mudd et al. 2009; Adam et al. 2010). Estimation and monitoring of wetland biomass, or "blue carbon," are needed to assess a wetland's ability to trap exogenic sediment and produce organic soils that increase surface elevation relative to sea level rise (Byrd et al. 2014; Thomas et al. 2019). Accurate AGB maps can be used to analyze and predict changes in wetland vegetation cover and total carbon storage (Morris et al. 2002; Craft et al. 2009; Kirwan and Guntenspergen 2010), and accordingly understand its impact on landscape and hydrological processes (Turpie et al. 2015). In addition to furthering our understanding of these processes, the observed spatial variability in biomass distributions can help support conservation and restoration efforts, making the research and development of optimized remote sensing methods critical (Schile et al. 2014).

Remote sensing data from satellite and airborne instruments, supported by *in situ* field measurements, offer the ability to develop empirical AGB models that can assess of ecosystem health and change (Adam et al. 2010; Byrd et al. 2014). These models depend on relationships between one or several remotely sensed parameters and AGB. Broadband multispectral data is the most widely distributed and utilized remote sensing data. With the ubiquity of multispectral satellite datasets, normalized difference vegetation index (NDVI), the normalized ratio of a pixel's near-infrared (NIR) and red reflectance that estimates plant photosynthetic activity (Rouse et al. 1973), is the most commonly used optical variable for biomass mapping (Li et al. 2007; Klemas 2013). Beyond the level of canopy coverage affecting a pixel's radiance/reflectance signal, optical data does not easily provide information on plant structure. Different approaches employ synthetic aperture radar (SAR) data, as a radar signal's backscatter is sensitive to vegetation structure and thereby AGB (Hong and Wdowinski 2014). There are often relationships between AGB and optical or radar backscatter variables, though the relationships are frequently logarithmic as parameters saturate at high biomass values (Adam et al. 2010; Li et al. 2007). Regression analysis provides the primary empirical tool for developing remote sensing-based data models that can be scaled to imagery and produce biomass maps. Multivariate regression analysis techniques can utilize the breadth of a sensor's spectral bands or combine data from multiple sensors to increase a model's predictive capability (Byrd et al. 2014).

Imaging spectroscopy—or hyperspectral remote sensing—can leverage hundreds of contiguous narrow bands and complete spectral response for estimating AGB. Imaging spectrometer data can thus improve on existing methods or enable new ones. For example, narrow bands may be used to calculate indices with a more sensitive response for univariate regression (Elvidge and Chen 1995), or multivariate techniques may be employed that utilize the continuous

spectral data. A comprehensively measured visible-shortwave infrared (VSWIR) reflectance spectrum provides a powerful basis for estimating vegetation properties, as with canopy foliar traits and other environmental variables (Townsend et al. 2003; Townsend et al. 2013). The spectral signature measured by the multitude of bands—either by an imaging spectrometer or an *in situ* field spectrometer (Byrd et al. 2014)—can optimize predictive capability and disentangle a surface's spectral properties in relation to its AGB by emphasizing the spectral features that are most associated with canopy coverage, water content, and photosynthetic activity (Byrd et al. 2014; Cho et al. 2007). Utilizing the first derivative spectra, rather than reflectance or radiance, removes pixel brightness variability and further enhances spectral features which may in turn be correlated with AGB (Tsai and Philpot 1998). The resultant regression models will typically be more sensitive to those key spectral features' shapes and attain a higher coefficient of determination (Byrd et al. 2014). Imaging spectroscopy is thus potentially invaluable for attaining information on vegetation biochemical composition that can relate to biomass.

Synthetic aperture radar (SAR) is an active microwave instrument sensitive to structural information not contained within a plant's spectral signature. The scattering mechanisms and measured backscatter amplitudes can be used to make inferences of vegetation type, surface conditions, and structural characteristics—including AGB (Henderson and Lewis 2008). Among these frequently studied measures is leaf area index (LAI), which is often used as a measurement from which AGB can be estimated (Treuhaft et al. 2003). As several studies have demonstrated empirical relationships between LAI and various backscatter metrics (Wang et al. 2009; Manninen et al. 2005; Ramsey et al. 2015), leaf abundance impacts SAR backscatter and contributes to AGB estimates. The primary SAR-based AGB estimation method typically involves conducting a regression analysis using cross-polarized horizontally emitted, vertically received (HV) data. HV

backscatter measurements represent the response from volumetric scattering resulting from the radar signal's interaction with a vegetation canopy before returning to the sensor (Hong and Wdowinski 2014). Other scattering mechanisms include surface scattering—the signal's specular reflection off a flat surface—and double bounce—where the signal is reflected by a surface onto a vertical object, effectively forming a right angle, scattering the signal towards the instrument (Hong and Wdowinski 2014; Neumann et al. 2012). A polarimetric decomposition estimate expresses the contribution of each of these three scattering mechanisms to the observed backscatter signal (Rosen et al. 2000; Mohammadimanesh et al. 2018), and is useful for vegetation classification and AGB modeling (Neumann et al. 2012).

There is great potential for developing accurate methods to estimate wetland AGB by integrating the biochemical data derived from imaging spectroscopy with the structural information provided by SAR (Klemas 2013; Sinha et al. 2015). Past studies have merged these datasets for forest AGB estimates, either directly with regression (Byrd et al. 2018) or via leaf area index optimization (Treuhaft et al. 2003). Other studies use similar approaches with imaging spectroscopy and LiDAR, though they rely on band selection and so do not assimilate the full range of spectral information for model development (Laurin et al. 2004; Peerbhay et al. 2013). This study examines the contribution of each remote sensing variable to both herbaceous and forested wetland AGB. Louisiana's Wax Lake Delta offers a valuable case study to estimate coastal wetland biomass estimation, as it is a prograding delta located within the greater Mississippi Deltaic Plain (MDP) where wetlands are severely degrading and receding (Twilley et al. 2016; Bevington et al. 2017) (Figure 3-1). Coastal Louisiana lost an estimated 4833 $km^2$ of marsh area from 1932 to 2016, accounting for roughly 25% of its coastal wetlands (Couvillion et al. 2017). A better understanding of biomass stocks and distributions in these prograding deltaic

wetland areas may inform future restoration efforts. AGB has been examined in the Wax Lake Delta (WLD), but as part of a broader national-scale assessment of carbon stocks using satellite data that did not resolve the local-scale AGB distributions in the WLD (Byrd et al. 2015; Byrd et al. 2018) or as part of a regional-scale AGB assessment that could not find a robust relationship with available *in situ* and satellite data (Thomas et al. 2019). This study's primary objective, then, is to develop an integrated empirical approach for estimating AGB that leverages the unique capabilities provided by each data type collected in tandem by airborne instruments. In doing so, we interpret the contributions of different spectral features and radar scattering components to the AGB estimation, for both herbaceous and forested wetland vegetation. We then apply the models that attain optimal performance metrics, in both parameterization and cross-validation, to imaging spectrometer and SAR data collected over Louisiana's WLD (Figure 3-1).

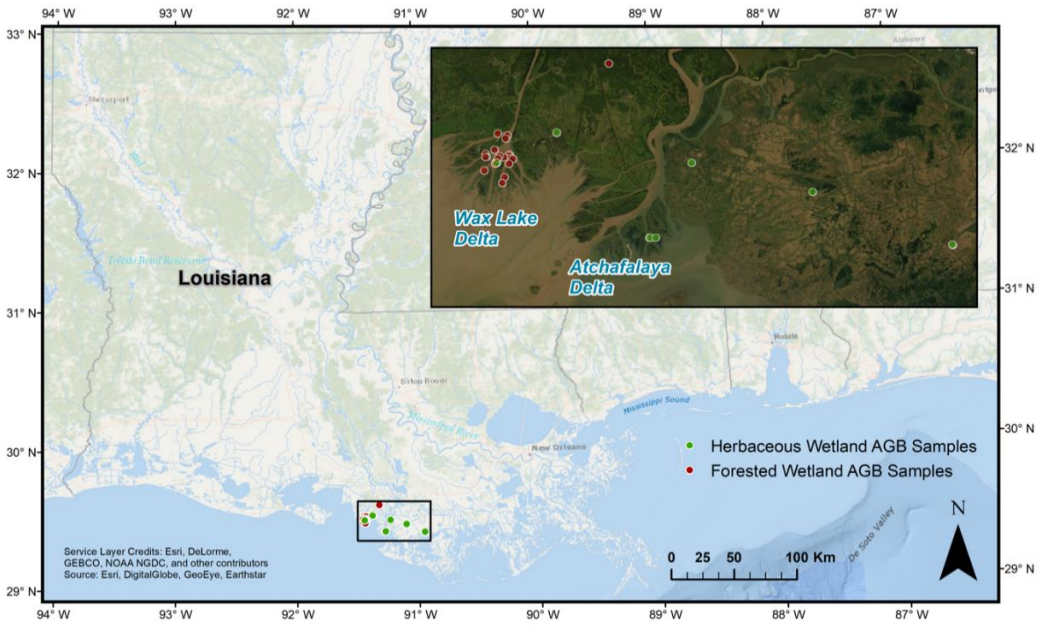


**Figure 3-1.** Study area for aboveground biomass sampling and airborne data collection. Sampling was focused on the Wax Lake Delta, with other sample sites in the Atchafalaya Delta and Terrebonne Basins to the east. Aboveground biomass (AGB) mapping was restricted to the Wax Lake Delta, though remote sensing measurements coincident with field plots extended beyond the delta for model calibration. Further AGB sample data and information is reported in Tables 3-A1 and 3-A2.

## 3.3. Materials and Methods

This study used airborne-derived reflectance spectra and SAR backscatter data, paired with coincident *in situ* AGB sample data, to develop and cross-validate a series of models based on one or both remote sensing datasets. The AGB data were primarily collected in the WLD, Louisiana, with other sample plots being located throughout the Atchafalaya and western Terrebonne Basins (Figure 3-1). The WLD is forming at the terminus of the Wax Lake Outlet, a constructed distributary channel of the Atchafalaya River, the main distributary of the Mississippi River. The outlet was constructed in 1942, diverting flow from the lower Atchafalaya River to alleviate flooding in the Morgan City area (Shlemon et al. 1975). Whereas the basins east of the Wax Lake Outlet and Atchafalaya River are severely degrading and seeing widespread wetland submergence, the WLD is an actively prograding system with accretion-driven feedbacks creating emergent deltaic floodplains (Twilley et al. 2016). Areal land growth rates in the WLD range between 1–3 $km^2$/year (Allen et al. 2012). As this artificial outlet has been allowed to build land under natural hydrologic conditions, the WLD presents an ideal case study for potential river diversion projects aimed at alleviating wetland subsidence and degradation across Louisiana's coast (Bevington et al. 2017).

### *3.3.1. Field Data*

Biomass field surveys were conducted in 2015 and 2016 to spatially coincide with imagery collected over multiple flight campaigns. Two field campaigns were conducted—one in May of 2015 and one in November of 2016—to encompass a range of biomass values across the growing season, where September is considered the peak biomass season. Fifteen sites coinciding with the May and June 2015 flight-lines (Table 3-1) were examined in the 2015 collections, six of which

were forested wetlands and nine herbaceous. Eight of the fifteen sites were located in the Wax Lake/Atchafalaya delta complex, while seven were selected in the western Terrebonne Basin. Ten out of the fifteen selected sites are part of Louisiana's Coastwide Reference Monitoring System (CRMS) (Steyer et al. 2003). One site within the WLD was examined on November 15 2016, solely for herbaceous wetland samples coinciding with the October 17, 2016, flightlines.

For the forested wetland sites (Figure 3-1; Table 3-A2), which were only examined in May 2015 given the small expected changes in annual tree growth and biomass, duplicate circular plots (10 m radius, 50 m apart) were established inside the forest approximately 30 m from the forest edge. Plots not located at CRMS sites were chosen for their accessibility within the WLD and representativeness of the immediate area. All trees with diameter at breast height (dbh, 1.3 m) ≥ 2.5 cm were measured within each plot. Species type were also registered, with *Salix nigra* being the predominant species in most plots. The height of all trees was measured with a laser range finder (Impulse 200 LR, Laser Technology Inc., Tucson, WY) and species-specific allometric equations (Jenkins et al. 2003; Jenkins et al. 2004; Chojnacky et al. 2013) were applied to estimate dry AGB. Thirty-six individual forested wetland plots within the six examined sites coincided with airborne flight-lines and were used in this study.

At herbaceous wetland sites (Figure 3-1; Table 3-A1), AGB was harvested inside duplicate plots (0.25 $m^2$, 5 m apart) at 10, 50, and 100 m along a transect established perpendicular to the wetland edge. The aboveground material in each plot was clipped at soil level, stored in plastic bags, refrigerated at 4 °C, and transported to the laboratory for further processing. Fresh plant material was sorted by species and dried at 60 °C for 72 hours before weighing to attain dry AGB ($g/m^2$). It should be noted that two of the 2016 plots were 0.49 $m^2$ and three were 0.75 $m^2$, and that two plot pairs coincided with the same pixel and were averaged together. In total, 25 herbaceous

plots coinciding with airborne flight-lines were utilized for this study, with fifteen plots collected in May 2015 and ten in November 2016.

### *3.3.2. Remote Sensing Data*

**Table 3-1.** Airborne remote sensing instrument information.

| | **Airborne Visible/Infrared Imaging Spectrometer-Next Generation (AVIRIS-NG)** | **Uninhabited Airborne Vehicle Synthetic Aperture Radar (UAVSAR)** |
|---|---|---|
| Acquisition Dates | 17 October 2016 (Mosaic, Figure 3-2);<br>6–9 May 2015; 2–6 June 2015 | 17 October 2016 (Mosaic, Figure 3);9 May 2015 |
| Aircraft Platform | B200 King Air | Gulfstream-III |
| Wavelength/ Frequency | 380-2510 nm<br>(Passive Radiance Measurements) | Fully polarimetric L-band;<br>0.2379 m/1.26 GHz<br>(Transmitted Frequency) |
| Spectral Resolution | 5 nm ± 0.5 nm | 80 MHz<br>(Chirp Bandwidth) |
| Spatial Resolution | 5.4 m | 5 m |
| Direct Model Inputs | Reflectance | Horizontally-Transmitted, Vertically-Received Backscatter |
| Derived Model Inputs | NDVI;<br>First-Derivative of Reflectance | Volume and Double Bounce Scattering Components |

#### *3.3.2.1. Imaging Spectrometer Data*

The Airborne Visible–Infrared Imaging Spectrometer-Next Generation (AVIRIS-NG) instrument measures 14-bit radiance from 380 to 2510 nm wavelengths with a ~5 nm spectral resolution (Table 3-1) (Hamlin et al. 2011; Thompson et al. 2015). AVIRIS-NG conducted five flight-lines over the WLD on October 17, 2016, producing individual datasets with 425 bands at a

5.4 m spatial resolution. These flight-lines provided the basis for mapping AGB, though we processed additional flight-lines from May and June, 2015, in order to extract pixel spectra coincident with field plots. Each raw dataset was atmospherically corrected using the physics-based Atmospheric removal (ATREM) algorithm to derive a surface reflectance image (Thompson et al. 2015; Gao et al. 1993; Bue et al. 2015). We applied the Adaptive Reflectance Geometric Correction (ARGC) algorithm to correct bidirectional reflectance distribution (BRDF) effects that cause across-track variations in observed illumination intensity (Jensen et al. 2017). With spectrally consistent surface reflectance data post-correction, we mosaicked the 2016 flight-lines and subset the resulting dataset to the WLD's extent (Figure 3-2).

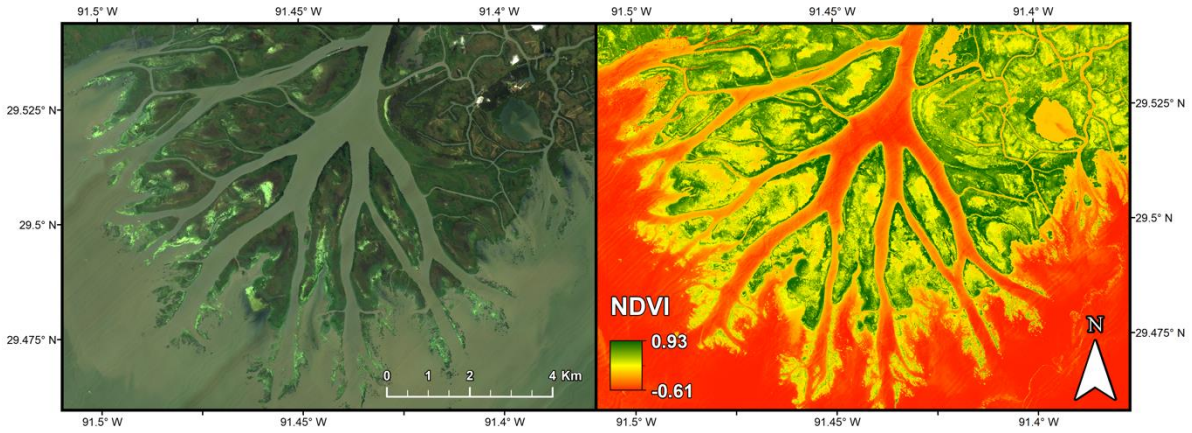


**Figure 3-2.** Imaging spectrometer data used for estimating aboveground biomass. (Left) True color composite of the Airborne Visible–Infrared Imaging Spectrometer-Next Generation (AVIRIS-NG) mosaic over the Wax Lake Delta (WLD), and (Right) normalized difference vegetation index (NDVI) calculated from AVIRIS-NG bands centered at 671.95 and 757.10 nm.

### *3.3.2.2. Synthetic Aperture Radar Data*

NASA's L-band Uninhabited Airborne Vehicle Synthetic Aperture Radar (UAVSAR) was flown concurrently with AVIRIS-NG in May 2015 and October 2016 (Table 3-1). The 2016 data, with 5 m posting, was subset to the WLD mosaic's extent and resampled to 5.4 m resolution

(Figure 3-3). The SAR signal results from different scattering mechanisms as the emitted microwaves interact with a vegetation canopy and surface before partially returning to the sensor (Klemas 2013; Hong and Wdowinski 2014). The radar signal's HV backscatter amplitude is dominated by volume scattering and has been shown to be the polarization most sensitive to AGB estimation (Sinha et al. 2015; Ramsey et al. 2014; Hamdan et al. 2014).

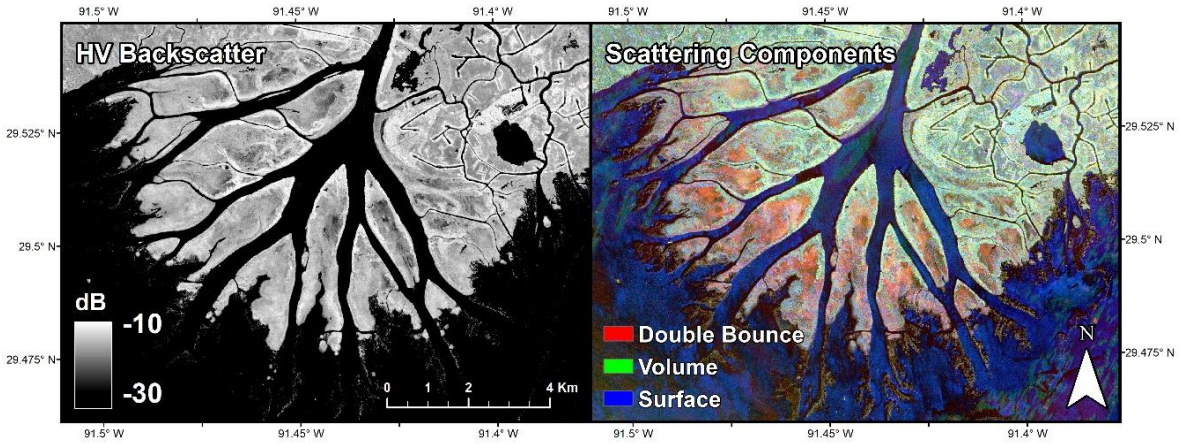


**Figure 3-3.** Synthetic aperture radar (SAR) data used for estimating aboveground biomass. (Left) Horizontally emitted, vertically received (HV) backscatter image of the 2016 Uninhabited Airborne Vehicle Synthetic Aperture Radar (UAVSAR) data over the WLD, and (Right) false color composite of the volume, double bounce, and surface scattering components from the Freeman–Durden polarimetric decomposition.

### *3.3.3. Model Development*

For each field measurement, we extracted the coincident AVIRIS-NG and UAVSAR pixel values. These data entailed surface reflectance measurements from AVIRIS-NG in addition to HV backscatter and scattering component values. These various measurements provided the basis of our modeling approach, whereby we assessed the efficacy of commonly applied univariate approaches, multivariate approaches from a single sensor, and new multivariate approaches that integrate both sensors. It should be noted that the herbaceous samples did not include submerged aquatic vegetation (SAV) or floating vegetation, which comprise a large portion of the low

intertidal and subtidal zones. These types were excised from the final mapped area, as the spectral signal from SAV is impacted by water while floating vegetation is too transient and spectrally variable for an accurate AGB prediction. For example, *Nelumbo lutea* is an emergent floating leaf vegetation that dominates the transition zone between submersed aquatic to emergent vegetation, and it is actively senescing at the time of image capture. Assessment and cross-validation of the models consequently reveals the optimal models to apply to the imagery and map AGB across the WLD.

#### *3.3.3.1. Single Sensor Ordinary Least Squares Regression Models*

Univariate regression based on a reflectance band, spectral index, or radar backscatter signal is the most common approach for remote AGB estimates (Klemas 2013; Sinha et al. 2015; Doughty and Cavanaugh 2019; Tanase et al. 2014). This is typically done by fitting a linear, logarithmic, or other polynomial function to the *in situ* AGB data and the paired remotely sensed value using ordinary least squares regression (OLSR), though machine learning algorithms are increasingly prevalent (Byrd et al. 2018). Normalized difference vegetation index (NDVI), being sensitive to vegetation's chlorophyll content and health, is the most frequently applied optical index for AGB estimation. To this end, many studies have shown NDVI to be the most effectively predictive optical index (Klemas 2013; Doughty and Cavanaugh 2019). While many studies employ NDVI such that the index values correspond to a single field collection (Cho et al. 2007), NDVI is often applied with several field collections for empirical AGB models such that it captures seasonal biomass variations (Doughty and Cavanaugh 2019). Without a full seasonal dataset, NDVI may show a significant relationship with AGB if the study area contains sufficient variance in plant tissue abundance and surface conditions (Klemas 2013). However, these measurements

may be hampered by the tendency of NDVI to saturate beyond a certain LAI (Cho et al. 2007) or in areas where soil and water may strongly influence the reflectance signal (Klemas 2013). To test the index's efficacy in relation to other approaches and data types for AGB estimation, we generated NDVI values with red and near-infrared (NIR) AVIRIS-NG bands centered at 671.95 and 757.10 nm, respectively. These are the closest AVIRIS-NG bands that correspond to the optimal wavelengths for calculating narrow-band NDVI denoted by Elvidge and Chen (1995). We then fit a linear OLS model to the resulting NDVI values and the AGB data to test whether an optical index-based approach was sufficient for estimating biomass in the spectrally and spatially complex WLD.

We implemented a similar approach with the UAVSAR imagery, whereby we fit a linear OLSR model to the HV backscatter data (Hamdan et al. 2014). Additionally, we decomposed the radar signal into the contributions of its constituent scattering mechanisms—volume, double bounce, and surface scattering—to provide a more comprehensive description of a plant area's structural properties, and thus biomass (Neumann et al. 2012; Tanase et al. 2014). We applied the Freeman-Durden polarimetric decomposition (Freeman and Durden 1998) to the UAVSAR data, producing the various scattering mechanism contributions to the observed backscatter signal (Figure 3-3). Because the surface component contains excessive noise and is not significantly impacted by vegetation structure (Neumann et al. 2012), it was not included in subsequent AGB models. Conversely, volume scattering is largely associated with attenuation and multiple reflection within vegetation canopies. The volume scattering component in the Freeman–Durden decomposition is approximated by HV backscatter (Freeman and Durden 1998). Further, corner reflection resulting from surface-trunk interaction contributes to double bounce scattering

(Neumann et al. 2012; Mougin et al. 1999). Using the volume and double bounce components, we developed bivariate OLSR models for both herbaceous and forest vegetation.

#### *3.3.3.2. Imaging Spectrometer Partial Least Squares Regression Models*

Partial least squares regression (PLSR) provides a suitable tool for leveraging the full breadth of imaging spectrometer data, as it does not rely on the statistical assumption of independence among input variables that OLSR does (Farrés et al. 2015). PLSR is instead focused on maximizing predictive capabilities, though it is prone to model overfitting (Townsend et al. 2003). As derivative spectroscopy has proven effective for hyperspectral AGB models (Byrd et al. 2014), the first derivative of reflectance was also calculated for each sample. We generated PLSR models for AGB separately for herbaceous and forest vegetation, based on both reflectances and derivatives to test the relative performance of each type. We subsequently examined the spectral characteristics each model is sensitive to.

For these reflectance and derivative models, we applied 290 of the original 425 AVIRIS-NG bands. We excised bands within the 376.44–441.55, 892.33–942.42, 1107.71–1157.79, 1353.13–1488.36, 1783.88–2024.29, and 2404.95–2500.12 nm spectral regions due to atmospheric water vapor interference. With the input spectra processed, further analysis was required to determine the PLSR models' optimal number of components. PLS components, also referred to as latent variables, are the synthetic variables in n-space that the input independent variables are projected onto. These are akin to principal components used in principal components analysis (PCA), though PLS components are developed with a weighting for the dependent variable's response (Mehmood et al. 2012; Singer et al. 2016). The PLS transformations of both the reflectance and derivative AVIRIS-NG data are shown in Figure 3-7. We then calculated the

predicted residual sum of squares (PRESS) statistic for 1–15 components (Figure 3-4). Calculating PRESS employs leave-one-out cross validation, whereby the model with the minimum summed value denotes the optimal number of components (Townsend et al. 2013; Chen et al. 2004; Singh et al. 2015). For the reflectance models, four and three components were selected for the forest and herbaceous models, respectively. It should be noted that the one-component PRESS statistic was slightly lower for the herbaceous reflectance models, though the model's $R^2$ (0.23) and mean absolute error (MAE) (103.41) were significantly inferior to the selected three-component model. Two components produced the lowest PRESS for both derivative-based models.

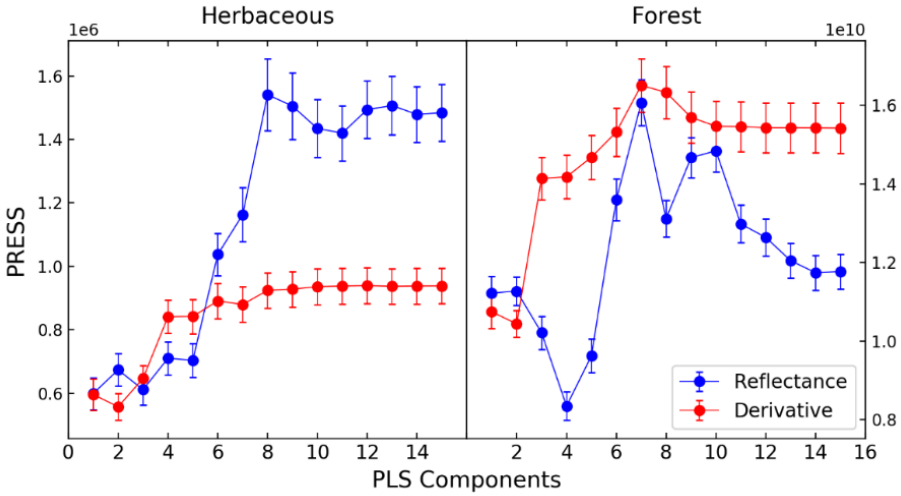


**Figure 3-4.** Predicted residual sum of squares (PRESS) statistic, calculated for 1–15 components for both reflectance and first-derivative-based models for herbaceous and forested wetlands. Error bars denote one standard deviation.

The variable importance in the projection (VIP) metric highlights the spectral domains that have the greatest bearing on the dependent variable (Farrés et al. 2015; Mehmood et al. 2012). When applied to imaging spectrometer-derivative data, the VIP response has the advantage of identifying narrow spectral features associated with the dependent variable (Jensen et al. 2019). We calculate VIP for both the herbaceous and forest derivative-based PLSR models using Equation (1):

$$VIP_i = \sqrt{p \sum_{a=1}^{A} [(q_a^2 t'_a t_a)(w_{ai}/\|w_a\|)^2] / \sum_{a=1}^{A} (q_a^2 t'_a t_a)}, \quad (7)$$

where p is the X-loading, $q_a$ is component *a*'s Y-loading, $t_a$ is its score vector, and $w_a$ is its loading weight. The loading $(w_{ai}/\|w_a\|)^2$ represents the importance of variable *i* and explains the variance in each PLS component. The $VIP_i$ weights thus measure the contribution of each variable according to that variance. We applied a moving average to smooth the VIP responses and clearly define spectral features where VIP > 1, denoting significant predictive power (Figure 3-5; Figure 3-6). By highlighting the specific spectral regions that increase predictive power, VIP aids in interpreting the biophysical characteristics that drive each PLSR model. Additionally, the biophysical information associated with each component for the different models can be viewed spatially by applying the PLS transformation to the AVIRIS-NG data (Figure 3-7).

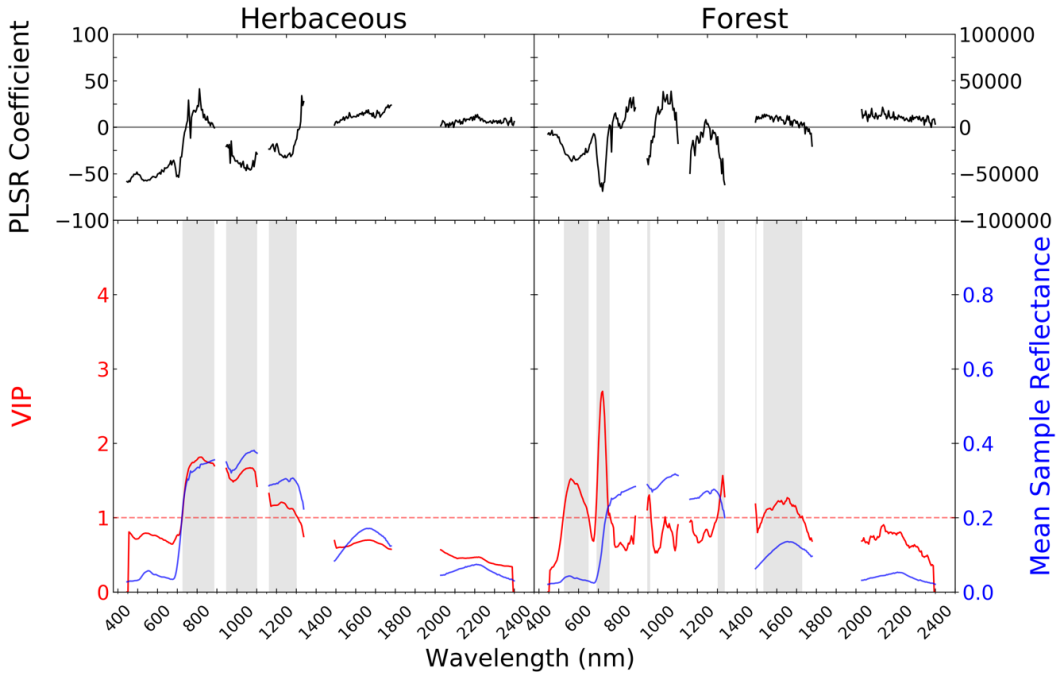


**Figure 3-5.** Reflectance-based partial least squares regression (PLSR) model results. These correspond to model 2 in Table 3-4. The model coefficients for each band are shown in black in

the top panels. In the bottom panels, variable importance in the projection (VIP) values are shown in red while average sample reflectance for either vegetation type is shown in blue. Spectral regions where VIP > 1 are highlighted in gray. Mean sample reflectance is calculated from the pixel values corresponding with each *in situ* plot and provides a reference for interpreting variable importance based on how the VIP signal aligns with spectral characteristics.

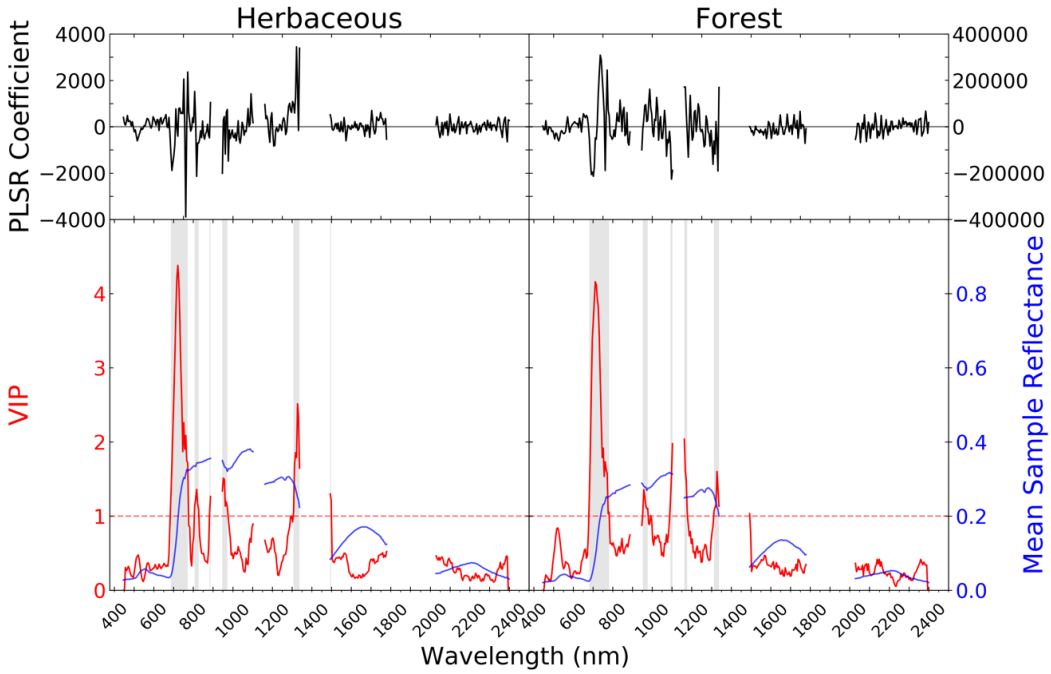


**Figure 3-6.** Derivative-based PLSR model results, corresponding to model 3 in Table 3-4.

### *3.3.3.3. Integrated Multi-sensor Models*

To determine if imaging spectrometer and SAR data beneficially complement each other for AGB estimation, we applied different variable combinations to develop optimized models integrating both datasets. We first combined the NDVI data with both the HV backscatter and the Freeman-Durden scattering components together. This allowed us to examine if a simple and easily calculable optical metric of vegetation health adds complementary information to the physical structural information provided by SAR data. However, the PLSR model inputs cannot be similarly combined with the SAR values to increase model efficacy, as we observed that the

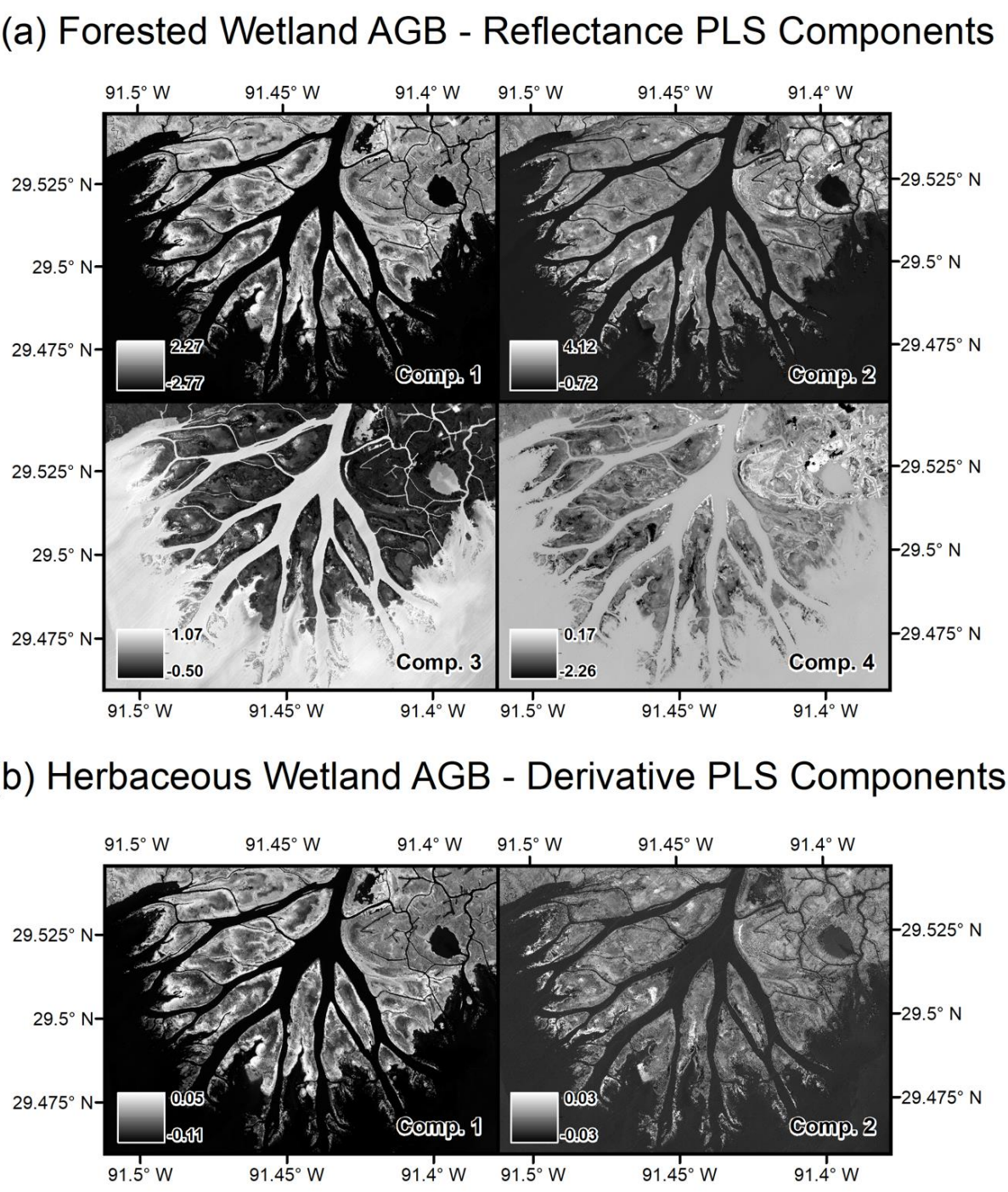


**Figure 3-7.** Partial least squares (PLS) transformations of the imaging spectrometer bands. (a) The four component responses for the PLS transformation based on the forested wetland biomass and AVIRIS-NG reflectance, and (b) the two component responses for the PLS transformation based on the herbaceous wetland biomass and AVIRIS-NG first derivative of reflectance. The greyscale and legends indicate the component loading values.

one or two extra parameters significantly degrade model results by giving inordinately high weight to the SAR variables and diminishing the spectral data's contribution. Other studies employing imaging spectroscopy for integrative AGB models rely on VIP analysis for band selection, rather than just interpretation, and so lose other bands' contributions to the AGB estimates by excising them from the final model (Laurin et al. 2004; Peerbhay et al. 2013). To assimilate the full range of VSWIR spectral information provided by imaging spectrometers into this approach, the PLSR approach must be adapted.

To modify the approach and fully integrate the two remotely sensed datasets, we extracted the PLS x-scores associated with each component—also referred to as factors (Townsend et al. 2003), latent variables or vectors (Mehmood et al. 2012; Singer et al. 2016), or bases (Sharma and Jacobs 2011)—from each model (Maitra and Yan 2008). These represent the normalized scores for the dimensionally reduced training data before each training variable is weighted with respect to the dependent variable to calculate the component loadings (Farrés et al. 2015; Mehmood et al. 2012; Delaigle and Hall 2012). Using PLS x-scores instead of PCA loading values offers more predictive capability, as the PLS components are constructed by taking information from both the independent and dependent variables into account (Sharma and Jacobs 2011). Obtaining the x-scores from the PLS decomposition and applying them separately in a regression to predict a dependent variable provides flexibility in using PLS to optimally extract orthogonal components from the independent variable dataset while avoiding restriction to the original PLS model (Maitra and Yan 2008). In doing so, the entire spectrum—for either reflectance or its derivative—associated with each AGB entry is reduced to statistically independent variables suited for combination with other data. The reflectance models were thus processed to calculate three PLS x-score values for herbaceous vegetation and four for the forested wetland models, while the

derivative models used two PLS x-scores each. The x-scores were then combined with either the HV backscatter or the paired volume and double bounce scattering values.

Our analysis resulted in a suite of models of varying complexity, each of which indicates the relative quality and importance of each input type in relation to the other variables. Uncertainty in each model was characterized by applying a leave-one-out cross validation, whereby we plotted the distribution of errors and calculated the MAE for each model. The cross-validation distribution of errors and MAE complement the model performance metrics based on calibration with all available data. The models that attained the lowest MAE, for both the initial model statistics and cross-validation, were applied to the AVIRIS-NG and UAVSAR imagery to map AGB over the Wax Lake Delta.

A classification (Figure 3-8) map was created to apply these models to their appropriate corresponding pixels. We first employed PCA to transform the 290 AVIRIS-NG reflectance bands into nine principle component bands. We then combined these bands with a LiDAR-based digital elevation model of the WLD (U.S. Geological Survey 2014) and applied an ISODATA unsupervised classification. We combined the resulting classes to reflect forested wetland vegetation, herbaceous wetland vegetation, other vegetation, and water. The other vegetation class includes SAV, *N. lutea,* and other floating vegetation types that are not suitable for the herbaceous AGB model's application. The extent of the classification map and the WLD's boundaries reflect those employed by a 2011 vegetation map (Carle et al. 2014) for consistency with established datasets. We conducted a validation survey on October 26, 2018, collecting 143 *in situ* observations along seven transects that crossed different vegetation types. With these points, we generated a confusion matrix (Table 3-2) and individual class accuracies, calculating an overall map accuracy of 95.10% (Table 3-3).

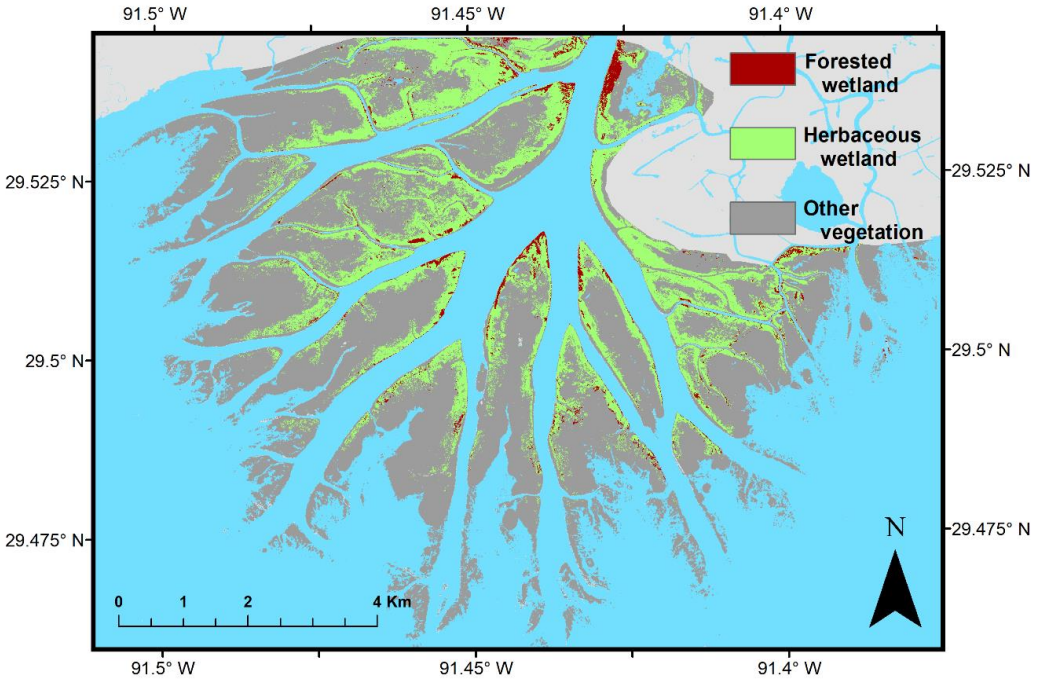


**Figure 3-8.** Classification map used to apply the aboveground biomass models. The "other vegetation" class includes *Nelumbo lutea*, floating vegetation, and submerged aquatic vegetation (SAV) and was excluded from model application.

**Table 3-2.** Classification confusion matrix.

| **Classification Data** | **Reference Data** | | | |
|---|---|---|---|---|
| | Forested wetland | Herbaceous wetland | Other vegetation | All |
| Forested wetland | **21** | 0 | 0 | 21 |
| Herbaceous wetland | 1 | **67** | 0 | 68 |
| Other vegetation | 0 | 6 | **48** | 54 |
| All | 22 | 73 | 48 | **143** |

**Table 3-3.** Classification accuracy statistics.

| | **User's Accuracy (%)** | **Producer's Accuracy (%)** |
|---|---|---|
| Forested wetland | 100.00 | 95.45 |
| Herbaceous wetland | 98.53 | 91.78 |
| Other vegetation | 88.89 | 100.00 |
| Overall accuracy | 95.10 | |
| Kappa | 0.92 | |

### 3.4. Results

All models and their corresponding numerical designation are reported in Table 3-4. The single sensor OLSR models (models 1 and 4) did not produce suitable AGB predictions, with the exception of the forest volume and double bounce scattering model (model 5) (Table 3-4). Adding NDVI to either the HV backscatter (model 6) or volume and double bounce model (model 7) only marginally increased model performances. These models did not attain appropriately low significance values, assuming a standard threshold of $p < 0.05$, for herbaceous vegetation. For the forest models, though the NDVI coupled with the Freeman–Durden components does attain a significant p-value, the performance metrics are similar to the volume and double bounce-only model.

The models that employ the full spectral response via PLS (models 2 and 3) attain superior performance metrics compared to the other models. For herbaceous vegetation, the first derivative PLSR model based only on AVIRIS-NG data performed significantly better than its reflectance counterpart. This is counter to the forest results, where the reflectance PLSR model is superior. All PLSR models, though, show high RMSE values relative to their MAEs, meaning the models do not perform well at higher AGB values. Combining the resultant PLS x-scores with the UAVSAR-derived values yields marked increases in model performance. The herbaceous models show a minor increase in $R^2$ from the standard PLSR approach when adding HV backscatter to the derivative PLS x-scores (model 9), with the Freeman–Durden components additionally producing similar results (model 11). The forest models show a more significant increase in performance when integrating the SAR data with the reflectance PLS x-scores. While adding the HV data to the PLS x-scores (model 8) yields similar results to the PLSR models, adding the volume and double bounce data (model 10) significantly increases model $R^2$ and decreases error.

**Table 3-4.** Aboveground biomass model performance statistics. Marked (*) values indicate the best performance

| | Herbaceous AGB Models (n = 25, mean = 359.24 g/m$^2$) | | | | | | Forest AGB Models (n = 36, mean = 25,555 g/m$^2$) | | | | | |
|---|---|---|---|---|---|---|---|---|---|---|---|---|
| | **PLS Comps.** | **$R^2$** | **RMSE** | **MAE** | **AIC** | **p** | **PLS Comps.** | **$R^2$** | **RMSE** | **MAE** | **AIC** | **p** |
| 1. NDVI | - | 0.08 | 150.59 | 111.38 | 325.68 | 0.18 | - | 0.08 | 16,309 | 13,033 | 805 | 0.11 |
| 2. Reflectance PLSR | 3 | 0.33 | 180.51 | 92.21 | - | - | 4 | 0.45 | 20,418 | 9,974 | - | - |
| 3. First Derivative PLSR | 2 | 0.46 | 189.62 | 81.65 | - | - | 2 | 0.35 | 19,708 | 11,260 | - | - |
| 4. HV Backscatter | - | 0.01 | 156.06 | 108.04 | 327.46 | 0.65 | - | 0.01 | 16,874 | 14,248 | 803 | 0.05 |
| 5. Volume, Double Bounce Components | - | 0.08 | 150.58 | 100.85 | 327.67 | 0.41 | - | 0.35 | 13,706 | 11,409 | 794 | <0.01 |
| 6. NDVI, HV Backscatter | - | 0.08 | 150.42 | 110.79 | 327.62 | 0.40 | - | 0.09 | 16,138 | 13,007 | 806 | 0.19 |
| 7. NDVI, Volume, Double Bounce | - | 0.23 | 137.22 | 99.91 | 325.03 | 0.13 | - | 0.38 | 13,375 | 10,972 | 794 | <0.01 |
| 8. Reflectance PLS X-Scores, HV Backscatter | 3 | 0.41 | 120.25 | 89.51 | 320.43 | 0.03 | 4 | 0.45 | 12,583 | 9,979 | 794 | <0.01 |
| 9. Derivative PLS X-Scores, HV Backscatter | 2 | 0.51 | 109.24* | 79.44 | 313.63* | <0.01 | 2 | 0.36 | 13,560 | 11,311 | 795 | <0.01 |
| 10. Reflectance PLS X-Scores, Volume, Double Bounce | 3 | 0.42 | 117.73 | 86.99 | 322.21 | 0.05 | 4 | 0.53* | 11,626* | 8,489* | 790* | <0.01 |
| 11. Derivative PLS X-Scores, Volume, Double Bounce | 2 | 0.51* | 110.10 | 77.07* | 316.02 | <0.01 | 2 | 0.48 | 12,233 | 10,066 | 790* | <0.01 |

Cross-validation of these models corroborates the compiled model performance metrics. The leave-one-out cross validation approach produced a series of error values for each model, shown as boxplot distributions in Figure 3-9. We averaged the errors for each model to calculate validation MAE values, reported in Table 3-5. The combined PLS and Freeman–Durden components models—using derivatives for herbaceous (model 11) and reflectance for forest vegetation (model 10)—produce the lowest MAE in the validation. Of the OLS models, though, model 9 attains the lowest Akaike Information Criterion (AIC) for herbaceous vegetation. Models 10 and 11 attain the lowest AIC for forested vegetation. AIC penalizes the use of additional variables to avoid overfitting, indicating the potential benefit of including extra information relative to the error reduction. Model coefficient and constant values are reported in Table A3. With the use of the PLS x-scores and Freeman–Durden components, these results reveal a marginal improvement in herbaceous AGB estimation error relative to the other models, but a substantial error reduction for forest AGB.

As the models applying PLS x-scores with the Freeman-Durden components (models 10 and 11) yielded the lowest MAEs for both the overall model using all available data (Table 3-4) and cross-validation (Table 3-5), the resultant models were selected to map AGB. The cross-validation point distributions for these models are shown in Figure 3-10. The derivative-based model was applied to herbaceous pixels in the AVIRIS-NG and UAVSAR products. The same process was performed on forest pixels using the reflectance PLS x-scores, volume, and double bounce model. Combined with the classification map of WLD herbaceous and forested wetland vegetation generated from the AVIRIS-NG data (Figure 3-8), the models produced the AGB map in Figure 3-11.


**Figure 3-9.** Distribution of aboveground biomass model leave-one-out cross-validation errors. The circles, or "fliers," represent outliers. Models 1 (NDVI) and 6 (NDVI, HV Backscatter) are excluded as performance was not significant ($p < 0.05$) for either herbaceous or forested vegetation.

**Table 3-5.** Mean absolute error results from cross-validation for applicable models.

| | **Herbaceous MAE ($g/m^2$)** | **Forest MAE ($g/m^2$)** |
|---|---|---|
| 2. Reflectance PLSR | 112.57 | 12,061 |
| 3. First derivative PLSR | 110.05 | 14,192 |
| 4. HV backscatter | 114.71 | 16,481 |
| 5. Volume, double bounce components | 111.71 | 12,477 |
| 7. NDVI, volume, double bounce components | 118.35 | 12,040 |
| 8. Reflectance PLS X-scores, HV backscatter | 114.67 | 12,346 |
| 9. Derivative PLS X-scores, HV backscatter | 110.47 | 14,345 |
| 10. Reflectance PLS X-scores, volume, double bounce | 114.43 | 11,060* |
| 11. Derivative PLS X-scores, volume, double bounce | 106.38* | 12,950 |

*Marked values indicate the lowest MAE results, and thus the selected models. Models 1 (NDVI) and 6 (NDVI, HV Backscatter) are excluded as performance was not significant ($p < 0.05$) for either herbaceous or forested vegetation.

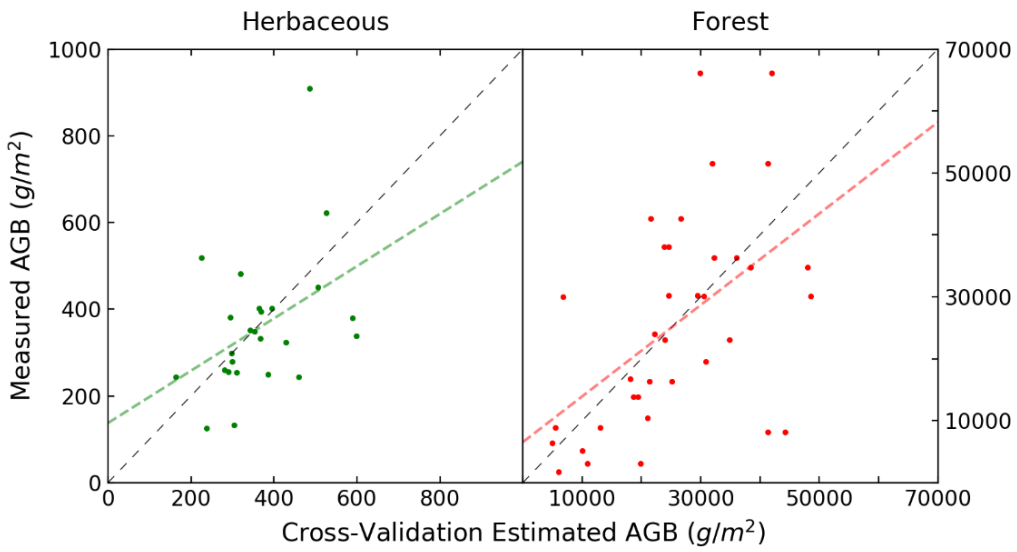


**Figure 3-10.** Point distribution of cross-validation predictions vs. sample values. Calculated for the herbaceous (model 11) and forest (model 10) models using the PLS x-scores and Freeman-Durden components. The black dashed lines represent the 1:1 line while the green and red dashed lines represent the lines of best fit for the cross-validation predictions, and thus the potential model biases.

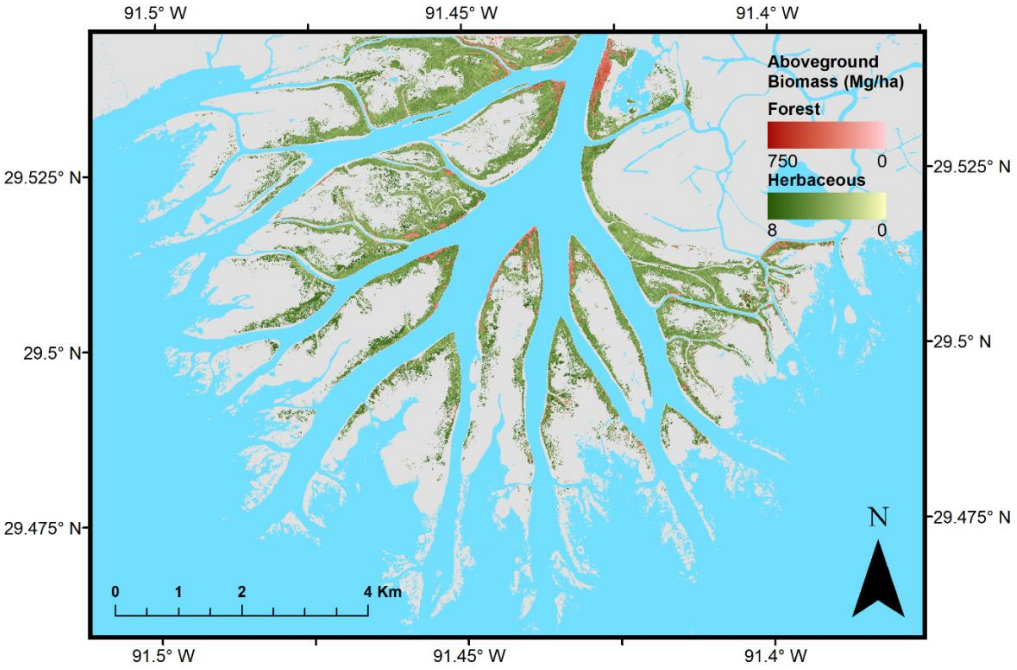


**Figure 3-11.** Estimated wetland aboveground biomass (Mg/ha) map of the Wax Lake Delta. The gray area represents *N. lutea*, floating vegetation, and submerged aquatic vegetation that was not included in this analysis.

### 3.5. Discussion

The VIP response calculated simultaneously with the PLSR models offers insight into the spectral properties inherent to each model. Using a threshold of VIP > 1, Figures 3-5 and 3-6 highlight the spectral domains that most increase the reflectance and derivative PLSR models' respective predictive capacity. The herbaceous reflectance model is particularly sensitive to the NIR domain, while the forest reflectance model is sensitive to the visible, red edge, parts of the NIR, and SWIR 1 (1493.37-1778.87 nm) domains. For the forest reflectance model, the visible, red edge, and NIR bands associated with high VIP correspond with negative model coefficients, though much of the NIR domain exhibits positive coefficients and VIP values close to one. Turgid leaves, i.e., the leaf canopy, is associated with visible absorption (with relatively higher green reflectance) and NIR reflectance (Asner 1998). Thus, the importance of these bands indicates that greater scattering from leaves is closely associated with greater forest biomass. The SWIR 1 region also exhibits high VIP values and positive coefficients. This spectral domain responds to non-photosynthetic vegetation (NPV), such that woody stems show low reflectance variation relative to the NIR domain (Asner 1998; Govender et al. 2009). The observed significance and positive coefficient values across the SWIR 1 domain likely indicate that more observed NPV material is associated with higher tree biomass. It is likely that this is due to lower canopy closure and leaf content being observed by AVIRIS-NG.

Conversely, the derivative-based PLSR models are attuned to specific spectral features' characteristics. Both the herbaceous and forest PLSR model VIP scores depict a significant response to the red edge region (Figure 3-6), for which the steepness and magnitude are strongly associated with red-absorbing chlorophyll and other pigments (Govender et al. 2009; Blackburn 1998; Blackburn 1999). The other important regions in both models represent spectral features

whose depth and curvature are associated with leaf water content (Govender et al. 2009; Lelong et al. 1998; Champagne 2003). It should be noted that the herbaceous derivative PLSR model quantifies a narrow feature at approximately 810–820 nm as important (Figure 3-6). It is unclear whether this feature is an artifact of the minor water vapor absorption lines from 813 to 820 (Ponsardin and Browell 1997), or whether it is correlated with a particular biophysical property in the herbaceous canopy (Ollinger 2010). For example, narrowband reflectance at 810 nm has been applied for estimating chlorophyll content (Blackburn 1998; Gitelson and Merzlyak 1996), water stress (Govender et al. 2009), nutrient (nitrogen, phosphorous, potassium)-related stress (Jørgensen et al. 2007), and photosynthetic rate (Tian et al. 2005). Additionally, reflectance at 820 nm has been incorporated in indices for detecting plant water stress (Lelong et al. 1998) or leaf water content while accounting for chlorophyll concentrations and structural properties (Ceccato et al. 2001). Given the water vapor absorption feature here and the numerous studies that use its wavelength range for detecting plant stress, the spectral response may be affected by the canopy liquid water features—which correlates with biomass—in turn affecting atmospheric reflectance estimates. Whereas the reflectance-based models describe biomass as a function of canopy cover, the first-derivative of the reflectance spectra train the models on chlorophyll and water absorption features. In forested wetlands where reflectance is the superior predictor, leaf abundance and woody NPV appear to be most closely associated with AGB. For herbaceous vegetation, water content appears to be most closely related to AGB.

For each of these PLSR models, the PLS x-scores values entail the essential information, though not the full weighted projection for each input band. Carrying the PLS x-scores forward into the integrated OLSR models complements the biochemical information inherent in the spectra with the structural information in the SAR data. For these data, model results including $R^2$, error

metrics, and AIC values (Table 3-4) indicate that full spectral responses are more effective at estimating AGB than standard vegetation indices. With respect to optical remote sensing generally, this supports the superior efficacy of imaging spectrometers over multispectral instruments. It is important to determine whether these optical data, being sensitive to vegetation biochemical information, aptly complement the information provided by the interaction of radar signals with plant structure.

The HV backscatter data from UAVSAR alone shows no significant relationship with AGB in either plant type in this assessment, though this parameter has proven effective in other AGB retrievals (Neumann et al. 2012; Hamdan et al. 2014; Mougin et al. 1999). It should be noted that HV backscatter constitutes the volume scattering component in the Freeman–Durden algorithm (Freeman and Durden 1998). When the Freeman–Durden polarimetric decomposition is applied to the UAVSAR data, though, the scattering components together in forested wetlands show a weak but significant ($R^2 = 0.35$, $p < 0.01$) relationship with AGB. On the contrary, the volume and double bounce scattering model remains insignificant for herbaceous vegetation—on par with the HV backscatter model. As HV backscatter is essentially equal to the volume scattering, any improvement from the addition of the double bounce component is due to the quantification of corner reflection and its interaction with the volume scattering variable. From this we can conclude that the polarimetric decomposition significantly increases AGB estimation capability for forest vegetation but not for herbaceous vegetation, as the volume and double bounce scattering components are controlled by plant structures (i.e., leaf canopy and tree trunks) that are more differentiated among trees.

A similar pattern is manifest in the combination of the SAR data with the PLS x-scores. Adding NDVI to any of the SAR-dominated models does not add any significant explanatory

power, though the PLS x-scores combined with SAR data increase performance across the board. NDVI, showing little explanatory power alone or with other variables, here represents a standard multispectral application and the first step in a series of increasingly complicated empirical models. For herbaceous vegetation, HV backscatter with the PLS x-scores produces the lowest AIC, which quantifies model quality in terms of accuracy, variable explanatory power, and model simplicity. However, the PLS x-scores combined with the Freeman–Durden components produced the lowest model (Table 3-4) and cross-validation (Table 3-5) error values. Whereas the lower error is desirable for maximizing AGB estimation accuracy, the marginal increase in performance with the polarimetric decomposition may be less preferable than a simpler model requiring less data processing in studies looking solely at herbaceous vegetation. The forested wetland vegetation, though, shows a significant decrease in error with the inclusion of the Freeman–Durden components. Coupling the PLS x-scores with the scattering components here produces a significant reduction in cross-validation error as well as the lowest AIC value. We conclude that while the polarimetric decomposition only slightly increases herbaceous AGB estimation accuracy when paired with imaging spectrometer data, it enables a significant increase in model performance for forested vegetation.

Lastly, we provide AGB estimates for the study domain over the WLD. 9.92 $km^2$ of herbaceous emergent vegetation was mapped, over which we calculated a mean AGB of 3.58 Mg/ha and a total of 3551.31 Mg. For the 0.93 $km^2$ of forested wetland vegetation, we estimated a mean AGB of 294.78 Mg/ha and a total of 27,499.14 Mg.

Other studies have assessed AGB in the broader MDP (Thomas et al. 2019; Byrd et al. 2018), including the Atchafalaya basin, though these studies employ coarser satellite data that is not as well suited for local-scale sites such as the WLD. For example, Byrd et al. (2018) use

Landsat and Sentinel-1 data to model herbaceous marsh biomass in seven coastal wetland regions throughout the conterminous United States, of which the MDP is one. An expansive *in situ* dataset was paired with six Landsat indices in a random forest model to estimate AGB, and subsequently uses an average percent carbon value of 44.1% to calculate an average carbon concentration of 1.85 Mg/ha in coastal Louisiana. This yields a mean herbaceous AGB value of 4.20 Mg/ha throughout the greater MDP, higher than this study's predicted average. This may be due to the study's use of coarser Landsat data, whose larger pixels likely mixed some forested wetlands with the herbaceous cover. Further, the study (Byrd et al. 2018) is not limited to emergent vegetation and includes the deltaic island interiors (i.e., interdistributary bays) where floating vegetation is prominent, which may appear very bright in optical data (Figure 3-1) and lead to erroneous higher AGB estimates. In addition, Thomas et al. (2019) use an *in situ* AGB dataset for both herbaceous and forested wetland vegetation in the study area, which overlaps with the data used in this study, reporting a mean sample AGB density of 3.82 Mg/ha for herbaceous wetlands and 227.02 Mg/ha for forested wetlands in May of 2015. Thomas et al. (2019), however, could not devise a robust model from coincident Sentinel-1 and Sentinel-2 data with the number of field sites available. This corroborates this study's poor results from NDVI and HV backscatter-only models, which represent standard multispectral and backscatter methods typically employed with widely available satellite data products. This further indicates that imaging spectrometers, especially in combination with SAR, have greater potential for AGB estimation than currently available multispectral instruments. Our lower herbaceous AGB estimates compared to these studies (Byrd et al. 2018; Thomas et al. 2019) are likely due to the more limited dataset not including many of the higher biomass samples from the peak growing season in September as they were not coincident with remotely sensed imagery. Additionally, with the October flight campaign being

just after the peak biomass period, some of the herbaceous species had started to senesce, likely resulting in lower AGB estimates. Unlike these studies (Byrd et al. 2018; Thomas et al. 2019), where coarser satellite-based data is used to map vegetation, here we employ high-resolution remote sensing data to map AGB at a local scale. This enables our estimates to be used in future studies concerning AGB's relationships with elevation, age, and species.

### 3.6. Conclusion

This study integrated airborne imaging spectrometer and SAR data for estimating wetland vegetation AGB, and in doing so showed that these distinct datasets complement each other and enable more accurate models than either sensor alone. Additionally, the full spectral response provided by the imaging spectrometer was shown to be superior to standard univariate vegetation index approaches for AGB estimation. Building on this, we found that the first derivative of reflectance is superior to reflectance itself for estimating AGB in herbaceous vegetation, though the converse holds true for forested vegetation. This is due to the detected spectral regions most closely associated with AGB in our models, which predominately relate to chlorophyll and water content in herbaceous vegetation as well as leaf abundance and NPV in forested wetlands. Similarly, the use of a polarimetric decomposition for the SAR data increases the models' effectiveness relative to standard backscatter, and this increase is larger for forested vegetation than for herbaceous due to greater structural diversity. These factors lead the integrated multi-sensor models to attain superior accuracies. High resolution imaging spectrometer data is shown here to be an effective tool for modeling and mapping AGB when integrating the structural information provided by SAR. Our approach and local AGB estimates, which are lower on average

than other remote sensing studies in coastal Louisiana (Byrd et al. 2018; Thomas et al. 2019), are suited for further study of AGB's ecological role in deltaic emergent wetland development.

Our methods and findings bear significance for future studies and Earth-observing satellite missions. Further study should incorporate more herbaceous and forested wetland AGB data coincident with field spectrometer/imaging spectrometer and SAR data collections. In doing so, the spectral characteristics associated with AGB across different vegetation types may be more accurately quantified and a transferable algorithm for emergent wetland vegetation may be developed. Our analysis provides an assessment of capabilities for two upcoming spaceborne missions: the NASA ISRO Synthetic Aperture Radar (NISAR), an L-band sensor partly designed to estimate biomass, and the Surface Biology and Geology (SBG) mission that will provide frequent and global hyperspectral data akin to AVIRIS-NG. Our methods show the benefit of leveraging and integrating imaging spectrometer and radar data to estimate wetland vegetation biomass.

### 3.7. References

Adam, Elhadi, Onisimo Mutanga, and Denis Rugege. 2010. "Multispectral and Hyperspectral Remote Sensing for Identification and Mapping of Wetland Vegetation: A Review." *Wetlands Ecology and Management* 18 (3): 281–96.

Allen, Yvonne C., Brady R. Couvillion, and John A. Barras. 2012. "Using Multitemporal Remote Sensing Imagery and Inundation Measures to Improve Land Change Estimates in Coastal Wetlands." *Estuaries and Coasts* 35 (1): 190–200.

Asner, Gregory P. 1998. "Biophysical and Biochemical Sources of Variability in Canopy Reflectance." *Remote Sensing of Environment* 64 (3): 234–53.

Bevington, Azure E., Robert R. Twilley, Charles E. Sasser, and Guerry O. Holm. 2017.

"Contribution of River Floods, Hurricanes, and Cold Fronts to Elevation Change in a Deltaic Floodplain, Northern Gulf of Mexico, USA." *Estuarine, Coastal and Shelf Science* 191: 188–200.

Blackburn, George A. 1999. "Relationships between Spectral Reflectance and Pigment Concentrations in Stacks of Deciduous Broadleaves." *Remote Sensing of Environment* 70 (2): 224–37.

Blackburn, George, and A. 1998. "Spectral Indices for Estimating Photosynthetic Pigment Concentrations: A Test Using Senescent Tree Leaves." *International Journal of Remote Sensing* 19 (4): 657–75.

Bue, Brian D., David R. Thompson, Michael Eastwood, Robert O. Green, Bo Cai Gao, Didier Keymeulen, Charles M. Sarture, Alan S. Mazer, and Huy H. Luong. 2015. "Real-Time Atmospheric Correction of AVIRIS-NG Imagery." *IEEE Transactions on Geoscience and Remote Sensing* 53 (12): 6419–28.

Byrd, Kristin B., Laurel Ballanti, Nathan Thomas, Dung Nguyen, James R. Holmquist, Marc Simard, and Lisamarie Windham-Myers. 2018. "A Remote Sensing-Based Model of Tidal Marsh Aboveground Carbon Stocks for the Conterminous United States." *ISPRS Journal of Photogrammetry and Remote Sensing* 139: 255–71.

Byrd, Kristin B., Laurel Ballanti, Nathan Thomas, James R. Holmquist, Marc Simard, Lisa Windham-Myers. "Aboveground Biomass High-Resolution Maps for Selected US Tidal Marshes, 2015." 2018. ORNL DAAC, Oak Ridge, TN, USA.

Byrd, Kristin B., Jessica L. O'Connell, Stefania Di Tommaso, and Maggi Kelly. 2014. "Evaluation of Sensor Types and Environmental Controls on Mapping Biomass of Coastal Marsh Emergent Vegetation." *Remote Sensing of Environment* 149: 166–80.

Carle, Melissa V., Lei Wang, and Charles E. Sasser. 2014. “Mapping Freshwater Marsh Species Distributions Using WorldView-2 High-Resolution Multispectral Satellite Imagery.” *International Journal of Remote Sensing* 35 (13): 4698–4716.

Ceccato, Pietro, Stéphane Flasse, Stefano Tarantola, Stéphane Jacquemoud, and Jean Marie Grégoire. 2001. “Detecting Vegetation Leaf Water Content Using Reflectance in the Optical Domain.” *Remote Sensing of Environment* 77 (1): 22–33.

Champagne, Catherine M., Karl Staenz, Abdou Bannari, Heather McNairn, and Jean Claude Deguise. 2003. “Validation of a Hyperspectral Curve-Fitting Model for the Estimation of Plant Water Content of Agricultural Canopies.” *Remote Sensing of Environment* 87 (2–3): 148–60.

Chen, Sheng, Xia Hong, Chris J. Harris, and Paul M. Sharkey. 2004. “Sparse Modeling Using Orthogonal Forward Regression With PRESS Statistic and Regularization.” *IEEE Transactions on Systems, Man, and Cybernetics, Part B: Cybernetics* 34 (2): 898–911.

Cho, Moses Azong, Andrew Skidmore, Fabio Corsi, Sipke E. van Wieren, and Istiak Sobhan. 2007. “Estimation of Green Grass/Herb Biomass from Airborne Hyperspectral Imagery Using Spectral Indices and Partial Least Squares Regression.” *International Journal of Applied Earth Observation and Geoinformation* 9 (4): 414–24.

Chojnacky, David C., Linda S. Heath, and Jennifer C. Jenkins. 2013. “Updated Generalized Biomass Equations for North American Tree Species.” *Forestry* 87 (1): 129–51.

Couvillion, Brady R., Holly Beck, Donald Schoolmaster, and Michelle Fischer. 2017. “Land Area Change in Coastal Louisiana (1932 to 2010) Map 3381.”

Craft, Christopher, Jonathan Clough, Jeff Ehman, Samantha Jove, Richard Park, Steve Pennings,

Hongyu Guo, and Megan Machmuller. 2009. “Forecasting the Effects of Accelerated Sea-Level Rise on Tidal Marsh Ecosystem Services.” *Frontiers in Ecology and the Environment* 7 (2): 73–78.

Delaigle, Aurore, and Peter Hall. 2012. “Methodology and Theory for Partial Least Squares Applied to Functional Data.” *Annals of Statistics* 40 (1): 322–52.

Doughty, Cheryl L., and Kyle C. Cavanaugh. 2019. “Mapping Coastal Wetland Biomass from High Resolution Unmanned Aerial Vehicle (UAV) Imagery.” *Remote Sensing* 11 (5).

Elvidge, Christopher D., and Zhikang Chen. 1995. “Comparison of Broad-Band and Narrow-Band Red and near-Infrared Vegetation Indices.” *Remote Sensing of Environment* 54 (1): 38–48.

Farrés, Mireia, Stefan Platikanov, Stefan Tsakovski, and Roma Tauler. 2015. “Comparison of the Variable Importance in Projection (VIP) and of the Selectivity Ratio (SR) Methods for Variable Selection and Interpretation.” *Journal of Chemometrics* 29 (10): 528–36.

Freeman, Anthony, and Stephen L. Durden. 1998. “A Three-Component Scattering Model for Polarimetric SAR Data.” *IEEE Transactions on Geoscience and Remote Sensing* 36 (3): 963–73.

Gao, Bo Cai, Kathleen B. Heidebrecht, and Alexander F.H. Goetz. 1993. “Derivation of Scaled Surface Reflectances from AVIRIS Data.” *Remote Sensing of Environment* 44 (2–3): 165–78.

Gitelson, Anatoly A., and Mark N. Merzlyak. 1996. “Signature Analysis of Leaf Reflectance Spectra: Algorithm Development for Remote Sensing of Chlorophyll.” *Journal of Plant Physiology* 148 (3–4): 494–500.

Govender, M., P. J. Govender, I. M. Weiersbye, E.T. F. Witkowski, and F. Ahmed. 2009.

"Review of Commonly Used Remote Sensing and Ground-Based Technologies to Measure Plant Water Stress." *Water SA* 35 (5): 741–52.

Hamdan, O., H. Khali Aziz, and I. Mohd Hasmadi. 2014. "L-Band ALOS PALSAR for Biomass Estimation of Matang Mangroves, Malaysia." *Remote Sensing of Environment* 155 (May): 69–78.

Hamlin, L., R. O. Green, P. Mouroulis, M. Eastwood, D. Wilson, M. Dudik, and C. Paine. 2011. "Imaging Spectrometer Science Measurements for Terrestrial Ecology: AVIRIS and New Developments." *IEEE Aerospace Conference Proceedings*, 1–8.

Henderson, Floyd M., and Anthony J. Lewis. 2008. "Radar Detection of Wetland Ecosystems: A Review." *International Journal of Remote Sensing* 29 (20): 5809–35.

Hong, Sang Hoon, and Shimon Wdowinski. 2014. "Double-Bounce Component in Cross-Polarimetric SAR from a New Scattering Target Decomposition." *IEEE Transactions on Geoscience and Remote Sensing* 52 (6): 3039–51.

Jenkins, Jennifer C, David C Chojnacky, Linda S Heath, and Richard A Birdsey. 2004. "Comprehensive Database of Diameter-Based Biomass Regressions for North American Tree Species." Newtown Square, PA.

Jenkins, Jennifer C., David C. Chojnacky, Linda S. Heath, and Richard A. Birdsey. 2003. "National-Scale Biomass Estimators for United States Tree Species." *Forest Science* 49 (1): 12–35.

Jensen, Daniel J., Marc Simard, Kyle C. Cavanaugh, and David R. Thompson. 2017. "Imaging Spectroscopy BRDF Correction for Mapping Louisiana's Coastal Ecosystems." *IEEE Transactions on Geoscience and Remote Sensing* 56 (3): 1739–48.

Jensen, Daniel, Marc Simard, Kyle Cavanaugh, Yongwei Sheng, Cédric G. Fichot, Tamlin

Pavelsky, and Robert Twilley. 2019. “Improving the Transferability of Suspended Solid Estimation in Wetland and Deltaic Waters with an Empirical Hyperspectral Approach.” *Remote Sensing* 11 (1629).

Jørgensen, R. N., L. K. Christensen, and R. Bro. 2007. “Spectral Reflectance at Sub-Leaf Scale Including the Spatial Distribution Discriminating NPK Stress Characteristics in Barley Using Multiway Partial Least Squares Regression.” *International Journal of Remote Sensing* 28 (5): 943–62.

Kirwan, Matthew L., and Glenn R. Guntenspergen. 2010. “Influence of Tidal Range on the Stability of Coastal Marshland.” *Journal of Geophysical Research* 115 (F2): 1–11.

Klemas, Victor. 2013. “Remote Sensing of Coastal Wetland Biomass: An Overview.” *Journal of Coastal Research* 290: 1016–28.

Laurin, Gaia V., Qi Chen, Jeremy A. Lindsell, David A. Coomes, Fabio Del Frate, Leila Guerriero, Francesco Pirotti, and Riccardo Valentini. 2014. “Above Ground Biomass Estimation in an African Tropical Forest with Lidar and Hyperspectral Data.” *ISPRS Journal of Photogrammetry and Remote Sensing* 89: 49–58.

Lelong, Camille C.D, Patrick C Pinet, and Hervé Poilvé. 1998. “Hyperspectral Imaging and Stress Mapping in Agriculture.” *Remote Sensing of Environment* 66 (2): 179–91.

Li, X., A. Gar-On Yeh, S. Wang, K. Liu, X. Liu, J. Qian, and X. Chen. 2007. “Regression and Analytical Models for Estimating Mangrove Wetland Biomass in South China Using Radarsat Images.” *International Journal of Remote Sensing* 28 (24): 5567–82.

Maitra, Saikat, and Jun Yan. 2008. “Principle Component Analysis and Partial Least Squares: Two Dimension Reduction Techniques for Regression.” In *Applying Multivariate Statistical Models*, 79th ed., 79–90.

Manninen, Terhikki, Pauline Stenberg, Miina Rautiainen, Pekka Voipio, and Heikki Smolander. 2005. “Leaf Area Index Estimation of Boreal Forest Using ENVISAT ASAR.” *IEEE Transactions on Geoscience and Remote Sensing* 43 (11): 2627–35.

Mehmood, Tahir, Kristian Hovde Liland, Lars Snipen, and Solve Sæbø. 2012. “A Review of Variable Selection Methods in Partial Least Squares Regression.” *Chemometrics and Intelligent Laboratory Systems* 118 (September 2017): 62–69.

Mohammadimanesh, Fariba, Bahram Salehi, Masoud Mahdianpari, Brian Brisco, and Mahdi Motagh. 2018. “Wetland Water Level Monitoring Using Interferometric Synthetic Aperture Radar (InSAR): A Review.” *Canadian Journal of Remote Sensing* 44 (4): 247–62.

Morris, James T., P. V. Sundareshwar, Christopher T. Nietch, Björn Kjerfve, and D. R. Cahoon. 2002. “Responses of Coastal Wetlands to Rising Sea Level.” *Ecology* 83 (10): 2869–77.

Mougin, E., C. Proisy, G. Marty, F. Fromard, H. Puig, J.L. Betoulle, and J.P. Rudant. 1999. “Multifrequency and Multipolarization Radar Backscattering from Mangrove Forests.” *IEEE Transactions on Geoscience and Remote Sensing* 37 (1): 94–102.

Mudd, Simon M., Susan M. Howell, and James T. Morris. 2009. “Impact of Dynamic Feedbacks between Sedimentation, Sea-Level Rise, and Biomass Production on near-Surface Marsh Stratigraphy and Carbon Accumulation.” *Estuarine, Coastal and Shelf Science* 82 (3): 377–89.

Neumann, Maxim, Sassan S. Saatchi, Lars M.H. Ulander, and Johan E.S. Fransson. 2012. “Assessing Performance of L- and P-Band Polarimetric Interferometric SAR Data in Estimating Boreal Forest above-Ground Biomass.” *IEEE Transactions on Geoscience and Remote Sensing* 50 (3): 714–26.

Ollinger, S. V. 2010. “Sources of Variability in Canopy Reflectance and the Convergent Properties of Plants.” *New Phytologist* 189: 375–94.

Peerbhay, Kabir Yunus, Onisimo Mutanga, and Riyad Ismail. 2013. “Commercial Tree Species Discrimination Using Airborne AISA Eagle Hyperspectral Imagery and Partial Least Squares Discriminant Analysis (PLS-DA) in KwaZulu-Natal, South Africa.” *ISPRS Journal of Photogrammetry and Remote Sensing* 79: 19–28.

Ponsardin, Patrick L., and Edward V. Browell. 1997. “Measurements of H216O Linestrengths and Air-Induced Broadenings and Shifts in the 815-Nm Spectral Region.” *Journal of Molecular Spectroscopy* 185 (1): 58–70.

Ramsey, Elijah, Amina Rangoonwala, Zhaohui Chi, Cathleen E. Jones, and Terri Bannister. 2014. “Marsh Dieback, Loss, and Recovery Mapped with Satellite Optical, Airborne Polarimetric Radar, and Field Data.” *Remote Sensing of Environment* 152: 364–74.

Ramsey, Elijah, Amina Rangoonwala, and Cathleen E. Jones. 2015. “Structural Classification of Marshes with Polarimetric SAR Highlighting the Temporal Mapping of Marshes Exposed to Oil.” *Remote Sensing* 7 (9): 11295–321.

Rosen, P A, S Hensley, I R Joughin, F K Li, S N Madsen, E Rodriguez, and R M Goldstein. 2000. “Synthetic Aperture Radar Interferometry.” *Proceedings of the IEEE* 88 (3): 333–82.

Rouse, J. W., R. H. Hass, J.A. Schell, and D.W. Deering. 1973. “Monitoring Vegetation Systems in the Great Plains with ERTS.” In *Third Earth Resources Technology Satellite (ERTS) Symposium*, 1:309–17.

Schile, Lisa M., John C. Callaway, James T. Morris, Diana Stralberg, V. Thomas Parker, and

Maggi Kelly. 2014. “Modeling Tidal Marsh Distribution with Sea-Level Rise: Evaluating the Role of Vegetation, Sediment, and Upland Habitat in Marsh Resiliency.” *PLoS ONE* 9 (2).

Sharma, Abhishek, and David W. Jacobs. 2011. “Bypassing Synthesis: PLS for Face Recognition with Pose, Low-Resolution and Sketch.” *Proceedings of the IEEE Computer Society Conference on Computer Vision and Pattern Recognition*, 593–600.

Shlemon, R.J. 1975. “Subaqueous Delta Formation-Atchafalaya Bay, Louisiana.” In *Deltas: Models for Exploration*, edited by Martha Lou Broussard, 209–21. Houston, TX: Houston Geological Society.

Singer, Marco, Tatyana Krivobokova, Axel Munk, and Bert De Groot. 2016. “Partial Least Squares for Dependent Data.” *Biometrika* 103 (2): 351–62.

Singh, Aditya, Shawn P. Serbin, Brenden E. McNeil, Clayton C. Kingdon, and Philip A. Townsend. 2015. “Imaging Spectroscopy Algorithms for Mapping Canopy Foliar Chemical and Morphological Traits and Their Uncertainties.” *Ecological Applications* 25 (8): 2180–97.

Sinha, S., C. Jeganathan, L. K. Sharma, and M. S. Nathawat. 2015. “A Review of Radar Remote Sensing for Biomass Estimation.” *International Journal of Environmental Science and Technology* 12 (5): 1779–92.

Steyer, Gregory D., Charles E. Sasser, Jenneke M. Visser, Erick M. Swenson, John A. Nyman, and Richard C. Raynie. 2003. “A Proposed Coast-Wide Reference Monitoring System for Evaluating Wetland Restoration Trajectories in Louisiana.” *Environmental Monitoring and Assessment* 81: 107–17.

Tanase, Mihai A., Rocco Panciera, Kim Lowell, Siyuan Tian, Jorg M. Hacker, and Jeffrey P.

Walker. 2014. “Airborne Multi-Temporal L-Band Polarimetric SAR Data for Biomass Estimation in Semi-Arid Forests.” *Remote Sensing of Environment* 145: 93–104.

Thomas, Nathan, Marc Simard, Edward Cateñeda-Moya, Kristin Byrd, Lisamaria Windham-Myers, Azure Bevington, and Robert R. Twilley. 2019. “High-Resolution Mapping of Biomass and Distribution of Marsh and Forested Wetlands in Southeastern Coastal Louisiana.” *International Journal of Applied Earth Observation and Geoinformation* 80 (December 2018): 257–67.

Thompson, David R., Bo Cai Gao, Robert O. Green, Dar A. Roberts, Philip E. Dennison, and Sarah R. Lundeen. 2015. “Atmospheric Correction for Global Mapping Spectroscopy: ATREM Advances for the HyspIRI Preparatory Campaign.” *Remote Sensing of Environment* 167: 64–77.

Tian, Y., Y. Zhu, and W. Cao. 2005. “Monitoring Leaf Photosynthesis with Canopy Spectral Reflectance in Rice.” *Photosynthetica* 43 (4): 481–89.

Townsend, P A, J R Foster, R A Chastian Jr, and W S Currie. 2003. “Canopy Nitrogen in the Forests of the Central Appalachian Mountains Using Hyperion and AVIRIS.” *IEEE Transactions on Geoscience and Remote Sensing* 41 (6): 1347–54.

Townsend, P. A., S. P. Serbin, E. L. Kruger, and J. A. Gamon. 2013. “Disentangling the Contribution of Biological and Physical Properties of Leaves and Canopies in Imaging Spectroscopy Data.” *Proceedings of the National Academy of Sciences* 110 (12): E1074–E1074.

Treuhaft, Robert N., Gregory P. Asner, and Beverly E. Law. 2003. “Structure-Based Forest Biomass from Fusion of Radar and Hyperspectral Observations.” *Geophysical Research Letters* 30 (9): 1472.

Tsai, Fuan, and William Philpot. 1998. “Derivative Analysis of Hyperspectral Data.” *Remote Sensing of Environment* 66 (1): 41–51.

Turpie, Kevin R., Victor V. Klemas, Kristin Byrd, Maggi Kelly, and Young Heon Jo. 2015. “Prospective HyspIRI Global Observations of Tidal Wetlands.” *Remote Sensing of Environment* 167: 206–17.

Twilley, Robert R., Samuel J. Bentley, Qin Chen, Douglas A. Edmonds, Scott C. Hagen, Nina S.N. Lam, Clinton S. Willson, et al. 2016. “Co-Evolution of Wetland Landscapes, Flooding, and Human Settlement in the Mississippi River Delta Plain.” *Sustainability Science* 11 (4): 711–31.

U.S. Geological Survey. “USGS NED ned19_n29x75_w091x50_LA-USGS_Atchafalaya2 2012_2014 1/9 arc-Second 20140615 15 x 15 Minute IMG.” 2014. U.S. Geological Survey, Reston, VA, USA.

Wang, Cuizhen, Jiaping Wu, Yuan Zhang, Guangdong Pan, Jiaguo Qi, and William A. Salas. 2009. “Characterizing L-Band Scattering of Paddy Rice in Southeast China with Radiative Transfer Model and Multitemporal ALOS/PALSAR Imagery.” *IEEE Transactions on Geoscience and Remote Sensing* 47 (4): 988–98.

Zhang, M., Susan L. Ustin, E Rejmankova, and Eric W Sanderson. 1997. “Monitoring Pacific Coast Salt Marshes Using Remote Sensing.” *Ecological Applications* 7 (3): 1039–53.

## 3.8. Appendix

**Table 3-A1.** Herbaceous wetland aboveground biomass field sample data.

| Collection Date | Plot Size ($m^2$) | Latitude | Longitude | Dominant Species | AGB ($g/m^2$) |
|---|---|---|---|---|---|
| May 6, 2015 | 0.25 | 29.53893 | -91.38042 | *Sagittaria lancifolia* | 324.10 |
| May 6, 2015 | 0.25 | 29.53918 | -91.38051 | *Sagittaria lancifolia* | 401.52 |
| May 6, 2015 | 0.25 | 29.53943 | -91.38044 | *Sagittaria lancifolia* | 394.42 |
| May 8, 2015 | 0.25 | 29.42521 | -91.27973 | *Alternanthera philoxeroides* | 132.92 |
| May 8, 2015 | 0.25 | 29.47480 | -91.10216 | *Spartina alterniflora* | 332.30 |
| May 8, 2015 | 0.25 | 29.42525 | -91.27923 | *Ludwigia grandiflora* | 259.50 |
| May 8, 2015 | 0.25 | 29.42533 | -91.27925 | *Typha domingensis* | 299.20 |
| May 8, 2015 | 0.25 | 29.42527 | -91.27888 | *Typha domingensis* | 519.10 |
| May 8, 2015 | 0.25 | 29.42527 | -91.27280 | *Colocasia esculenta* | 244.44 |
| May 8, 2015 | 0.25 | 29.50637 | -91.23360 | *Saururus cernuus* | 126.00 |
| May 9, 2015 | 0.25 | 29.41716 | -90.94989 | *Sagittaria lancifolia* | 451.28 |
| May 9, 2015 | 0.25 | 29.41719 | -90.94984 | *Eleocharis radicans* | 338.00 |
| May 9, 2015 | 0.25 | 29.41759 | -90.95010 | *Sagittaria lancifolia* | 908.76 |
| May 9, 2015 | 0.25 | 29.41762 | -90.95002 | *Sagittaria lancifolia* | 622.20 |
| May 9, 2015 | 0.25 | 29.41796 | -90.95036 | *Sagittaria lancifolia* | 379.44 |
| November 15, 2016 | 0.25 | 29.50650 | -91.44556 | *Colocasia esculenta* | 250.04 |
| November 15, 2016 | 0.25 | 29.50644 | -91.44558 | *Colocasia esculenta* | 351.44 |
| November 15, 2016 | 0.25 | 29.50639 | -91.44567 | *Colocasia esculenta* | 253.72 |
| November 15, 2016 | 0.25 | 29.50672 | -91.44564 | *Colocasia esculenta* | 243.32 |
| November 15, 2016 | 0.25 | 29.50664 | -91.44550 | *Colocasia esculenta* | 279.68 |
| November 15, 2016 | 0.49 | 29.50664 | -91.44539 | *Colocasia esculenta* | 482.02 |
| November 15, 2016 | 0.49 | 29.50656 | -91.44542 | *Colocasia esculenta* | 348.67 |
| November 15, 2016 | 0.75 | 29.50639 | -91.44541 | *Colocasia esculenta* | 255.73 |
| November 15, 2016 | 0.75 | 29.50647 | -91.44531 | *Colocasia esculenta* | 380.67 |
| November 15, 2016 | 0.75 | 29.50655 | -91.44576 | *Colocasia esculenta* | 402.40 |

**Table 3-A2.** Forested wetland aboveground biomass field sample data.

| Collection Date | Plot Radius (m) | Latitude | Longitude | Dominant Species | AGB ($g/m^2$) |
|---|---|---|---|---|---|
| May 6-8, 2015 | 10 | 29.51538 | -91.43171 | *Salix nigra* | 38,030 |
| May 6-8, 2015 | 10 | 29.51121 | -91.43267 | *Salix nigra* | 8160 |
| May 6-8, 2015 | 10 | 29.51070 | -91.42787 | *Salix nigra* | 42,590 |
| May 6-8, 2015 | 10 | 29.50545 | -91.43219 | *Salix nigra* | 30,100 |
| May 6-8, 2015 | 10 | 29.61462 | -91.32393 | *Taxodium distichum* | 19,552 |
| May 6-8, 2015 | 10 | 29.49074 | -91.43710 | *Salix nigra* | 8850 |
| May 6-8, 2015 | 10 | 29.61431 | -91.32350 | *Salix nigra* | 1790 |
| May 6-8, 2015 | 10 | 29.51413 | -91.43279 | *Salix nigra* | 51,520 |
| May 6-8, 2015 | 10 | 29.51214 | -91.43756 | *Salix nigra* | 23,100 |
| May 6-8, 2015 | 10 | 29.51361 | -91.44246 | *Salix nigra* | 16,350 |
| May 6-8, 2015 | 10 | 29.51607 | -91.45768 | *Salix nigra* | 13.830 |
| May 6-8, 2015 | 10 | 29.51266 | -91.45770 | *Salix nigra* | 30,210 |
| May 6-8, 2015 | 10 | 29.50539 | -91.44698 | *Salix nigra* | 3070 |
| May 6-8, 2015 | 10 | 29.53821 | -91.44451 | *Salix nigra* | 36,300 |
| May 6-8, 2015 | 10 | 29.53608 | -91.43400 | *Salix nigra* | 66,080 |
| May 6-8, 2015 | 10 | 29.53263 | -91.43570 | *Salix nigra* | 34,780 |
| May 6-8, 2015 | 10 | 29.50715 | -91.44643 | *Salix nigra* | 5180 |
| May 6-8, 2015 | 10 | 29.53821 | -91.44451 | *Salix nigra* | 36,300 |
| May 6-8, 2015 | 10 | 29.53608 | -91.43400 | *Salix nigra* | 66,080 |
| May 6-8, 2015 | 10 | 29.53263 | -91.43570 | *Salix nigra* | 34,780 |
| May 6-8, 2015 | 10 | 29.51538 | -91.43171 | *Salix nigra* | 38,030 |
| May 6-8, 2015 | 10 | 29.51413 | -91.43279 | *Salix nigra* | 51,520 |
| May 6-8, 2015 | 10 | 29.51121 | -91.43267 | *Salix nigra* | 8160 |
| May 6-8, 2015 | 10 | 29.51070 | -91.42787 | *Salix nigra* | 42,590 |
| May 6-8, 2015 | 10 | 29.51214 | -91.43756 | *Salix nigra* | 23,100 |
| May 6-8, 2015 | 10 | 29.51361 | -91.44246 | *Salix nigra* | 16,350 |
| May 6-8, 2015 | 10 | 29.51607 | -91.45768 | *Salix nigra* | 13,830 |
| May 6-8, 2015 | 10 | 29.51299 | -91.45649 | *Salix nigra* | 16,710 |
| May 6-8, 2015 | 10 | 29.52044 | -91.44769 | *Salix nigra* | 29,990 |
| May 6-8, 2015 | 10 | 29.49821 | -91.45908 | *Salix nigra* | 24,020 |
| May 6-8, 2015 | 10 | 29.51266 | -91.45770 | *Salix nigra* | 30,210 |
| May 6-8, 2015 | 10 | 29.50545 | -91.43219 | *Salix nigra* | 30,100 |
| May 6-8, 2015 | 10 | 29.50539 | -91.44698 | *Salix nigra* | 3070 |
| May 6-8, 2015 | 10 | 29.49074 | -91.43710 | *Salix nigra* | 8850 |
| May 6-8, 2015 | 10 | 29.48458 | -91.43940 | *Salix nigra* | 10,430 |
| May 6-8, 2015 | 10 | 29.51120 | -91.44429 | *Salix nigra* | 6370 |

**Table 3-A3.** Aboveground biomass ordinary least squares regression models.

| | **Herbaceous Model Coefficient** | **Forest Model Coefficient** |
|---|---|---|
| Derivative PLS Component 1 | -1966.287 | |
| Derivative PLS Component 2 | -11555.016 | |
| Reflectance PLS Component 1 | | 1188.786 |
| Reflectance PLS Component 2 | | -16,737.491 |
| Reflectance PLS Component 3 | | -194,039.813 |
| Reflectance PLS Component 4 | | -41,831.015 |
| Volume Scattering Component | -7.293 | 1471.021 |
| Double Bounce Scattering Component | 3.418 | -1398.494 |
| Constant | 339.758 | 23,568.644 |

*Volume and double bounce scattering component values are inherently negative. The coefficient sign is indicative of an inverse relationship if positive or a positive relationship if negative.

# Chapter 4

## Accretion-Driven Variation in Vegetation Composition and Biomass in Louisiana's Wax Lake Delta

### 4.1. Abstract

Louisiana's Wax Lake Delta (WLD) is an actively prograding delta in a coastal region that is otherwise experiencing widespread degradation and submergence of its coastal wetlands. Because the WLD is actively accreting sediment and organic matter to build soil surface elevation, the composition of its emergent wetland vegetation communities is highly dynamic. However, there is uncertainty about how net changes in soil elevation impact aboveground carbon storage across species. This study utilizes high resolution data imaging spectrometer captured to map the delta's dominant vegetation species and types. We validated this vegetation map (overall accuracy = 77.62%, Kappa = 0.72) and compared it with a published species map that used WorldView-2 data collected five years earlier (Carle et al. 2014). This allowed us to map changes resulting from five years of accretion and elevation gain for a wetland forest species (*Salix nigra*), two dominant herbaceous wetland species (*Colocasia esculenta* and *Polygonum punctatum*), and various grass species. Results show a significant increase in *C. esculenta* and a marginal increase in forested wetlands (*S. nigra*). The former increase occurred largely outwards toward the delta fringes into wetland area previously occupied by *P. punctatum*, which saw a corresponding recession in the deltaic islands. Additionally, this study leveraged these species distributions with a published aboveground biomass (AGB) dataset (Jensen et al. 2019b) to examine the dominant plant types' growth patterns across elevational gradients. We characterized variability in AGB by marsh platform elevation and across different elevational zones categorized by hydroperiod, or hydrogeomorphic zones (HGZ). We found that the herbaceous plant species peak in AGB in the

low intertidal zone and decrease with elevation before increasing slightly in the highest elevations. These remote sensing-derived results specifically for *C. esculenta* agree with aboveground net primary production values derived from a controlled marsh organ experiment conducted in the delta. With vegetation distributions, succession, and growth patterns in the WLD characterized, this study may inform future restoration efforts throughout the Mississippi Deltaic Plain regarding the changing vegetation composition that may emerge with similar river diversion projects.

## 4.2. Introduction

Louisiana's coast is rapidly submerging, with nearly 4000 $km^2$ of wetlands lost statewide since 1956, with an ongoing rate of 44 $km^2$ of wetland area being lost each year (Barras et al. 2003; Barras et al. 2008; Twilley et al. 2016). Wetland loss in the Mississippi Deltaic Plain (MDP) has been largely driven by extensive coastal engineering that has starved its floodplains of sediment supply (Day et al. 2007). Today, the Atchafalaya River and the adjoining Wax Lake Outlet are the primary distributaries of the main river, with the latter dredged out of a mosaic of forested and herbaceous wetlands in 1942 to divert flow and relieve flooding along the former (Shlemon 1975). Contrary to the greater MDP where sediment deposition has decreased, wetlands here are undergoing significant aggradation, with the recent emergence of the Wax Lake Delta (WLD) creating a novel ecosystem of deltaic floodplains and accretion-driven feedbacks (Twilley et al. 2016; Twilley et al. 2019) where areal land growth rates range between 1-3 $km^2$/yr (Allen et al. 2012). Despite the Wax Lake Outlet being an artificial channel, the active WLD has built land under essentially natural hydrologic conditions—resulting from significantly higher sediment deposition and accretion than nearby inactive wetlands in the Terrebonne and Barataria coastal basins (Jensen et al. 2019a)—making the delta an ideal case study for informing river diversion

projects aiming to counteract wetland subsidence across the greater MDP (Bevington et al. 2017). Here we characterize how the WLD's significant accretion and the subsequent change in soil elevation over five years has affected vegetation composition and biomass distributions. The higher rates of accretion in the WLD compared to surrounding inactive coastal basins are likely to have large impacts on wetland species distributions and biomass storage.

Accretion—the trapping of mineral sediments and deposition of organic matter—largely governs delta development and wetland submergence, and is further dependent on vegetation species, structure, and biomass (Morris et al. 2002; Mudd et al. 2009; Kirwan and Guntenspergen 2010; Kirwan et al. 2010). A negative feedback cycle connects accretion and bioproductivity, processes that are spatially variable across emergent wetlands and help change wetland soil elevation**.** Biomass is an important ecological component that drives accretion, as organic matter deposition and root turnover make up accretion's organic component (FitzGerald et al. 2008). More productive plants generate more organic matter, in turn elevating the marsh platform (Figure 4-1). However, lower elevation and more inundation time forces wetland plants' net primary productivity to increase, increasing overall accretion via organic matter deposition (Morris et al. 2002). In addition to this biogenic feedback, biomass is a key factor in inorganic sediment trapping (Kirwan and Megonigal 2013), making wetland stability and surface elevation dependent on the interplay of sea level, soil elevation, vegetation type, primary productivity, and inorganic accretion (Morris et al. 2002). An aggrading marsh ecosystem, such as the WLD, with increasing overall biomass likely has concurrently increasing accretion potential and ability to trap sediment to increase the soil surface elevation (Mudd et al. 2009). In addition to being an indicator of overall wetland health, accurate landscape-scale estimates of aboveground biomass (AGB)—the observable portion of vegetation biomass above the soil—may form an essential parameter for

predicting changes in total wetland carbon storage (Morris et al. 2002; Craft et al. 2009; Kirwan and Guntenspergen 2010). These processes vary across landscapes, and thus necessitate spatially discrete and comprehensive analysis.

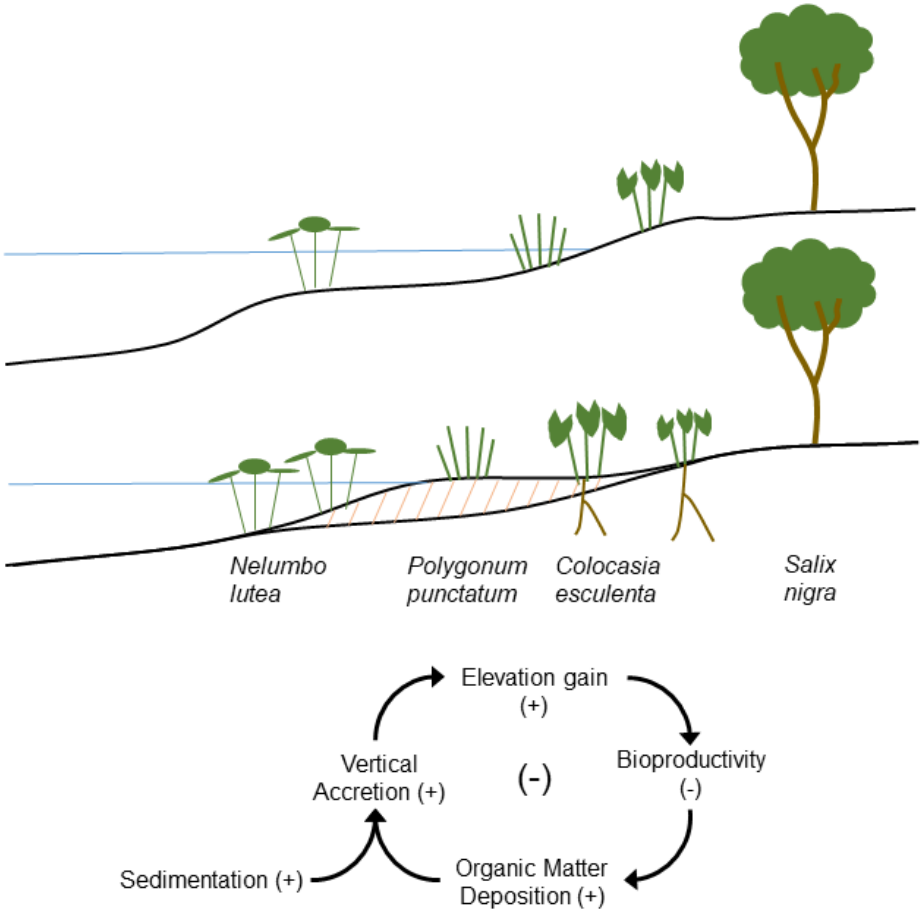


**Figure 4-1.** Dominant species composition in the WLD. Species shown by elevation, along with associated negative feedback loop driving elevation gain.

Sediment accretion and the resulting shifts in marsh platform elevation affect plant species composition and net primary productivity. Wetland species distributions vary across hydrogeomorphic zones (HGZs)—zones that have a specific interaction of soil elevation, hydrology, and salinity that controls the landscape distribution of wetland vegetation (Krauss et al. 2014; Twilley et al. 2019). In deltaic floodplains, these HGZs are principally determined by

soil elevation and hydroperiod, as defined by flooding frequency, duration, and depth (Twilley et al. 2019). Species with particular flood tolerances dominate in specific elevation niches (Figure 4-1). Characterizing each species by its elevation distribution in tandem with mapping temporal changes in species distributions provide insight into how accretionary processes are impacting wetland elevation. Accurately mapping species distribution may further inform efforts towards modeling AGB and productivity. A landscape-scale AGB estimate would further allow HGZs to be characterized by their constituent plants' growth patterns. While HGZs can be characterized by their species compositions, some species are found across different zones (Carle et al. 2015; Ma et al. 2018). The WLD's dominant vegetation types vary with elevation and inevitably vary in productivity and biomass allocation. As these processes vary across the deltaic floodplain, remote sensing offers valuable tools to assess spatially and ecologically complex relationships. To conduct this analysis, new remote sensing approaches utilizing the unique strengths of various sensors are developed to assess such spatially and ecologically complex relationships.

Accurate species and biomass maps offer a baseline to examine ecological variables that drive sediment accretion. For example, satellite and airborne instruments can attain regional-scale data that may be used to map wetland land-cover and assess environmental health and change. However, multispectral data may be insufficient for discriminating vegetation type and composition in this environment. Wetland vegetation types are difficult to distinguish due to their frequently similar spectra, variable local hydrology, and underlying soil influence (Adam et al. 2010). Further, wetland vegetation assemblages often have a high degree of spectral and spatial variability due to steep environmental gradients and short ecotones (Adam and Mutanga 2009; Adam et al. 2010) in addition to the increased radiative attenuation in mid- to near-infrared spectral zones (Zomer et al. 2008). Compared to moderate-resolution multispectral data, airborne imaging

spectrometers offer an ideal remote sensing platform for mapping wetland species composition in the WLD, as higher spatial and spectral resolutions may mitigate these confounding environmental variables (Belluco et al. 2006). In mapping a region's vegetation assemblage, distinguishing species enables improvements in characterizing plant biomass and productivity, accretionary processes, and changes in extent (Adam et al. 2010; Byrd et al. 2014). Additionally, remote sensing provides efficient tools for estimating AGB on landscape and regional scales.

This study leverages a multi-sensor airborne remote sensing dataset to assess how accretion governs the composition and succession of vegetation communities in the WLD. We investigate how the distribution and composition of vegetation in the WLD changed with its accretion and expansion from 2011 to 2016. We also investigate whether species' AGB significantly varies across HGZs, characterizing their productivity and biomass allocation across space in doing so. We hypothesize that species characteristic of higher elevations have supplanted lower elevation species as the WLD has accreted, and that species that span HGZs have higher biomass densities at lower elevations in response to increased flooding.

## 4.3. Methods

### *4.3.1. Remote Sensing Data and Preprocessing*

The Airborne Visible-Infrared Imaging Spectrometer-Next Generation (AVIRIS-NG) measures 14-bit radiance from 380 to 2510 nm wavelengths with a ~5 nm spectral resolution (Hamlin et al. 2010; Thompson et al. 2015). AVIRIS-NG conducted five flightlines over the WLD on October 17, 2016, producing individual datasets with 425 bands at a 5.4 m spatial resolution. Each raw dataset was atmospherically corrected using the physics-based ATmospheric REMoval (ATREM) algorithm to derive a surface reflectance image (Gao et al. 1993; Bue et al. 2015;

Thompson et al. 2015). We applied the Adaptive Reflectance Geometric Correction (ARGC) algorithm to correct bidirectional reflectance distribution (BRDF) effects that cause across-track variations in observed illumination intensity (Jensen et al. 2017). After producing spectrally consistent surface reflectance data with the ARGC, we mosaicked the flightlines and subset the resulting dataset to the WLD's extent (Figure 4-2). We utilized 290 of the original 425 AVIRIS-NG bands, excising bands within the 376.44-441.55, 892.33-942.42, 1107.71-1157.79, 1353.13-1488.36, 1783.88-2024.29, and 2404.95-2500.12 nm spectral regions due to atmospheric water vapor interference.

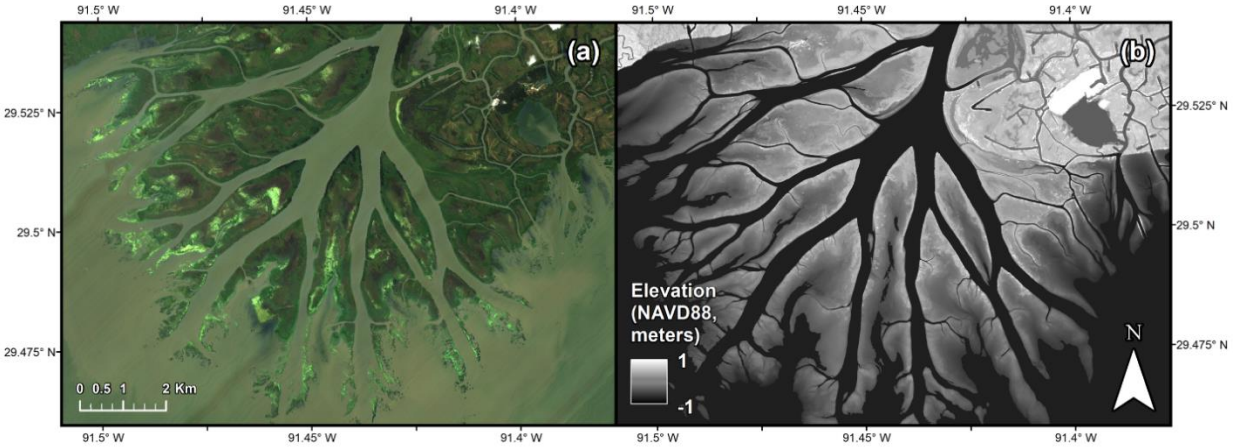


**Figure 4-2.** Remote sensing data used for vegetation mapping. (a) True color composite of the processed AVIRIS-NG mosaic subset to the WLD, and (b) the USGS LiDAR DTM over the same domain.

A digital terrain model (DTM) (Figure 4-2), expressed in meters relative to the North American Vertical Datum of 1988, based on Light Detection and Ranging (LiDAR) was collected from the National Elevation Dataset (U.S. Geological Survey 2014). The USGS collected these data over the on December 18, 2012. This collection followed many of the present species' senescence and is coincident with a low water level, leaving much of the marsh platform exposed

above water for optimal elevation retrieval. Using the elevation ranges outlined by Twilley et al. (2019), we classified this DTM into HGZs (Figure 4-3).

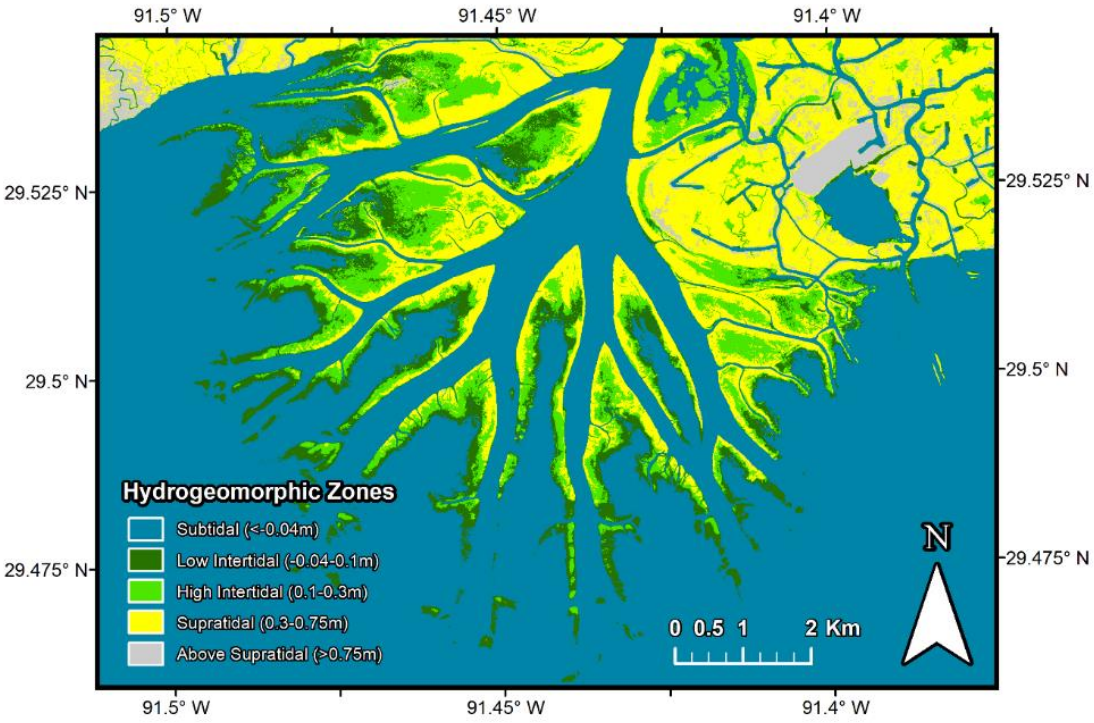


**Figure 4-3.** Hydrogeomorphic zones derived from the USGS LiDAR DTM.

### *4.3.2. Vegetation Distributions*

#### *4.3.2.1. Vegetation Species/Type Classification*

We employed an unsupervised classification approach to map vegetation species composition in the WLD. We selected an unsupervised approach due to a lack of suitable training data and the infeasibility of locating every species present in the field in large, representative stands. Additionally, an unsupervised approach is useful for informing the separability of a region's potential classes, thus determining which dominant species have distinguishable characteristics *vis a vis* the remote sensing data. To this end, a Principal Components Analysis

(PCA) was applied to the 290-band AVIRIS-NG mosaic to reduce data dimensionality and produce component images whose loading values indicate varying spectral characteristics. Dimension reduction facilitates the integration of additional data sources, ensuring the elevation data is sufficiently weighed in the classification algorithm, and allows for the omission of spectral information and noise that do not contribute to the classification. Of the output PCA bands, nine were selected (Figure 4-4) based on the existence of coherent structure, while the discarded bands appeared to be dominated by striping effects from the instrument's pushbroom sensor array, residual BRDF effects, or noise. We stacked these nine PCA bands with the DTM (U.S. Geological Survey 2014), forcing the classification to account for marsh platform elevation when determining class distributions. We then applied an ISODATA classification with a minimum of 50 output classes, a maximum class standard deviation value of one, and a minimum class distance value of three to maximize the separation of key vegetation groupings.

The raw output classes were assigned a land cover class based on visual inspection. This analysis was further informed by prior published data (Carle et al. 2014) and *in situ* photographs of *Salix nigra, Colocasia esculenta, Polygonum punctatum, Nelumbo lutea,* Submerged Aquatic Vegetation (SAV), grasses, and floating vegetation. Based on *in situ* data, the primary forb species—herbaceous broadleaf plants that are not woody or grasses (Byrd et al. 2018)—were adequately distinguished such that one or more output classes were dominated by those individual species. The *C. esculenta* and *P. punctatum* classes did not require the combining of multiple raw ISODATA output classes, whereas other vegetation classes in Figure 4-5 are the product of several output classes that required manual identification. Individual grass species, however, did not dominate across separate output classes and were thus grouped into a single parent class. This class includes *Zizianiopsis miliacea, Phragmites australis, Typha latifolia,* and *Leersia hexandra*. For

each of these classes, in addition to *N. lutea*, we extracted elevation values from DTM (Figure 4-2) for each relevant pixel to examine areal and elevation characteristics (Table 4-1). The SAV class is largely composed of *Potamogeton nodosus*, though we did not distinguish between other potential SAV species. The floating vegetation class includes water hyacinth (*Eichornia crassipes)*, a transient floating macrophyte that tends to gather along banks and island interiors, and common duckweed (*Lemma minor*), which consists of small oval leaves that tend to cover the surface of still waters. Duckweed is apparent in the AVIRIS-NG imagery as bright green patches, frequently covering areas of recently senesced *N. lutea.*

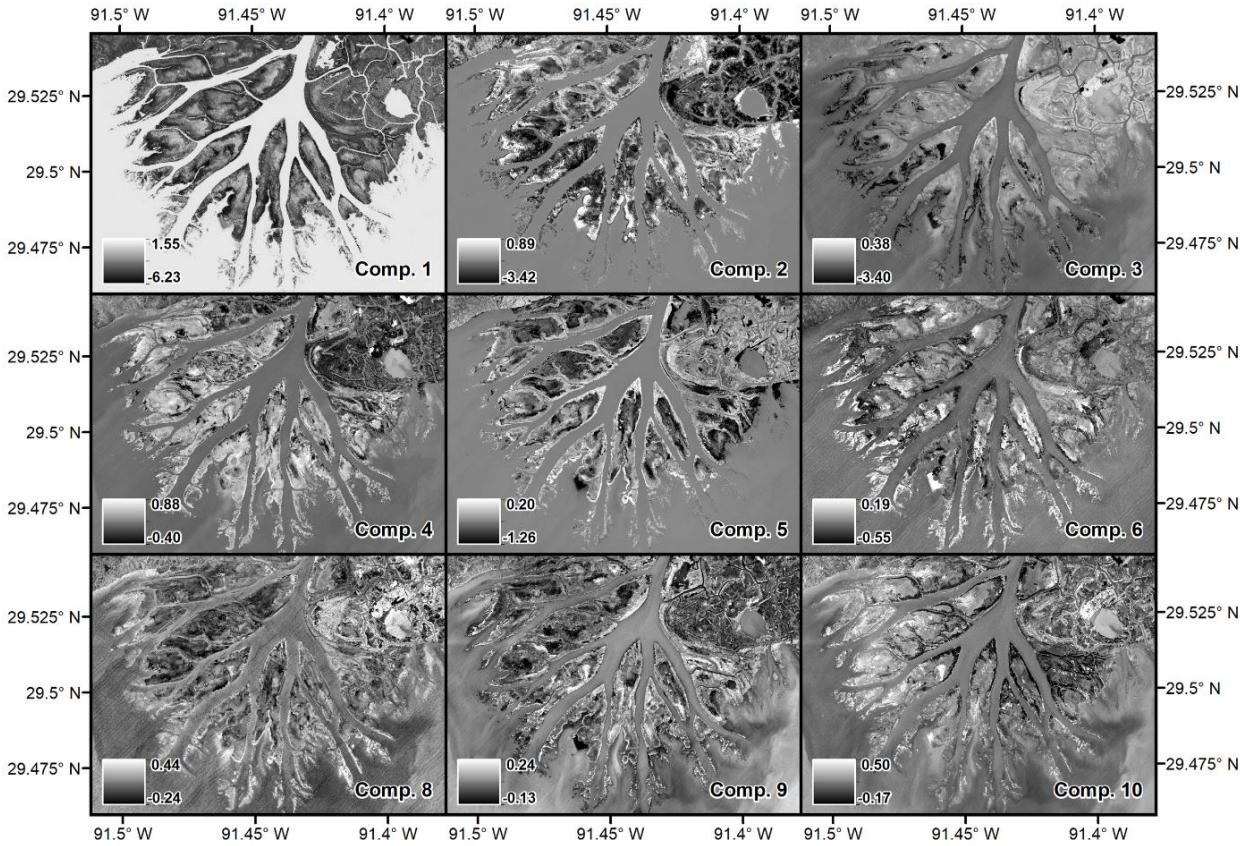


**Figure 4-4.** PCA components utilized in the ISODATA classification. Legend values denote component loading values. Component 7 was not included due to excess visible noise.

#### *4.3.2.2. Classification Validation*

We validated the classification by conducting an *in situ* survey of the grouped ISODATA classification output. We selected seven transect sites where the classification map showed diverse species composition across an apparent elevational gradient, with special focus on the four primary species (*S. nigra, C. esculenta, P. punctatum,* and *N. lutea*). Each transect was approximately 200 meters long and *in situ* species observations were taken every ten meters. This ensured each validation point was a separate pixel on the 5.4 m resolution map, resulting in 143 total observations being recorded. At each observation, we recorded a GPS point, an overhead picture for visual interpretation, and the species present within the surrounding square meter in order of percent composition. The species with the greatest presence at each observation was considered to be the point's dominant species. These *in situ* data were compared against their corresponding map pixel class value to compile a confusion matrix (Table 4-1). The forb species *Bidens laevis* and *Sagittaria lancifolia* were present at the surveyed sites. While we observed them to be dominant at a small number of *in situ* plots, they did not appear to be dominant across any of the ISODATA output classes, being surpassed by either *C. esculenta, P. punctatum,* or *N. lutea*. The former species are counted as "Other Forbs" in the confusion matrix's reference data (Table 4-1), though we did not include them in the map as dominant species. From the validation dataset and the confusion matrix, we calculated user's and producer's accuracies, overall accuracy, and Kappa values (Table 4-2).

#### *4.3.2.3. Vegetation Extent Changes*

We compared our classifications to a previous species map of the region (Carle et al. 2014) to characterize how vegetation has changed in the WLD between 2011 and 2016. Carle et al. (2014)

mapped species distributions using a Maximum Likelihood Classifier with 2 m resolution WorldView-2 data collected on October 11, 2011. We resampled this previous species map to our 5.4 m AVIRIS-NG-based map to track changes—loss, gain, or no change—in *P. punctatum, C. esculenta, S. nigra,* and grass extents. Neither dataset was suitable for mapping changes in *N. lutea,* a key species in the low intertidal zone, due to phenology at the time of each data acquisition. In 2016, *N. lutea* had started senescing in many areas, resulting in some areas being colonized by SAV or floating vegetation, while in 2011, data was captured following a storm event that temporarily converted much of the *N. lutea* area into mudflat.

#### *4.3.2.4. Aboveground Biomass*

Aboveground biomass (AGB) for herbaceous and forested wetlands in the WLD was produced using empirical models integrating data from AVIRIS-NG and Uninhabited Aerial Vehicle Synthetic Aperture Radar (UAVSAR), an airborne L-band radar instrument. The models and AGB products (Figure 3-11) were developed and cross-validated by Jensen et al. (2019b). The forested wetland AGB model utilizes a partial least squares (PLS) transformation of the AVIRIS-NG reflectance data in concert with the volume and double bounce scattering components from a polarimetric decomposition of the UAVSAR data (Freeman and Durden 1998). The herbaceous AGB model utilizes a similar approach, but instead utilizes the first derivative of reflectance from the AVIRIS-NG data in the PLS transformation, making the model more sensitive to canopy biochemical features relating to plant biomass (Jensen et al. 2019b). Both AGB models were applied to forested wetland land cover and herbaceous vegetation separately, in accordance with the classification map (Figure 4-5). The herbaceous model application excluded *N. lutea,* SAV, and floating vegetation. These classes were not included in the training dataset and have different

spectral characteristics due to their intermingling with water, in addition to *N. lutea*'s ongoing senescence at the time of AVIRIS-NG's image collection, making them unsuitable for accurate AGB estimation.

### *4.3.3. Marsh Organ Growth Experiment*

A mesocosm growth experiment was conducted within the WLD (Rovai et al. *in progress*), from which the results were compared to the remotely sensed biomass estimates and distributions. This allowed us to assess whether the modeled biomass estimates for *C. esculenta* vary across HGZs in accordance with experimentally observed growth. The mesocosm experiment consisted of a multi-elevation planter also known as a "marsh organ" (Morris 2007). The marsh organ consisted of four rows each, each with four 15.24 cm diameter PVC pipes placed at increasing heights in order to simulate different HGZs (low intertidal, high intertidal, supratidal, above supratidal) where *C. esculenta* have been observed to naturally occur (Figure 4-3). Target elevations were determined based on the 2012 USGS DTM (Figure 4-2; U.S. Geological Survey 2014). One *C. esculenta* plant along with undisturbed native soil was transplanted into each PVC pipe. The experiment spanned the 2018 growing season, from May to October (Carle et al. 2015; Carle et al. 2016; Twilley et al. 2019). At the end of the growing season, plants were retrieved and above- and belowground biomass separated before being rinsed, dried and weighed. Initial and final biomass values were derived by measuring the plants' dry weight, and net primary productivity (NPP) rates (g $m^{-2}$ $yr^{-1}$) were derived by subtracting final biomass values from the initial biomass reference values and integrating over the time duration of the experiment. In addition to aboveground biomass and NPP, belowground biomass and NPP were measured to

examine how the allocation of root versus stem material varies across HGZs. For a full description of the experimental design and processing, see Rovai et al. (*in progress*).

## 4.4. Results

### *4.4.1. Vegetation Type Distribution and Change*

Our vegetation map (Figure 4-5) shows *C. esculenta* dominates in the high intertidal zones of the deltaic island interiors, typically adjacent to the *S. nigra* stands that populate the island levees. In these islands, *P. punctatum* appears to populate a slightly lower zone adjacent to much of the *C. esculenta* before transitioning to *N. lutea*. However, many of the upland regions in the northernmost parts of the delta that are more connected to the mainland appear to be dominated by *P. punctatum*. Many large grass stands, typically *Z. miliacea* and *P. australis*, are also present in these parts of the WLD. Grasses are also abundant in the outer islands. While these grasses could not be distinguished from others in the classification, they visually appear (Figure 4-1) to be a different species—likely *T. latifolia*—that cover broader areas and are actively senescing at the time of image capture on October 17, 2016. The confusion matrix (Table 4-2) generated from the validation dataset show the total correctly identified points and whether misclassified points pertain to the classification (i.e. map pixel class) or reference (i.e. *in situ* observation) data. Class and overall accuracy metrics (Table 4-3) were calculated from the confusion matrix, showing an overall accuracy of 77.62% and a Cohen's Kappa of 0.72. The *S. nigra* class attained both high user's and producer's accuracies, while the other classes differ between the two metrics. *C. esculenta* shows a high user's accuracy and lower producer's accuracy, while *P. punctatum* and grasses reverse this pattern. *N. lutea* also shows a lower user's accuracy, though it attains higher

accuracies overall than the other herbaceous classes. Similar accuracy metrics are shown for the October 11, 2011, classification (Carle et al. 2014).

**Table 4-1.** Elevation statistics for each primary vegetation type on October 17, 2016

| | ***Salix nigra*** | ***Colocasia esculenta*** | ***Polygonum punctatum*** | **Grasses** | ***Nelumbo lutea*** |
|---|---|---|---|---|---|
| **Total Area ($km^2$)** | 0.93 | 2.87 | 4.05 | 3.00 | 21.22 |
| **Mean Elevation (m)** | 0.55 | 0.41 | 0.42 | 0.33 | -0.04 |
| **Elevation Range (m) ($25^{th}$–$75^{th}$ percentile)** | 0.28–2.70 (0.45–0.59) | 0.00–1.79 (0.33–0.49) | 0.01–2.30 (0.35–0.50) | -0.24–2.69 (0.18–0.44) | -0.75–0.84 (-0.17–0.15) |
| **Elevation Standard Deviation (m)** | 0.16 | 0.13 | 0.12 | 0.20 | 0.26 |

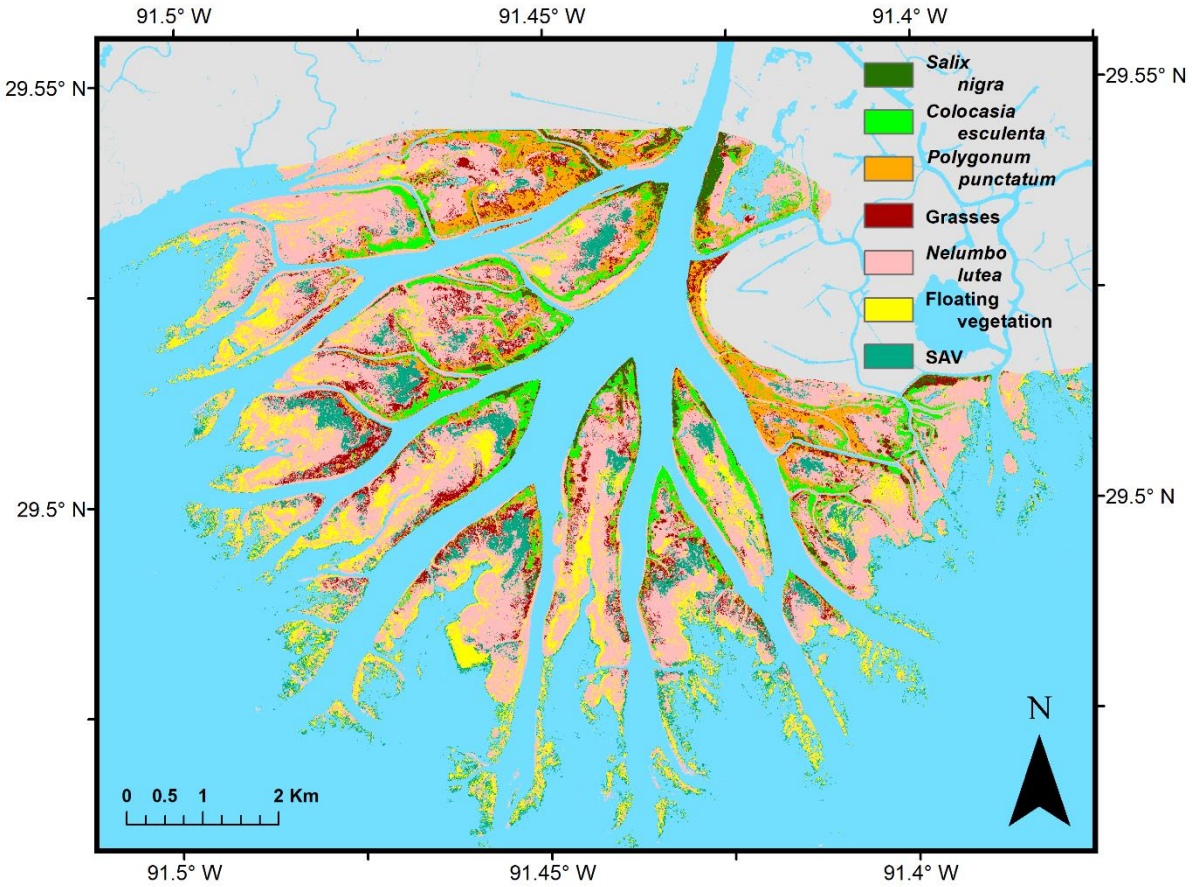


**Figure 4-5.** Vegetation species/type classification of the Wax Lake Delta.

**Table 4-2.** Classification validation confusion matrix

| | | Reference Data | | | | | | | |
|---|---|---|---|---|---|---|---|---|---|
| | | ***Salix nigra*** | ***Colocasia esculenta*** | ***Polygonum punctatum*** | **Grasses** | ***Nelumbo lutea*** | **Floating vegetation** | **Other Forbs** | **All** |
| Classification Data | ***Salix nigra*** | **21** | 0 | 0 | 0 | 0 | 0 | 0 | 21 |
| | ***Colocasia esculenta*** | 0 | **19** | 2 | 1 | 0 | 0 | 1 | 23 |
| | ***Polygonum punctatum*** | 0 | 6 | **13** | 1 | 0 | 0 | 4 | 24 |
| | **Grasses** | 1 | 3 | 0 | **13** | 0 | 0 | 4 | 21 |
| | ***Nelumbo lutea*** | 0 | 1 | 0 | 3 | **45** | 3 | 2 | 54 |
| | **All** | 22 | 29 | 15 | 18 | 45 | 3 | 11 | **143** |

**Table 4-3.** Classification validation accuracy

| | **User's Accuracy (%)** | **Producer's Accuracy (%)** |
|---|---|---|
| ***Salix nigra*** | 100.00 | 95.45 |
| ***Colocasia esculenta*** | 82.61 | 65.55 |
| ***Polygonum punctatum*** | 54.17 | 86.67 |
| **Grasses** | 61.90 | 72.22 |
| ***Nelumbo lutea*** | 83.33 | 100.00 |
| **Overall Accuracy (%)** | 77.62 | |
| **Kappa** | 0.72 | |

Comparison of the classification for October 17, 2016 (Figure 4-5), with Carle et al.'s species map from October 16, 2011 reveals significant changes in the four primary vegetation types (Figure 4-6). It is important to note that the change in *N. lutea*'s extent was not examined due in part to unsuitability of the 2011 data, where a hurricane had recently converted much of the deltaic island interiors where it is most prevalent into bare mudflat (Carle et al. 2014). Additionally, at the time of AVIRIS-NG's flights in 2016, much of the *N. lutea* was senescent. Paired datasets captured at *N. lutea*'s peak extents in different years prior to disturbance or senescence would be required to accurately map such a change. The grasses display significant change, with a net decrease of 0.38 km$^2$ (-11.24%). The change appears dynamic, with an increase in grass presence in 2016 along the inner delta island banks despite a decrease along the island levees and interiors.

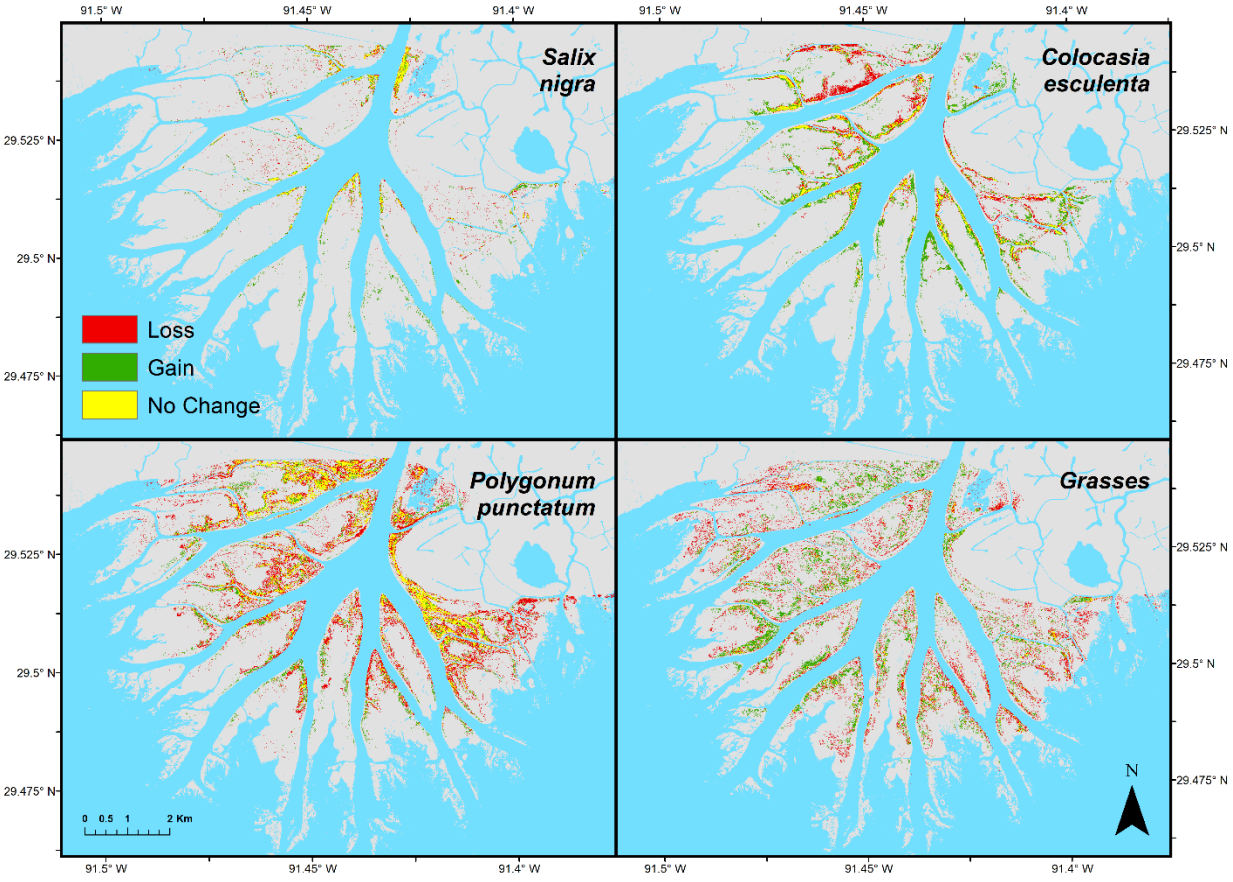


**Figure 4-6.** Changes in vegetation and species type extents. *Salix nigra*, *Colocasia esculenta*, *Polygonum punctatum*, and grass changes from October 16, 2011 to October 17, 2016.

*S. nigra* sees a modest net increase of 0.14 $km^2$ (+17.72%), with much of its expansion occurring on the levees further out from the head of each deltaic island. *P. punctatum* shows the greatest extent change with a net loss of -1.58 $km^2$ (-28.06%). While the large upland banks in the northern and eastern parts of the delta remain largely dominated by *P. punctatum*, the species has significantly receded in the deltaic island interiors and inner banks. Conversely, *C. esculenta* significantly expanded with a net increase of 0.68 $km^2$ (+31.05%). This expansion largely occurred on the delta island banks as it has expanded outwards towards the delta fringes.

### *4.4.2. Aboveground Biomass Distribution*

We extracted the AGB pixel values (Figure 3-11; Jensen et al. 2019b) corresponding to each vegetation type to profile how biomass varies by elevation and across HGZs by species. Figure 4-7 shows the distribution of AGB values across the range of elevations in the WLD. The AGB profile values here are binned averages, banded by each bin's standard deviation. The minimum and maximum elevation values were denote each vegetation type's elevation interquartile range (IQR). The boxplot portion of Figure 4-7 aggregates each vegetation type's elevation and AGB data into HGZs, displaying the differences in median estimated AGB values across each HGZ where the plant types are present. Grass biomass is relatively high throughout the low and high intertidal zones, with AGB peaking at an elevation of approximately 0.1 m, before decreasing in the supratidal zone. *C. esculenta* and *P. punctatum* both reach their highest AGB in the low intertidal zone where they are at their lowest elevations. Both species' AGB decrease in concert through the supratidal zone before increasing slightly at their highest elevations. *S. nigra* exhibits the highest estimated AGB at approximately 0.3 m—the upper end of the high intertidal zone—but decreases rapidly before increasing steadily across the supratidal zone.

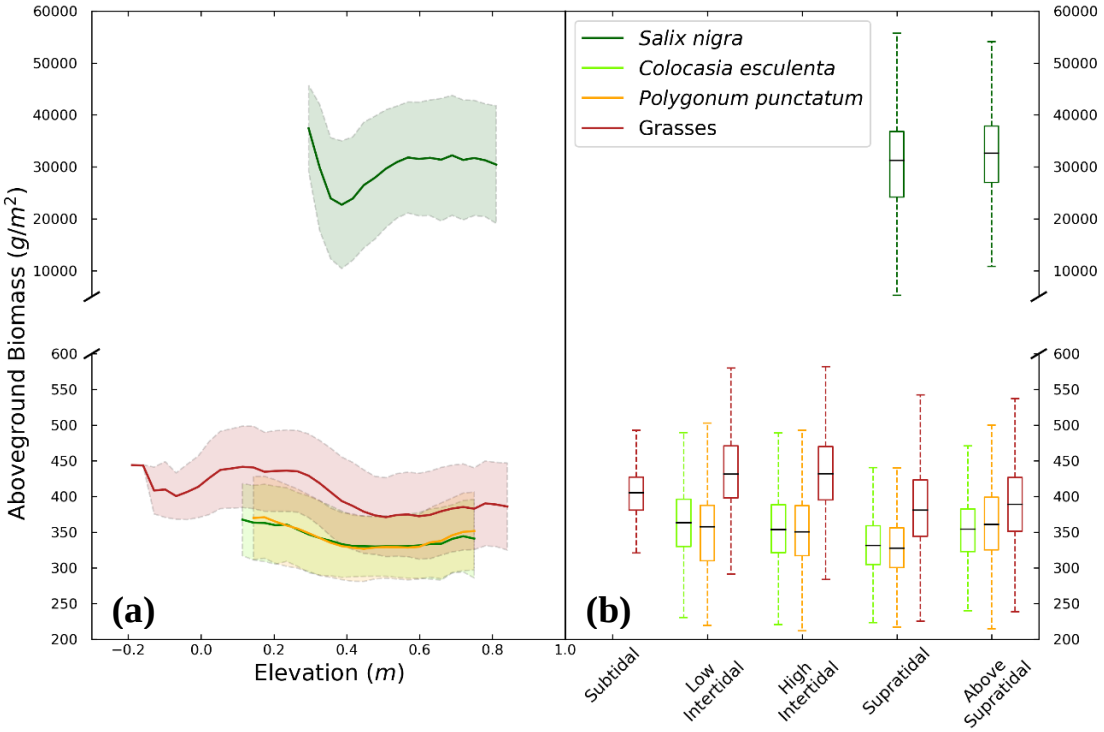


**Figure 4-7.** Elevational distribution of aboveground biomass for each vegetation type. The left panel (a) shows binned average AGB with 1 standard deviation bands. The right panel (b) shows AGB statistics within each hydrogeomorphic zone.

The marsh organ experiment conducted on Mike Island within the WLD (Rovai et al. *in progress*) further examines *C. esculenta*'s growth patterns as an example of a species that crosses HGZs (Figure 4-8). The aboveground portion of the biomass values was used along with the duration of the experiment (May-October 2018) to calculate the aboveground NPP in each simulated HGZ. The low intertidal, high intertidal, and supratidal zones, with respective mean aboveground NPP values of 355.63, 210.00, and 105.31g $m^{-2}$ $yr^{-1}$ show the same decreasing pattern as the remotely sensed AGB estimates (Figure 4-7). However, the above supratidal zone, with a mean NPP of 46.49 g $m^{-2}$ $yr^{-1}$, decreases further rather than increasing slightly. While aboveground biomass decreases with elevation in both the remotely sensed and experimental data, belowground

biomass does not vary as significantly and the derived root:shoot ratios show a clear increase with elevation (Table 4-4).

**Table 4-4.** Marsh organ averages for *Colocasia esculenta* (Rovai et al. *in progress*)

| Hydrogeomorphic Zone (Elevation, m) | Total Aboveground Biomass (g $m^{-2}$) | Aboveground NPP (g $m^{-2}$ $yr^{-1}$) | Total Belowground Biomass (g $m^{-2}$) | Belowground NPP (g $m^{-2}$ $yr^{-1}$) | Root: Shoot Ratio |
|---|---|---|---|---|---|
| Low Intertidal (0.03) | 1422.50 | 355.63 | 2237.64 | 559.41 | 1.59 |
| High Intertidal (0.2) | 840.00 | 210.00 | 3261.95 | 815.49 | 3.59 |
| Supratidal (0.5) | 421.25 | 105.31 | 1915.98 | 479.00 | 4.64 |
| Above Supratidal (0.8) | 185.97 | 46.49 | 2036.94 | 509.24 | 18.39 |

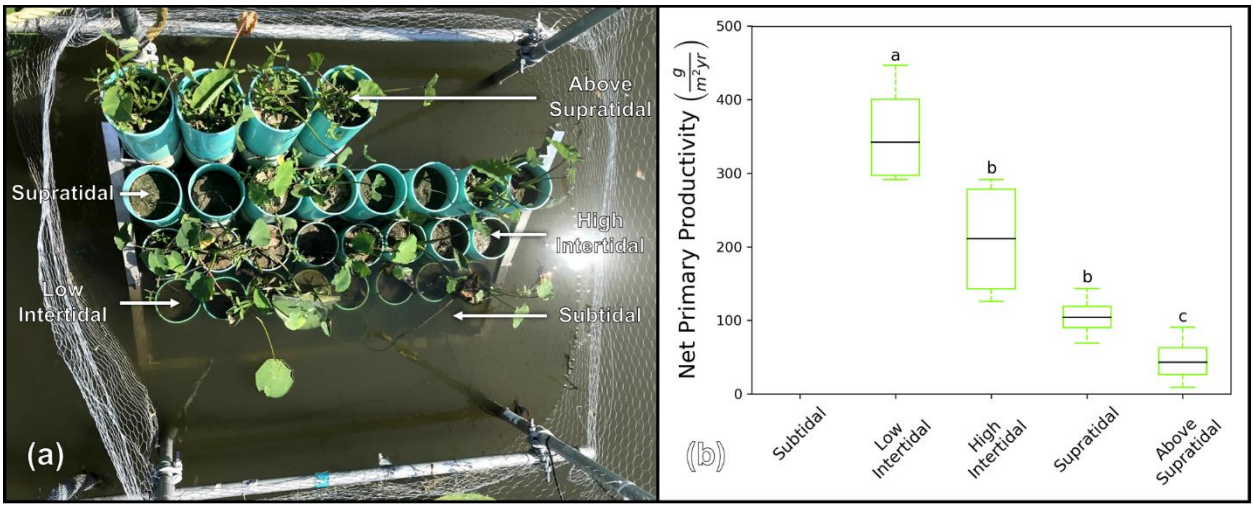


**Figure 4-8.** The marsh organ mesocosm experiment. (a) The marsh organ apparatus constructed in the WLD, and (b) *Colocasia esculenta* aboveground net primary productivity values derived from the experiment. Shared letters indicate no significant difference in mean values (with a $p < 0.05$ standard) as determined by one-way ANOVA (n = 4 for each HGZ sample set). From Rovai et al. (*in progress*).

### 4.5. Discussion

The current distribution of vegetation species and types in the WLD (Figure 4-5) shows the clustering of *S. nigra* and *C. esculenta* on the deltaic island levees at relatively high elevations.

The *P. punctatum* on the deltaic islands typically occupies the transitional space lower than or intermingled with *C. esculenta*, though it dominates the eastern and northwestern banks of the large islands that are more connected with the mainland. This indicates that while *C. esculenta* and *P. punctatum* occupy similar elevational niches, *C. esculenta* preferentially occupies and dominates the newly emergent marshland. This pattern is borne out in the vegetation extent change maps (Figure 4-6). While a minor outward expansion and net gain in *S. nigra* is detected (+0.14 $km^2$), there are much greater changes in *C. esculenta* (+0.68 $km^2$) and *P. punctatum* (-2.40 $km^2$). *C. esculenta*, an invasive species in Louisiana, shows significant outward growth towards the delta fringes from October 2011 to October 2016, clearly indicating significant accretion along the deltaic island banks in concert with this species' dominance of the islands' supratidal HGZ. *C. esculenta* has been shown to be an effective pioneer species following disturbance. While the species dominates the WLD's higher intertidal and supratidal emergent communities (Bevington 2016), lower elevations exhibited greater diversity prior to storm events (Twilley et al. 2019). In the following years, these regions saw significant expansion by *C. esculenta* without a return to pre-disturbance compositional diversity. Therefore, it is likely that complex interactions of elevation, interspecific competition, and disturbance patterns favor *C. esculenta's* expansion in the WLD (Twilley et al. 2019).

Other studies have shown *C. esculenta* to occupy a slightly higher elevational niche than *P. punctatum* (Carle et al. 2015; Ma et al. 2018), which contrasts with elevation distributions found in this study for the two species (Table 4-1). It is likely that this discrepancy is due to *C. esculenta*'s significant expansion and replacement of *P. punctatum* in the outer deltaic islands coupled with significant accretion taking place over the five year span. Conversely, the *P. punctatum* on the northern, more connected islands remained largely intact—though the *in situ* validation field study

revealed these regions to be intermixed with other forb and grass species while remaining largely dominated by *P. punctatum*. This could be due to more well-established connectivity between the wetland surface and deltaic channels. It should also be noted that while the DTM (U.S. Geological Survey 2014) represents the best available marsh platform elevation data, additional accretion will have taken place since the dataset's production. As the more established areas are higher in elevation than the deltaic islands, the resulting elevation range calculated from the 2016 map are likely higher than those calculated from earlier datasets (Carle et al. 2015; Ma et al. 2018).

In addition to the 2016 classification's overall accuracy (77.62%, Kappa = 0.72) the accuracy assessment (Table 4-2, Table 4-3) quantifies individual class accuracy and informs the interpretation of class distributions. *C. esculenta* shows a higher user's accuracy (82.61%) than producer's accuracy (65.55%), largely due to several *P. punctatum* observations in the classified imagery being mislabeled (i.e. six *C. esculenta in situ* validation points were classified as *P. punctatum*). This pattern is reversed for *P. punctatum*, which has a lower user's accuracy (54.17%) than producer's accuracy (86.67%). The primary contributor to this discrepancy is the higher number of *C. esculenta* or other forb species reference points disagreeing with the pixel classification. In much of the field observations, areas that are *P. punctatum*-dominant are intermixed with other species, whereas *C. esculenta* tends to completely cover a given area in its primary elevation range. Despite the varying degrees of mixing among these classes, two factors indicate that the mapped expansion in the major vegetation types accurately captures the five-year change (Figure 4-6). For one, there are large areas—shown in yellow in Figure 4-6—in both years' classification maps for *S. nigra, C. esculenta,* and *P. punctatum* that we would expect to remain stable. Secondly, the pattern of user's and producer's accuracies (Table 4-3) for those respective types in 2016 closely resemble the 2011 metrics calculated by Carle et al. (2014). The similar

accuracies in classification results between the two years indicate that the very high spatial resolution of the WorldView-2 data (2 m, 8 bands) provides a similar advantage as the high spectral resolution AVIRIS-NG data (5.4 m, 290 utilized bands). We can therefore conclude that our estimates of distribution, expansion, and recession for these vegetation types accurately reflects the WLD's accretion-driven evolution.

Building on the vegetation distributions, our AGB estimates (Figure 3-11; Jensen et al. 2019b) show how aboveground growth patterns vary across elevations and HGZs (Figure 4-7) by vegetation type. The forested wetland AGB distributions show a general increasing trend with elevation. *S. nigra* shows no significant difference in AGB between supratidal and above supratidal HGZs where it is present. However, plotting the average AGB for the forested wetlands by elevations does reveal a notable pattern whereby the AGB steadily increases from approximately 0.4-0.6 m (Figure 4-7) before reaching a plateau. This is likely due to younger trees with lower AGB becoming established on accreting banks at lower elevations towards the delta fringes. Additionally, Li et al. (2006) show that, relative to well drained samples, *S. nigra* shoot biomass allocation increases when exposed to partial flooding. The peak at roughly 0.3 m, being the lowest present elevation for *S. nigra*, is likely due to the presence of mature trees on the channel-side of the island banks where they are exposed to the channel water surface.

Conversely, the herbaceous AGB distributions from the remotely sensed estimates show a general decreasing trend in concert with increasing marsh platform elevation. Each assessed herbaceous vegetation type—*C. esculenta*, *P. punctatum,* and grasses—varies significantly across each HGZ where present (Figure 4-7). Each vegetation type's AGB peaks in the low intertidal zone and decreases through the supratidal zone. This occurs as the plants allocate less biomass to their aboveground structure as they spend less time inundated by the tide (Morris et al. 2002).

Increasing inundation time coincides with an increase in overall biomass production in intertidal vegetation, and is further controlled by inorganic sedimentation (Mudd et al. 2009; Twilley et al. 2019). Biomass production is contingent upon feedbacks between marsh elevation and sedimentation. Higher elevation results in less flooding and exposure to inorganic suspended sediment, while also resulting in lower biomass and less root growth (but a higher root:shoot ratio) (Mudd et al. 2009). It should be noted that there are some high AGB grass areas in the low intertidal zone that cause this class to deviate from this pattern. These solitary stands, typically *Z. miliacea*, grow in the deltaic island interiors that are frequently flooded and otherwise dominated by *N. lutea*, floating vegetation, or SAV. Additionally, each of the herbaceous types show a slight increase in AGB in the above supratidal zone rather than a further linear decrease. This zone sees significant competition amongst different plant types outside of tidal influence (Ma et al. 2018), and there is accordingly greater heterogeneity in these higher elevations. The observed increase in AGB here, then, is likely due to the increased abundance of different plants growing in the same area. The overall AGB of a specific plant type by itself may decrease in this zone, but the remote sensing model estimates higher AGB if it is intermixed with other abundant plants.

The marsh organ experiment examining *C. esculenta* in the WLD (Figure 4-8; Rovai et al. *in progress*) complements our remotely sensed AGB distributions, providing a controlled experiment in the same study site to examine plant growth patterns across HGZs. The aboveground NPP values decrease across higher elevations (Figure 4-8), though there is a corresponding increase in root:shoot ratios as the plant allocates less aboveground. While *C. esculenta* belowground production peaks in the high intertidal zone, there is no corresponding linear increase in root allocation (Table 4-4). Of particular note is the alignment between the experimentally-derived NPP (Table 4-4, Figure 4-8) in the low intertidal zone (mean = 355.63 g $m^{-2}$ $yr^{-1}$) and the

average remote sensing estimate of AGB (Figure 4-7) for this HGZ (mean = 364.12 g/m$^2$). This shows that the *C. esculenta* in the low intertidal zone is largely expanding into the area rather than growing in an established area, as the annual aboveground growth rate closely aligns with the standing AGB at the end of the growing season in October. Aboveground NPP decreases through the supratidal in accordance with the remotely sensed AGB estimates. The above supratidal zone in the marsh organ experiment, however, shows even lower aboveground NPP despite the increase in the remotely sensed AGB. This lower value at the highest elevations is likely due to a dehydration effect in the highest elevation pipes (Snedden et al. 2015), whereas *C. esculenta* at similar natural elevations are frequently shaded by a tree canopy. The discrepancy between the two assessments can likely be attributed to the increasing heterogeneity and competition in the higher elevations as previously discussed in concert with dehydration inhibiting growth.

Our study indicates that the WLD will continue to build significant stores of biomass as it continues to accrete and see its assemblage of vegetation species change. *S. nigra*'s outward growth along the deltaic island banks has increased the WLD's overall biomass, though the herbaceous vegetation is much more dynamic. The various grass species are significant biomass sources, having higher average AGB than other herbaceous plant types. Though we estimated a slight net decrease in grass extent, there are many areas of the island interiors, adjacent to the banks, where grasses have established and contribute large AGB stocks. As *C. esculenta* exhibits slightly higher median AGB values from the low intertidal to the supratidal zones, its replacement of *P. punctatum* likely resulted in a net increase of total biomass.

### 4.6. Conclusion

Louisiana's WLD is a complex and dynamic system that has implications for restoration efforts throughout the state's degrading coastline. Our results detail how plant communities'

composition and growth patterns change under an altered hydrologic regime, as with the construction of the Wax Lake Outlet. Here we employed a multi-sensor airborne remote sensing dataset to examine vegetation distributions and changes in the WLD. From October 2011 to October 2016, the delta saw significant expansion of the invasive species *C. esculenta* into area previously occupied by *P. punctatum*, along with a minor increase in forested area dominated by *S. nigra*. Within the assessed vegetation classes, including the aforementioned species, AGB does vary significantly across elevation. The forested wetlands steadily increase in AGB in the supratidal zone and plateau, while herbaceous plants' AGB generally peaks in the low intertidal and decreases through the supratidal zone. This analysis allows us to characterize changes and assess productivity in the WLD, thereby informing future restoration efforts regarding patterns that may emerge with changing ecology.

This study quantifies succession and growth patterns in the WLD, building insights into deltaic development in doing so. *C. esculenta*'s outward growth and dominance in the WLD is indicative of many invasive species' ability to supplant native vegetation and decrease a region's compositional heterogeneity—especially following disturbance events. The relationship between emergent vegetation and biomass, corroborated by the *in situ* marsh organ experiment, further characterizes each plant type's growth and development. The resulting AGB zonation patterns allow for better assessment of wetland carbon stocks, as well as biomass projections for restoration efforts. Potential river diversions in the MDP, for example, will deliver fresh water and sediment to degrading wetland regions, thereby altering an area's hydrology and vegetation composition as with the Wax Lake Outlet. The changes in vegetation composition and biomass distribution in the WLD assessed here may inform how vegetation will grow and change under such altered conditions.

## 4.7. References

Adam, Elhadi, and Onisimo Mutanga. 2009. “Spectral Discrimination of Papyrus Vegetation (Cyperus Papyrus L.) in Swamp Wetlands Using Field Spectrometry.” *ISPRS Journal of Photogrammetry and Remote Sensing* 64 (6): 612–20.

Adam, Elhadi, Onisimo Mutanga, and Denis Rugege. 2010. “Multispectral and Hyperspectral Remote Sensing for Identification and Mapping of Wetland Vegetation: A Review.” *Wetlands Ecology and Management* 18 (3): 281–96.

Allen, Yvonne C., Brady R. Couvillion, and John A. Barras. 2012. “Using Multitemporal Remote Sensing Imagery and Inundation Measures to Improve Land Change Estimates in Coastal Wetlands.” *Estuaries and Coasts* 35 (1): 190–200.

Barras, J., S. Beville, D. Britsch, S. Hartley, S. Hawes, J. Johnston, P. Kemp, Q. Kinler, A. Martucci, J. Porthouse, D. Reed, K. Roy, S. Sapkota, and J. Suhayda. 2003. *Historical and Projected Coastal Louisiana Land Changes: 1978-2050*. Reston, VA.

Barras, J.A., J.C. Bernier, and R.A. Morton. 2008. “Land area change in coastal Louisiana—A multidecadal perspective (from 1956 to 2006): U.S. Geological Survey Scientific Investigations Map 3019, scale 1:250,000,” 14 p. pamphlet. Reston, VA.

Belluco, Enrica, Monica Camuffo, Sergio Ferrari, Lorenza Modenese, Sonia Silvestri, Alessandro Marani, and Marco Marani. 2006. Mapping salt-marsh vegetation by multispectral and hyperspectral remote sensing.” *Remote Sensing of Environment* 105 (1):54–67.

Bevington, Azure E. 2016. “Dynamics of land building and ecological succession in a prograding deltaic floodplain, Wax Lake delta, LA, USA.” PhD Dissertation. Louisiana State University.

Bevington, Azure E., Robert R. Twilley, Charles E. Sasser, and Guerry O. Holm. 2017. "Contribution of River Floods, Hurricanes, and Cold Fronts to Elevation Change in a Deltaic Floodplain, Northern Gulf of Mexico, USA." *Estuarine, Coastal and Shelf Science* 191: 188–200.

Bue, Brian D., David R. Thompson, Michael Eastwood, Robert O. Green, Bo Cai Gao, Didier Keymeulen, Charles M. Sarture, Alan S. Mazer, and Huy H. Luong. 2015. "Real-Time Atmospheric Correction of AVIRIS-NG Imagery." *IEEE Transactions on Geoscience and Remote Sensing* 53 (12): 6419–28.

Byrd, Kristin B., Laurel Ballanti, Nathan Thomas, Dung Nguyen, James R. Holmquist, Marc Simard, and Lisamarie Windham-Myers. 2018. "A remote sensing-based model of tidal marsh aboveground carbon stocks for the conterminous United States." *ISPRS Journal of Photogrammetry and Remote Sensing* 139:255–271.

Byrd, Kristin B., Jessica L. O'Connell, Stefania Di Tommaso, and Maggi Kelly. 2014. "Evaluation of Sensor Types and Environmental Controls on Mapping Biomass of Coastal Marsh Emergent Vegetation." *Remote Sensing of Environment* 149: 166–80.

Carle, Melissa V., and Charles E. Sasser. 2016. "Productivity and Resilience: Long-Term Trends and Storm-Driven Fluctuations in the Plant Community of the Accreting Wax Lake Delta." *Estuaries and Coasts* 39 (2):406–422.

Carle, Melissa V., Charles E. Sasser, and Harry H. Roberts. 2015. "Accretion and Vegetation Community Change in the Wax Lake Delta Following the Historic 2011 Mississippi River Flood." *Journal of Coastal Research* 31 (3):569–587.

Carle, Melissa V., Lei Wang, and Charles E. Sasser. 2014. "Mapping Freshwater Marsh

Species Distributions Using WorldView-2 High-Resolution Multispectral Satellite Imagery." *International Journal of Remote Sensing* 35 (13): 4698–4716.

Craft, Christopher, Jonathan Clough, Jeff Ehman, Samantha Jove, Richard Park, Steve Pennings, Hongyu Guo, and Megan Machmuller. 2009. "Forecasting the Effects of Accelerated Sea-Level Rise on Tidal Marsh Ecosystem Services." *Frontiers in Ecology and the Environment* 7 (2): 73–78.

Day, J. W., D. F. Boesch, E. J. Clairain, G. P. Kemp, S. B. Laska, W. J. Mitsch, K. Orth, H. Mashriqui, D. J. Reed, L. Shabman, C. a Simenstad, B. J. Streever, R. R. Twilley, C. C. Watson, J. T. Wells, and D. F. Whigham. 2007. "Restoration of the Mississippi Delta: lessons from Hurricanes Katrina and Rita." *Science* 315 (5819):1679–84.

FitzGerald, Duncan M., Michael S. Fenster, Britt A. Argow, and Ilya V. Buynevich. 2008. "Coastal Impacts Due to Sea-Level Rise." *Annual Review of Earth and Planetary Sciences* 36 (1):601–647.

Freeman, Anthony, and Stephen L. Durden. 1998. "A Three-Component Scattering Model for Polarimetric SAR Data." *IEEE Transactions on Geoscience and Remote Sensing* 36 (3): 963–73.

Gao, Bo Cai, Kathleen B. Heidebrecht, and Alexander F.H. Goetz. 1993. "Derivation of Scaled Surface Reflectances from AVIRIS Data." *Remote Sensing of Environment* 44 (2–3): 165–78.

Hamlin, L., R. O. Green, P. Mouroulis, M. Eastwood, D. Wilson, M. Dudik, and C. Paine. 2011. "Imaging spectrometer science measurements for terrestrial ecology: AVIRIS and new developments." *IEEE Aerospace Conference Proceedings*:1–8.

Jensen, Daniel J., Marc Simard, Kyle C. Cavanaugh, and David R. Thompson. 2017. "Imaging

Spectroscopy BRDF Correction for Mapping Louisiana's Coastal Ecosystems." *IEEE Transactions on Geoscience and Remote Sensing* 56 (3): 1739–48.

Jensen, Daniel, Marc Simard, Kyle Cavanaugh, Yongwei Sheng, Cédric G. Fichot, Tamlin Pavelsky, and Robert Twilley. 2019a. "Improving the Transferability of Suspended Solid Estimation in Wetland and Deltaic Waters with an Empirical Hyperspectral Approach." *Remote Sensing* 11 (1629).

Jensen, Daniel, Kyle C. Cavanaugh, Marc Simard, Gregory S. Okin, Edward Castañeda-Moya, Annabeth McCall, and Robert R. Twilley. 2019b. "Integrating Imaging Spectrometer and Synthetic Aperture Radar Data for Estimating Wetland Vegetation Aboveground Biomass in Coastal Louisiana." *Remote Sensing* 11 (21):2533.

Kirwan, Matthew L., and Glenn R. Guntenspergen. 2010. "Influence of Tidal Range on the Stability of Coastal Marshland." *Journal of Geophysical Research* 115 (F2): 1–11.

Kirwan, Matthew L., Glenn R. Guntenspergen, Andrea D'Alpaos, James T. Morris, Simon M. Mudd, and Stijn Temmerman. 2010. "Limits on the adaptability of coastal marshes to rising sea level." *Geophysical Research Letters* 37 (23):1–5.

Kirwan, Matthew L., and J. Patrick Megonigal. 2013. "Tidal wetland stability in the face of human impacts and sea-level rise." *Nature* 504 (7478):53–60.

Krauss, Ken W., Karen L McKee, Catherine E Lovelock, Donald R Cahoon, Neil Saintilan, Ruth Reef, and Luzhen Chen. 2014. "How Mangrove Forests Adjust to Rising Sea Level." *The New Phytologist* 202 (1): 19–34.

Li, Shuwen, S. Reza Pezeshki, and F. Douglas Shields. 2006. "Partial flooding enhances aeration in adventitious roots of black willow (Salix nigra) cuttings." *Journal of Plant Physiology* 163 (6):619–628.

Ma, Hongxu, Laurel G. Larsen, and R. Wayne Wagner. 2018. “Ecogeomorphic Feedbacks that Grow Deltas.” *Journal of Geophysical Research: Earth Surface* 123 (12):3228–3250.

Morris, James T., P. V. Sundareshwar, Christopher T. Nietch, Björn Kjerfve, and D. R. Cahoon. 2002. “Responses of Coastal Wetlands to Rising Sea Level.” *Ecology* 83 (10): 2869–77.

Morris, James T. 2007. “Estimating net primary production of salt marsh macrophytes.” In *Principles and standards for measuring primary production*, ed. T. J. Fahey and A. K. Knapp, 106-119. New York, NY: Oxford University Press.

Mudd, Simon M., Susan M. Howell, and James T. Morris. 2009. “Impact of Dynamic Feedbacks between Sedimentation, Sea-Level Rise, and Biomass Production on near-Surface Marsh Stratigraphy and Carbon Accumulation.” *Estuarine, Coastal and Shelf Science* 82 (3): 377–89.

Rovai, Andre S., Robert R. Twilley; Alexandra Christensen, Daniel Jensen, Gregg A. Snedden, Christopher N. Janousek, and James T. Morris T. *In Progress.* “Tidal freshwater wetlands adapt to multiple platform elevations in response to coastal dynamics.” To be submitted to *Estuaries and Coasts*.

Shlemon, R. J. 1975. “Subaqueous delta formation-Atchafalaya Bay, Louisiana.” In *Deltas: Models for Exploration*, ed. M. Lou Broussard, 209–221. Houston, TX: Houston Geological Society.

Snedden, Gregg A., Kari Cretini, and Brett Patton. 2014. “Inundation and salinity impacts to above- and belowground productivity in Spartina patens and Spartina alterniflora in the Mississippi River deltaic plain: Implications for using river diversions as restoration tools.” *Ecological Engineering* 81:133–139.

Spalding, E. A., and M. W. Hester. 2007. “Interactive Effects of Hydrology and Salinity on

Oligohaline Plant Species Productivity: Implications of Relative Sea-level Rise." *Estuaries and Coasts* 30 (2):214–225.

Thompson, David R., Bo Cai Gao, Robert O. Green, Dar A. Roberts, Philip E. Dennison, and Sarah R. Lundeen. 2015. "Atmospheric Correction for Global Mapping Spectroscopy: ATREM Advances for the HyspIRI Preparatory Campaign." *Remote Sensing of Environment* 167: 64–77.

Twilley, Robert R., Samuel J. Bentley, Qin Chen, Douglas A. Edmonds, Scott C. Hagen, Nina S.N. Lam, Clinton S. Willson, et al. 2016. "Co-Evolution of Wetland Landscapes, Flooding, and Human Settlement in the Mississippi River Delta Plain." *Sustainability Science* 11 (4): 711–31.

Twilley, R. R., J. W. Day, A. E. Bevington, E. Castañeda-moya, A. Christensen, G. Holm, L. R. Heffner, R. Lane, A. Mccall, A. Aarons, S. Li, A. Freeman, and A. S. Rovai. 2019. "Ecogeomorphology of coastal deltaic floodplains and estuaries in an active delta: Insights from the Atchafalaya Coastal Basin." *Estuarine, Coastal and Shelf Science* 227 (August).

U.S. Geological Survey. 2014. *USGS NED ned19_n29x75_w091x50_LA-USGS_Atchafalaya2 2012_2014 1/9 arc-Second 20140615 15 x 15 Minute IMG*; U.S. Geological Survey, Reston, VA, USA. Available online: http://ned.usgs.gov/ (accessed on 10 October 2018).

Zomer, Robert J., Antonio Trabucco, and Susan L. Ustin. 2008. "Building spectral libraries for wetlands land cover classification and hyperspectral remote sensing." *Journal of Environmental Management* 90 (7):2170–2177.

# Conclusion

The models, results, and findings of the preceding chapters represent a broader effort towards applying imaging spectroscopy for accurate quantification of wetland accretion. Net vertical accretion in coastal wetlands comprises multiple additive processes—including tidal inundation, sedimentation, and bioproductivity (FitzGerald et al. 2008). In addition to the necessary corrections and image processing making such analysis possible (Jensen et al. 2017), the studies contained herein develop methods and products from an airborne imaging spectrometer dataset that represent these key accretionary processes. Developing a model of hydrologic suspended solids whose transferability is enabled by imaging spectroscopy will permit effective estimation of accretion's inorganic sedimentation component (Jensen et al. 2019a). The transferability of this algorithm is key, as it will permit application to future imaging spectrometer datasets without the need for recalibration and thus allow for cumulative sediment supply estimates to be made over a timeseries. In concert with synthetic aperture radar, the bioproductivity component was also addressed (Jensen et al. 2019b; Jensen et al. *in progress*). The observable aboveground portion of wetland biomass is a key indicator of its overall productivity, and can further be applied to estimate belowground biomass and production. In modeling and examining suspended solids, aboveground biomass, and vegetation species and their growth patterns, we are using imaging spectroscopy to conduct spatially explicit analyses that will inform future modeling efforts towards the remote sensing of wetland accretion.

Future efforts will pursue a landscape-scale accretion model that uses remote sensing data to project changes in wetland elevation and submergence. Such analysis will entail more targeted campaigns over coastal Louisiana, but these efforts will also be expanded upon and operationalized with Earth-observing satellite missions currently in development. The NASA-ISRO Synthetic

Aperture Radar (NISAR), being similar in instrumentation to UAVSAR, will provide global coverage of SAR data enabling improved AGB estimates as well as the flow of water through wetland vegetation. The Surface Water Ocean Topography (SWOT) mission will also collect data on water surface elevations and discharge in river channels. These data will complement those from the Surface Biology and Geology (SBG) mission, a satellite-borne imaging spectrometer akin to AVIRIS-NG. SBG's reflectance measurements will allow for global and repeatable mapping of wetland vegetation, AGB, and water contents. The temporal coverage provided by NISAR, SWOT, and SBG will permit long-term measurements of these parameters to be assessed. These measurements will link various accretionary components—including bioproductivity and sedimentation—at landscape scales. Building on the methods and results developed here, we will then be able to model accretion rates. Subsequently, we will be able to project changes in wetland soil elevation and quantify risk of wetland submergence as RSLR continues to worsen in vulnerable wetlands throughout the world.

**References**

FitzGerald, Duncan M., Michael S. Fenster, Britt A. Argow, and Ilya V. Buynevich. 2008. "Coastal Impacts Due to Sea-Level Rise." *Annual Review of Earth and Planetary Sciences* 36 (1):601–647.

Jensen, Daniel J., Marc Simard, Kyle C. Cavanaugh, and David R. Thompson. 2017. "Imaging Spectroscopy BRDF Correction for Mapping Louisiana's Coastal Ecosystems." *IEEE Transactions on Geoscience and Remote Sensing* 56 (3): 1739–48.

Jensen, Daniel, Marc Simard, Kyle Cavanaugh, Yongwei Sheng, Cédric G. Fichot, Tamlin

Pavelsky, and Robert Twilley. 2019a. “Improving the Transferability of Suspended Solid Estimation in Wetland and Deltaic Waters with an Empirical Hyperspectral Approach.” *Remote Sensing* 11 (1629).

Jensen, Daniel, Kyle C. Cavanaugh, Marc Simard, Gregory S. Okin, Edward Castañeda-Moya, Annabeth McCall, and Robert R. Twilley. 2019b. “Integrating Imaging Spectrometer and Synthetic Aperture Radar Data for Estimating Wetland Vegetation Aboveground Biomass in Coastal Louisiana.” *Remote Sensing* 11 (21):2533.

Jensen, Daniel, Kyle C. Cavanaugh, Marc Simard, Alexandra. Christensen, Andre Rovai, and Robert R. Twilley. *In Progress.* “Accretion-driven variation in vegetation composition and biomass in Louisiana's Wax Lake Delta.” To be submitted to *Estuarine, Coastal and Shelf Science*.